KATHMANDU UNIVERSITY

SCHOOL OF ENGINEERING

DEPARTMENT OF MECHANICAL ENGINEERING

DISSERTATION ON

NTNU

SECONDARY FLOW AND SEDIMENT EROSION IN FRANCIS TURBINES

In Partial Fulfillment of the Requirements for the
Doctorate Degree in Mechanical Engineering

Sailesh Chitrakar

June, 2018

Preface

This thesis comprises of the works done as a joint PhD between Kathmandu University (KU) and Norwegian University of Science and Technology (NTNU). The works were carried out at the Waterpower Laboratory under Department of Energy and Process Engineering at NTNU and Turbine Testing Lab under Department of Mechanical Engineering at KU. The work is a part of a project, SEDIPASS (Sustainable design and operation of hydropower plants exposed to high sediment yield) funded by Norwegian Research Council.

Acknowledgement

This PhD is a joint degree between Kathmandu University (KU) and Norwegian University of Science and Technology (NTNU). I am grateful to many people from both the Universities for the completion of this work. My supervisors for this work are Assoc. Prof. Hari Prasad Neopane from KU and Prof. Ole Gunnar Dahlhaug from NTNU. I feel blessed to have received a complete trust and support on my work by them. Whether by providing prompt logistic supports, giving technical feedbacks, motivations for carrying further works or travelling for different purposes, my supervisors have always been key persons to have made them possible. Hence, I would like to thank them from the core of my heart.

I spent one and a half year at NTNU and rest at KU. I received love and support at both places. At NTNU, I used to have fruitful discussions with Dr. Biraj Singh Thapa. With him supporting me in technical and non-technical matters, the problems got half easier to solve. I would like to thank Bård Brandåstø for helping me speed up the lab works. When I was there, I received technical suggestions from my colleagues, Dr. Chirag Trivedi, Mr. Igor Iliev, and everyone from the Waterpower Laboratory. I want to thank them for the interesting discussions. Moreover, I couldn't be more thankful for the technical persons of the lab, Joer, Halvor and Trygve, for making all the lab testing possible. I would also like to thank the administrative persons, specially Wenche and Thea, for helping me in many ways.

At KU, I would like to thank Prof. Bhola Thapa, whose motivation has always thrived me to become a better researcher. I would like to thank everyone in the Turbine Testing Lab, who have become much more than an office colleague by now. Besides the lab, I also used to have interesting discussions with Dr. KP Shrestha, thank you for your valuable suggestions.

Finally, amid the ups and downs I went through my work, my parents were always behind me. I would like to thank my family for their continuous love and support.

Abstract

Sediment erosion of the hydropower turbine components is one of the key challenges due to the constituent of hard particles in the rivers of Himalayas and Andes. In these regions, Quartz is found as a main constituent (more than 50%), along with feldspar and other hard minerals. These particles have hardness more than 5 Moh's scale, which is capable to erode turbine components. This has not only caused maintenance problems of the turbines, but has also decreased the efficiency of the plant during operation. In the case of Francis turbines, erosion is mostly observed around stay vanes, guide vanes and runner blades. The quantity and pattern of erosion depends upon the operating conditions and type of flow phenomena in particular regions. The flow phenomena in Francis turbines are highly unsteady, especially around guide vanes and runner. The flow instability arises in the form of leakage through clearance gap, horseshoe vortex, rotor-stator interaction and turbulences supported by high velocity and acceleration. The erosion on the other hand, deteriorates the surface morphology, aggravating the flow.

This study focuses on the leakage flow through the clearance gap of guide vanes of Francis turbines by using both numerical and experimental techniques. The clearance gap is identified as a simultaneous effect of secondary flow and erosion inside guide vanes of sediment affected power plants. A cascade rig containing a single guide vane (GV) was developed in a previous study, which gives a close estimation of the flow field around one GV compared to that in the real turbine. The walls covering the rig were designed such that a sufficient swirl component of the flow is developed at the inlet of the guide vane. In this study, the velocity field around the GV containing clearance gap of size 2 mm at one end is captured using Particle Image Velocimetry (PIV) technique. Pressure sensors are used to estimate the GV loading at designed GV opening angle. A numerical model of the same rig is made, and the results from the CFD are validated with the experiments. The leakage flow is investigated further using CFD, and it has been found that this flow leads to the formation of a vortex filament, which travels downstream striking the runner blade at inlet.

Since the one GV cascade rig is unable to predict the velocity field at different GV opening angles, a three GV cascade rig has been considered in this work. The three GV cascade rig overcomes the limitations of the one GV rig by causing minimum influence from the neighboring walls. On comparing asymmetrical GV profiles with the reference GV profile, it is found from both one GV and three GV cascade rig that asymmetrical GV profiles are more suitable for turbines affected by erosion. This is due to reduced pressure difference between the two GV sides, which consequently reduces the extent of the leakage flow and vortices originating from it.

A numerical analysis has also been performed in a complete turbine passage, including GV and runner to investigate the effect of the leakage flow on the performances of the turbine. The results are compared with experiment conducted in one GV cascade rig, developed for the same turbine. Simulations are performed for 3 GV profiles with each at 11 operating conditions. It is found that the symmetrical guide vane profile, which is the reference profile in the plant, is not suitable for best efficiency and part load conditions. Such a profile could wear the runner blade by both erosion and cavitation. It is also found that asymmetrical profiles could increase the performance of the turbine at all operating conditions. However, in the case of asymmetrical profiles, some negative leakage flow could appear at full load conditions, which have a tendency to hit neighboring GV causing erosion. This thesis gives an indication of the flow behavior through the clearance gap of GV for different GV profiles. The results from this thesis can be used to conduct rigorous optimization technique such that the most optimized profile suitable for all the operating conditions can be chosen.

Contents

List of Figures

List of Tables

List of Symbols

Euler's equation of turbine and velocity triangle

C_u	Tangential component of absolute velocity	m/s
C_{u1}	Tangential component of absolute velocity at the inlet	m/s
C_{u2}	Tangential component of absolute velocity at the outlet	m/s
ρ	Density	kg/m^3
g	Acceleration due to gravity	m/s^2
Q	Flow rate or Discharge	m^3/s
u	Tangential velocity of the runner	m/s
u_2	Tangential velocity of the runner at the outlet	m/s
u_1	Tangential velocity of the runner at the inlet	m/s
η_h	Hydraulic efficiency of the turbine	[-]
W	Relative velocity	m/s

List of Symbols

Quantification of leakage flow

C_u	Tangential component of absolute velocity	m/s
C_m	Meridional component of absolute velocity	m/s
u	Cartesian velocity component in x direction	m/s
v	Cartesian velocity component in y direction	m/s
V	Average velocity at point (X,Y)	m/s
θ	Angle made by V with respect to u	°
α	Angle of the chord	°
β	Angle representing the direction of the velocity vector	°
X_1, Y_1	Point of the leading edge	m
X_2, Y_2	Point of the trailing edge	m
V'_x	Velocity component along the chord length	m/s
V'_y or Vy	Velocity component normal to the chord length	m/s
V_o	Reference velocity	m/s
n	Number of points along the chord	[-]
L_{ff}	Leakage flow factor	[-]
i	index	[-]

List of Symbols

Sediment erosion (The symbols of the erosion models are presented in the chapter)

S	Hydro-abrasive erosion depth	mm
W	Characteristic velocity	m/s
PL	Particle load	$kg \times h/m^3$
C	Concentration of particles	kg/m^3
K_f	Flow coefficient	$\frac{mm \times s^{3.4}}{kg \times h \times m^{\alpha}}$
K_m	Material factor	[-]
RS	Turbine's reference diameter	m
p	Value of the exponent	[-]
K_{size}	Size factor	[-]
K_{shape}	Shape factor	[-]
$K_{hardness}$	Hardness factor	[-]
W_{gv}	Characteristic velocity for guide vanes	m/s
W_{run}	Characteristic velocity for runner	m/s
u_2	Velocity of runner	m/s
c_2	Velocity of water	m/s
α	Average shortest distance between adjacent guide vanes	m
Z_0	Total number of guide vanes in a turbine	[-]
B_0	Height of the distributor	m
n	Rotation speed of the runner	rad/s
D	Diameter of the runner	m

List of Symbols

CFD and PIV

t	Time	sec
Δt	Time step	sec
ϕ_{fg}	Cross-correlation function	
ρ	Density of fluid	kg/m^3
$\vec{V}$	Velocity vector	m/s
u_i	Time-averaged velocity components	m/s
p	Time-averaged pressure	Pa
ν	Fluid kinematic viscosity	m^2/s
u_i'	Fluctuating velocity components	m/s
τ_{ij}	Reynold's stress	Pa
h	Size of the grid	m
ϕ	Any variable	
e_a	Approximate relative error	[-]
e_{ext}	Extrapolated relative error	[-]
GCI_{fine}	Grid Convergence Index of fine mesh	[-]
C_p and CTP	Normalized pressure	[-]

List of Abbreviation

KU	Kathmandu University
NTNU	Norwegian University of Science and Technology
TTL	Turbine Testing Lab
GV	Guide Vane
PS	Pressure Side
SS	Suction Side
NACA	National Advisory Committee for Aeronautics
BEP	Best Efficiency Point
CFD	Computational Fluid Dynamics
PIV	Particle Image Velocimetry
ICEM	Integrated Computer Engineering and Manufacturing
GCI	Grid Convergence Index
HPP	Hydro Power Plant
SV	Stay Vane
CG	Clearance Gap
SVout	Stay Vane Outlet
GVin	Guide Vane Inlet
GVout	Guide Vane Outlet
Rin	Runner Inlet
PDE	Partial Derivative Equation

List of Abbreviation

MW	Mega Watt
GW	Giga Watt
ASTM	American Society for Testing and Materials
LIF	Laser Induced Fluorescence
LDA	Laser Doppler Anemometry
RSI	Rotor Stator Interaction
TRPIV	Transient Particle Image Velocimetry
VG	Vortex Generator
BPF	Blade Passing Frequency
HVOF	High Velocity Oxygen Fuel
RDA	Rotating Disc Apparatus
WC	Tungsten Carbide
IEC	International Electrotechnical Commission
AoA	Angle of Attack
HZ	Hertz
Nd-YAG	Neodymium-doped Yttrium Aluminum Garnet
CCD	Charge-Coupled Device
LE	Leading Edge
TE	Trailing Edge

Chapter 1

Introduction

Hydropower is one of the cleanest forms of energy and has been used in many countries as a principle source of electricity. However, it has been reported that 2/3rd of the world's feasible hydropower resources are still undeveloped. Out of these potential resources, more than 55% lies in Asia alone [1]. Despite the future prospects in hydropower development in this region, the geological problem seems to be a major obstacle. It has been studied that out of 20 billion tons of global sediment flux from rivers to the oceans per year, around 6 billion tons is contributed by Asian rivers, particularly from Indian subcontinent [2]. Apart from the huge sediment load, the sand particles contain hard minerals which can erode the turbines made of steel. It was reported that in Nepalese rivers, nearly 70% of the constituent are hard particles, including Quartz [3]. The problem of sediment handling, maintenance and operation of the power plants has become a serious issue.

Francis turbines are the most widely used reaction turbines, suitable for medium head and flow conditions. In these turbines, the flow is regulated through wicket gates or guide vanes present upstream of the runner. The guide vanes are oriented at an angle, which provides the required inlet angle in the runner for a given flow. At varying load conditions, this opening angle is adjusted so that the constant speed of the turbine is maintained. The shape of the guide vane is typically a hydrofoil connected to shafts at two ends for opening and closing. A certain number of guide vanes are distributed around the runner forming a circular ring. When the guide vanes are completely closed, the trailing edge of one guide vane (GV) touches the leading edge of neighboring vane with some overlapping factor. The GVs are assembled inside facing plates, that extends downstream as runner hub and shroud. The GV shafts are pulled out of facing plates through holes and connected to GV control mechanisms. To enable rotation of the shafts, a small clearance gap is made between the GV ends and the facing plates during manufacturing. The gap is also called dry clearance, which grows in size due to water pressure on the facing plates. Apart from maintaining the flow, GVs also play role in converting the hydraulic energy of water into the kinetic energy. The flow inside GV is accompanied with highest acceleration, which results in unsteady nature of the fluid. In the case of hard sediment particles flowing together with water, the high turbulence and high velocity tend to erode the GV and facing plate material. The horseshoe vortex erodes the corners and due to the pressure difference in the GV, the flow is driven from high pressure side (PS) to the low pressure side or suction side (SS),

which is termed as the leakage flow. This flow abrades the GV ends and facing plates, resulting in the increased size of the gap. When the leakage flow takes place with high acceleration, it distorts the primary or main flow in SS causing efficiency loss and structural problems downstream of the GV.

This study focuses on investigating the leakage flow through the clearance gap and its potential effects on the performances of the turbine. These effects have been related with the GV's profile by studying the pressure distribution around the hydrofoils.

1.1 Objectives

1. Investigate the secondary flow phenomena around guide vanes including erosion induced clearance gap.
2. Study the effect of leakage flow through clearance gaps on the performance of the runner.
3. Compare pressure distribution around guide vane, leakage flow and performance of the runner using guide vanes of different hydrofoils.

1.2 Methodology

The methodology of this work is divided into three parts. These parts are shown in Figure 1.1. In the first part, all the investigations are carried out in one GV cascade rig. One GV cascade rig is a reduced model of the GV ring, consisting of a periodic section and covering an angular range of 30° out of the total circumference of the ring. Since this rig requires only $1/12^{th}$ of the designed flow of the turbine, this rig makes it possible to test in BEP with laboratory capacity. Therefore, both experiments and CFD are carried out in this rig, so that the numerical model can be tested and used for further investigations. In the figure, the numbers 0012, 2412 etc. represent different NACA profiles having same thickness, which were tested and compared.

Similarly, the three GV cascade rig covers an angular range of 60° out of the total circumference of the ring. The required flow to test in BEP is $1/6^{th}$ of the designed flow, which makes it more challenging to be tested in laboratory. This thesis consists of testing this rig numerically and comparing the results with one GV rig. The idea is to investigate the flow when the opening angle of GV changes, which was not possible to test in one GV rig.

In both the rigs, the GVs contain clearance gaps of 2 mm on one end, which induces secondary flow. This flow passes inside the runner, affecting the overall performances of the turbine. To study the effect of such flow on runner blades, a numerical investigation is carried out in the actual turbine, by taking GV and runner blade passages. In this case, 11 GV opening angles and 3 NACA profiles are tested, so that the most optimum NACA profile in all the operating conditions can be investigated. Similar to the three GV rig, the results obtained from the simulation of the turbine is compared with

the results from one GV rig. The comparison primarily includes the nature of the vortex originating from the leakage flow through the clearance gap.

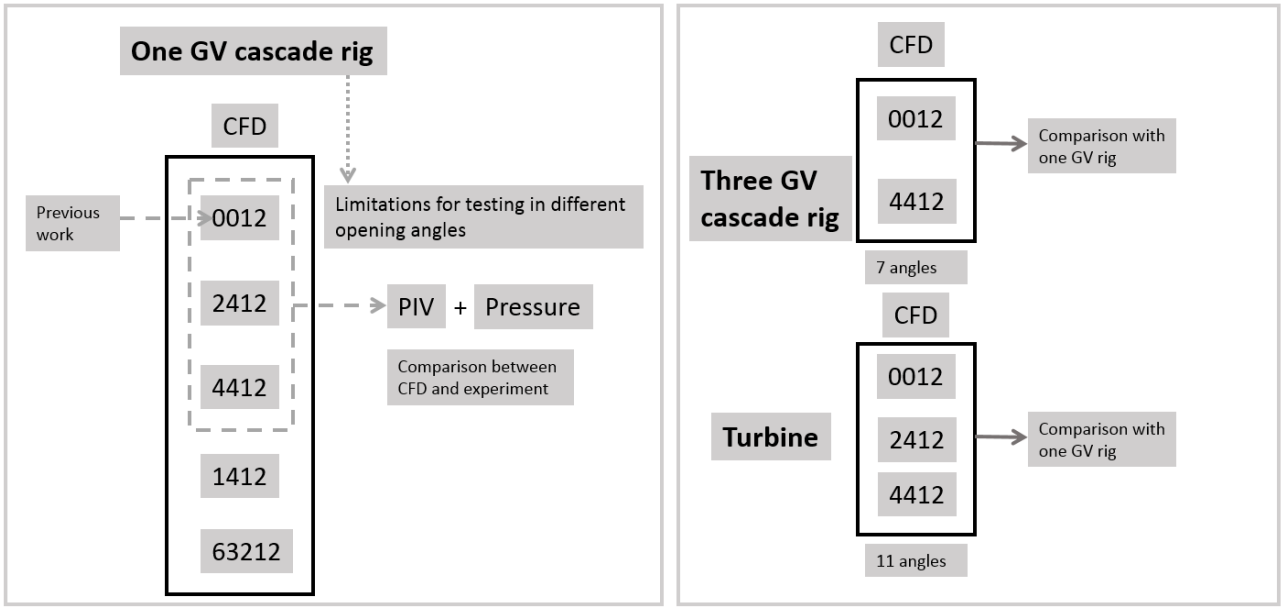

Figure 1.1: Methodology used in this study

1.3 Scope and limitations

This study uses both numerical and experimental techniques to investigate the flow phenomena around GVs of a Francis turbine. The GVs correspond to a high/medium head type Francis turbine of Jhimruk HPP in Nepal. Numerical study is performed using CFD in ANSYS CFX 15.0. Experimental study includes a two-dimensional Particle Image Velocimetry (PIV) and pressure measurements. One GV cascade rig developed in a previous study [4] is used to investigate different GV profiles. Three GV cascade rig is designed with the same principle as one GV. The rigs do not contain runner blades. Hence, the measurements are performed in steady conditions. The size of the GVs used in this study is in the original scale compared to the real turbine. The GVs contain a clearance gap of 2 mm on one side. The gap represents eroded surface, which is non-uniform in the real case. However, the eroded surface is considered to be uniform in this study. In PIV, the seeding particles have the density close to water. However, sediment particles or seeding particles close to the density of the sediment are not used in any analysis. This is because the aim of this work is to investigate the potential consequences of erosion, rather than the mechanisms of erosion.

Meshing of the fluid domain of the rig is done using ICEM CFD. GCI technique [5] is used to carry out the mesh sensitivity study. During experiments, cavitation is controlled by maintaining the pressure in the smallest cross section of the rig between 200-250 kPa. However, some cavitations are induced inside the clearance gap of the guide vane. The numerical model does not contain any

cavitation model. The effect of the vortices developed from the leakage flow is inferred from the pressure, velocity and vorticity contours.

1.4 Summary of chapters

This thesis is divided into 8 chapters. This chapter contained background of the problem, objectives of the work, scope and limitations of the methodology.
Chapter 2 contains all the general theories used in this work, including background of the tools used and equations.
Chapter 3 contains a review related to the flow and erosion in Francis turbines. This chapter includes the previous works done in this field, along with the case study of sediment erosion in turbines of Jhimruk HPP.
Chapter 4 contains the PIV and CFD works carried out in one GV cascade rig.
Chapter 5 contains the CFD works carried out in three GV cascade rig.
Chapter 6 contains the CFD works carried out in the actual turbine. The analyses and summary of results obtained in Chapter 4, 5 and 6 are presented in the same chapters.
Chapter 7 gives the conclusion from the overall work along with future recommendation.
Chapter 8 reports the publications (title and abstract) done as a part of this work.

Chapter 2

Theories of turbine, erosion and measurements

2.1 Francis turbine

Francis turbines, named after an American Engineer, J.B. Francis are the most widely used medium head reaction turbines. These turbines are mixed flow type of turbines, since water enters the runner in the radial direction and leaves in the axial direction. The basic features of a Francis turbine are shown in Figure 2.1. Water from the penstock enters the spiral casing, which transfers it to the runner with uniformly decreasing cross-section to maintain constant flow velocity. In between the runner and the spiral casing, two sets of vanes are distributed in circular rings. The first set of vanes are called stay vanes, which transfers water to guide vanes and provides structural support to spiral casing. Stay vanes are designed to have a minimum influence on the flow. In other words, the conversion of hydraulic energy of water to kinetic energy inside stay vanes is minimum due to the assumption of free-vortex theory inside this region. Guide vanes, also known as wicket gates help to regulate the flow into the runner. They are accompanied with shaft on both sides, which changes the opening angle of the guide vanes. These shafts are connected to a regulating mechanism, which further connects to a servo motor controlled by a governor system. Depending upon the available flow and required load, the opening angle changes, keeping the rotational speed of the runner constant. A significant amount of hydraulic energy is converted into kinetic energy inside guide vanes. When the flow reaches the inlet of the runner, a part of the total pressure energy is converted into kinetic energy and the rest of the energy is converted inside the runner blades. The fraction of the converted energy inside the runner out of the total energy converted gives the reaction ratio of the turbine. Runners of Francis turbines rotate due to both impulsive (towards the first half) and reactive (towards the second half) action of the fluid. Runner blades are covered with upper crown plate (hub) and lower runner band (shroud), which rotate together with the blades. The runner is connected to a shaft, which rotates the generator at a constant rpm. A gap is maintained between rotating runner and stationary covers for rotation. To prevent the leakage of the water from this gap, labyrinth seals are present in hub

and shroud. Labyrinth seals help to minimize the leakage loss from the runner and balance hydraulic forces of the turbine. From the runner, water passes through a diffuser like structure, called as draft tube, which converts the remaining kinetic energy from the runner outlet to the pressure energy.

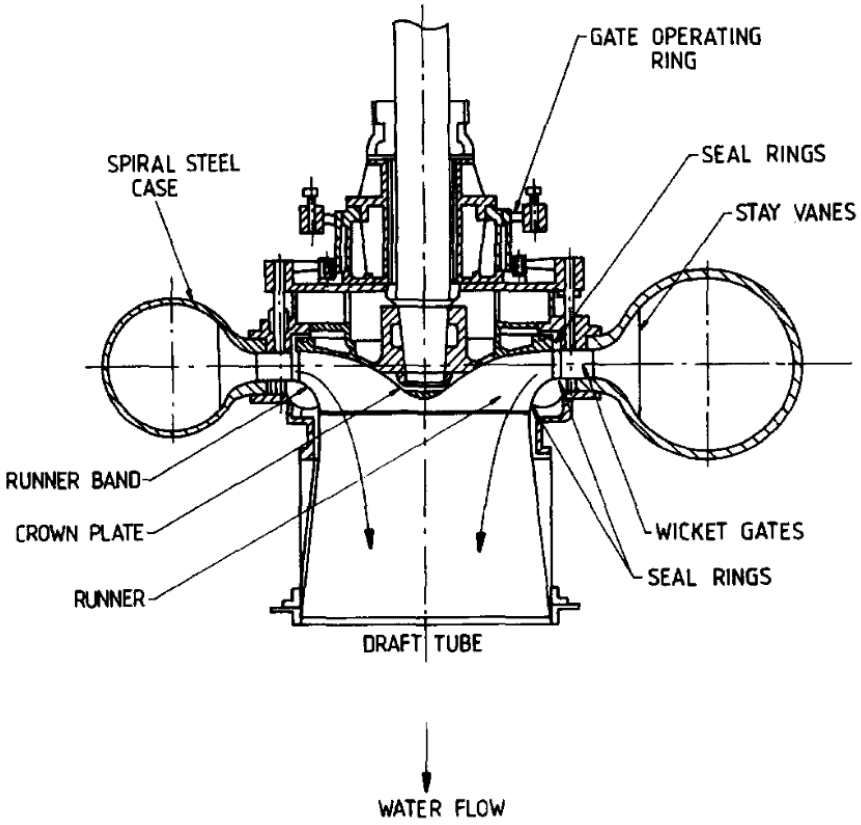

Figure 2.1: Basic features of a Francis turbine [6]

Figure 2.2 shows a velocity triangle at inlet and outlet of a runner blade. C and W represent absolute and relative velocity components of the flow respectively, whereas u represents tangential velocity of the turbine. Inlet and outlet sections are represented by suffixes 1 and 2 respectively. α and β represent angles made by absolute and relative velocity components with the tangential velocity respectively. C_u is the tangential component of the absolute velocity.

The general expression for the work done by a turbine, according to Euler momentum equation is given by:

$$\text{work done} = \rho.Q(C_{u1}.u_1 \pm C_{u2}.u_2) \tag{2.1}$$

Where Q is the discharge through the runner in m^3/s At best efficiency point (BEP), the no swirl component at the outlet of the runner is assumed ($C_{u2} = 0$). If H is the net head of the system and η_h is the hydraulic efficiency of the turbine,

$$\eta_h = \frac{\text{Power developed by the runner}}{\text{Power supplied to the turbine (water power)}} = \frac{\rho.Q(C_{u1}.u_1)}{\rho.g.H.Q} \tag{2.2}$$

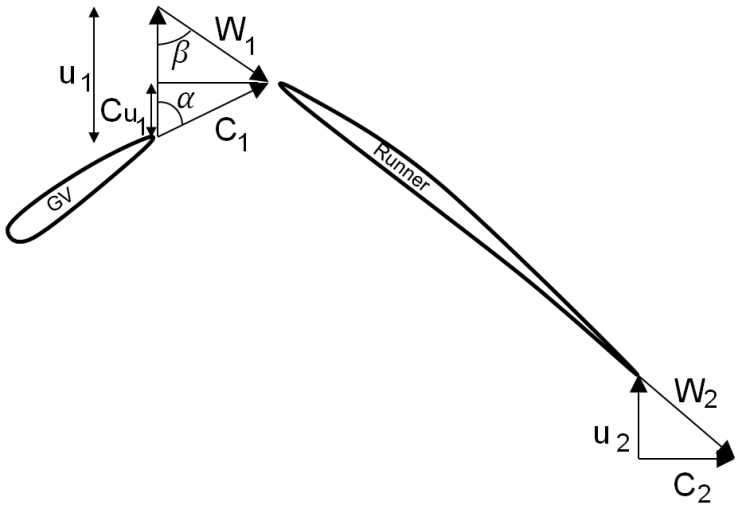

Figure 2.2: Velocity triangles at inlet and outlet of runner

The turbines are usually classified based on the available head and discharge, which gives the specific speed. According to IEC 60193 [7], the definition of the specific speed is according to the following formula:

$$\text{Specific speed} = \frac{\text{nQ}^{0.5}}{(\text{Hg})^{0.75}} \tag{2.3}$$

Where n is the rotational speed of the turbine in s^{-1}.

A sectional view of a Francis turbine is shown in Figure 2.3. From spiral casing, water enters into stay vanes (SV), guide vanes (GV) and runner. At part load conditions, when the speed of the runner tends to rise, GVs start to close, so that the net discharge decreases. Similarly, at full load conditions, GVs move towards opening direction. Similarly, depending upon part and full flow conditions, GVs close and open to maintain a constant rotation speed of the runner. To enable opening and closing of GVs, a shaft is connected between GVs and a regulating ring, which makes all the GVs rotate with a same angle. A small clearance gap (CG) is present between GVs and facing plates to allow free rotating movement without friction. This size of the gap grows due to deflection from water pressure on the covers, as well as wear of the GV and facing plate surfaces.

The arrangement of the GVs in a circular ring is shown in Figure 2.4. Due to different radial distance on the two adjacent sides of GVs at a same chord length, the GVs develop high and low pressure sides. The uneven pressure distribution produces a torque, which tends to rotate the GV around it's axis. In presence of the clearance gap (CG), the flow leaks from high pressure side to the low pressure side through the gap. This flow is termed as 'Leakage Flow' in this thesis. The leakage flow mixes with the main flow in suction side, disturbing the primary flow. Consequently, this accumulates more losses and also causes erosion in downstream turbine components.

In this PhD work, CFD and PIV measurements have been carried out in GV cascade rigs, which contains GVs oriented in circumferential position. The angular position of these rigs cover a portion of the total circumference of the GV ring. Figure 2.5 shows an example of the boundary of the

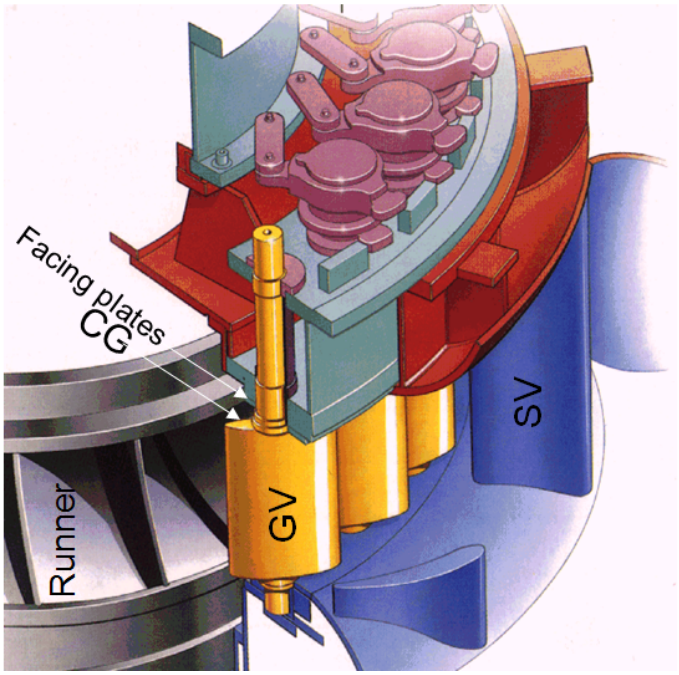

Figure 2.3: Sectional 3D view of a Francis turbine

measurement for one GV rig, which contains two guide vane passages (one on each side). The guide vane is oriented in the opening angle corresponding to the designed condition. The figure also shows the circumferential locations corresponding to stay vane outlet (SVout), guide vane inlet (GVin), guide vane outlet (GVout) and runner inlet (Rin) of the real turbine. The space between guide vane outlet and runner inlet represents vaneless region. The secondary flow in the form of wakes and leakages through clearance gaps undergo dissipation in this space before reaching the runner inlet. The dissipation of these flows can be visualized in between these two curves.

The velocities measured by PIV and calculated by CFD are in Cartesian co-ordinates initially, but are converted later to infer the flow condition of the real turbine. The velocities in Cartesian co-ordinate system is converted into the cylindrical co-ordinate system with the equations:

$$C_m = -(u\cos\theta + v\sin\theta) \tag{2.4}$$

$$C_u = (u\sin\theta - v\cos\theta) \tag{2.5}$$

The Cartesian velocity components u, v and the angle θ are explained in Figure 2.6. The terms C_u and C_m are the tangential and meridional components of the velocity, which are analogous to the real turbine. C_u component is responsible for the work done and power produced by the turbine, whereas C_m component is responsible for the directing the flow downstream.

To quantify the leakage flow, a coordinate system containing the origin at the center of the turbine is considered, as shown in Figure 2.7. A GV is assumed with leading and trailing edges at points (X_1, Y_1) and (X_2, Y_2) respectively. A velocity vector, V is assumed at a point in the chord length of GV. This vector can be resolved in velocities u and v with respect to the global coordinate system. α

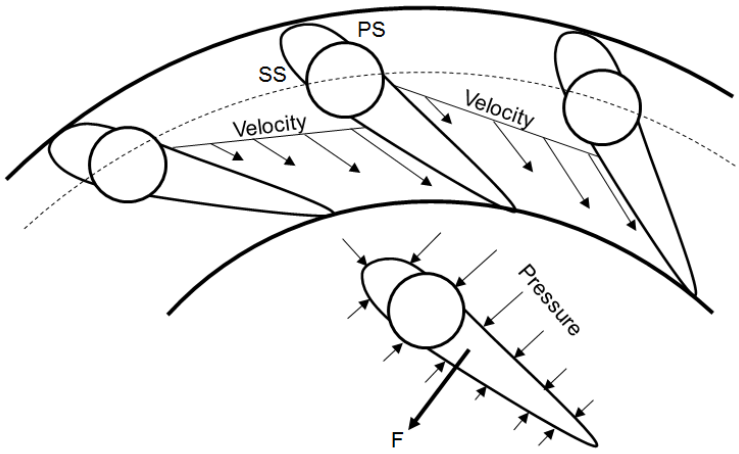

Figure 2.4: Orientation of GVs and velocity and pressure distribution

represents the angle of the chord and β represents the direction of the velocity vector, with respect to horizontal. A local coordinate system $x'y'$ is assumed along the chord length of GV, such that V'_x is the velocity component along the chord length of GV and V'_y (or simply Vy in next chapters) is the velocity component perpendicular to the chord length. The conversion of the coordinate system is based on following equations:

$$\alpha = \tan^{-1}\left(\frac{Y_2 - Y_1}{X_2 - X_1}\right) \tag{2.6}$$

$$\beta = \tan^{-1}\left(\frac{v}{u}\right) \tag{2.7}$$

$$V'_x = V.\cos(\alpha + \beta) \tag{2.8}$$

$$V'_y = V.\sin(\alpha + \beta) \tag{2.9}$$

In the region inside the clearance gap, Leakage Flow Factor (L_{ff}) has been defined in this study as the sum of the velocity component normal to the guide vane chord from leading edge to trailing edge, compared to a reference velocity.

$$L_{ff} = \frac{\sum_{i=(X_1,Y_1)}^{(X_2,Y_2)} \mid V'_y \mid}{n. \mid V_o \mid} \tag{2.10}$$

Where V_o is the reference velocity, n is the number of the points taken and L_{ff} is the leakage flow factor. In this study, the reference velocity is taken as the velocity at stay vane outlet (SVout). In the ideal scenario, the flow is directed along the chord, such that V'_y is zero. The pressure difference between the pressure and the suction side of the guide vane results in the velocity component in the direction normal to the chord. The absolute value in the numerator takes into account the negative leakage flow and avoids canceling with the positive values.

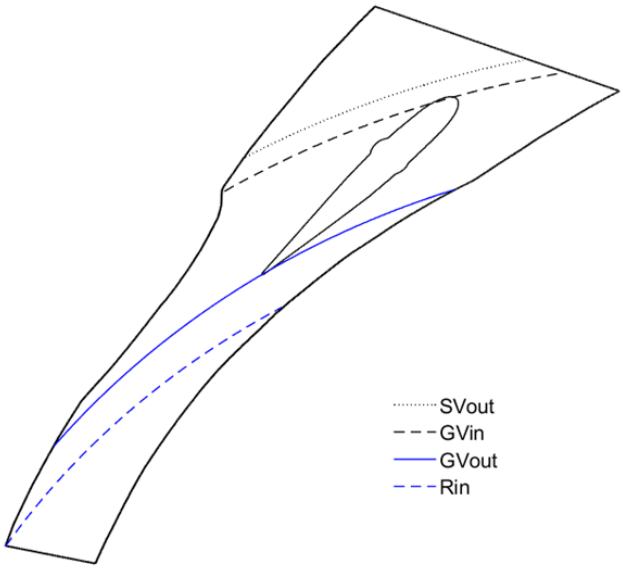

Figure 2.5: Boundary of the rig, measurement locations

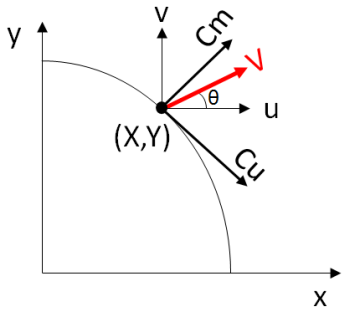

Figure 2.6: Tangential and meridional velocity components

2.1.1 Hydrofoils for guide vanes

This study compares GVs with different NACA profiles. NACA0012 is the reference hydrofoil, which is symmetric along the chord and has the maximum thickness of 12% of the chord length at 30% chord. Jhimruk HPP currently uses the reference hydrofoil shaped guide vanes and the test rig present in the lab was designed according to this profile [4]. NACA1412, NACA2412 and NACA4412 are the cambered hydrofoils with similar configuration as the reference case, but has camber of 1%, 2% and 4% respectively at 40% chord. NACA63212 has the maximum thickness of 12% at 35% chord and the maximum camber of 1.1% at 55% chord. The thicknesses of all the GVs are equivalent to avoid the change in the flow condition due to the area of the passage.

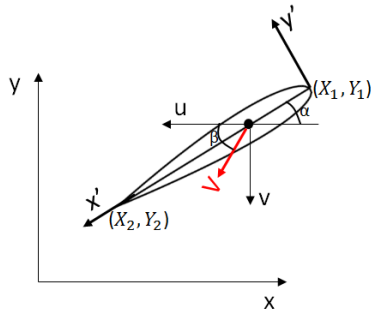

Figure 2.7: Velocity components in the axis of the chord

2.2 Sediment erosion

Erosive wear or erosion is one form of wear caused by the impacts of solid or liquid particles on a solid surface. The flow medium contains particles that possess enough kinetic energy to damage metallic surface. The mechanism of the erosive wear is quite similar to the abrasive wear, but in the case of the abrasive wear, the eroding agent is much bigger in size and the angle of impingement is lower. The erosive wear on the other hand, is accompanied with relatively small particles with several number of wear mechanisms. These mechanisms are differentiated based on the impingement angle, size, shape and speed of the particles and mechanical properties of the base material. Stachowiak and Batchelor [8] have discussed seven different possible mechanisms for solid particle erosion, including abrasive erosion, surface fatigue, brittle fracture, ductile deformation, surface melting, macroscopic erosion and atomic erosion. In the case of hydraulic machinery, the first four mechanisms out of the seven are applicable. A low angle of impingement is favorable for the abrasive wear, as the particles are drawn across the surface after the impact. Similarly, if the speed is low, the stresses at impact are insufficient for plastic deformation or brittle fracture, which induces surface fatigue depending upon the endurance limit of the base material. If the shape of the eroding particle is blunt or spherical, the plastic deformation is more likely to occur, whereas, if the particles are sharp, the cutting or abrasive wear is more common. The basic factors affecting wear of hydraulic machines are: i) the properties of the solid particles (sand) like hardness, size, shape, relative density and concentration, ii) properties of the eroded material like composition, structure and hardness and iii) the operating condition like flow-speed, temperature and impact angle.

Velocity of the fluid carrying particle and impingement angle are characteristics which affect wear significantly. The most general expression for erosion with respect to velocity is written as, Erosion $\propto$ (Velocity)^{n}, where n depends on the material and operating conditions. This value is mostly taken to be 3, but Truscott [9] reported different value of this exponent, for instance 1.4 for steel St37 to 4.6 for rubber. According to IEC 62364, the hydro-abrasive erosion depth in a Francis turbine can be estimated in mm by using following equation [10]:

$$S = \frac{W^{3.4} \times PL \times K_m \times K_f}{RS^{p}} \tag{2.11}$$

Where, PL(Particle Load) is the integral of the modified particle concentration over time.

$$PL = \int_0^T C(t) \times K_{size}(t) \times K_{shape}(t) \times K_{hardness}(t)dt \tag{2.12}$$

W is the characteristic velocity. In the case of guide vanes, it is the flow through the unit divided by the minimum flow area at the guide vane apparatus at best efficiency point (W_{gv}).

$$W_{gv} = \frac{Q}{\alpha \times Z_0 \times B_0} \tag{2.13}$$

Q is the discharge, α is the average shortest distance between adjacent guide vanes. Z_0 is the total number of guide vanes in a turbine and B_0 is the height of the distributor in a turbine. In the case of runner, it is the relative velocity between the water and the runner at best efficiency point (W_{run}).

$$W_{run} = \sqrt{u_2^2 + c_2^2}, u_2 = n \times \pi \times D, c_2 = \frac{Q \times 4}{\pi \times D^2} \tag{2.14}$$

K_m is the material factor, which characterizes how the hydro-abrasive erosion relates to the material properties of the base material
K_f is the flow coefficient $\left[\frac{mm \times s^{3.4}}{kg \times h \times m^{\alpha}}\right]$, which characterizes how the hydro-abrasive erosion relates to the water flow around each component
RS is the turbine's reference size in [m], which is the reference diameter (blade low pressure section diameter at the band) for the case of Francis turbines.
p is the value of the exponent, which is 0.25 for guide vanes, facing plates and runner inlet, whereas 0.75 for labyrinth seals and runner outlet.
C is the concentration of particles in [kg/m^3].
K_{size} is the size factor (median particle size d50 in [mm]), K_{shape} is the shape factor (Round = 1, Subangular = 1.5 and Angular = 2) and $K_{hardness}$ is the hardness factor (fraction of particles harder than Mohs 4.5 for stainless steel).

2.3 Particle Image Velocimetry (PIV)

Particle Image Velocimetry (PIV) is a flow visualization technique, which allows for capturing velocity field in a flow by tracking the particles inside the flow within a short interval of known time. Being a non-intrusive technique, PIV is gaining more popularity in aerodynamic and turbomachinery applications. By using advanced cameras and lasers, the flow around boundary layers can also be analyzed using this technique. An example of the experimental arrangement for PIV is shown in Figure 2.8. Flow is mixed with tracer particles, with density usually similar to that of flow, so that the velocity of the tracer particles and the fluid is similar. These particles are illuminated in a plane at least twice within a short interval of known time. The light scattered by these particles are recorded at those times. The displacement of particles within these frames and within the known time step gives the velocity vector. The area captured by the camera is divided into sub-areas, called interrogation areas, such that the velocity vectors could be determined for each interrogation area.

Each interrogation area consists of several tracer particles and in determining the velocity vector, it is assumed that all particles move homogeneously between two illuminations. In reality, the particles might travel unevenly inside the interrogation area, and some of the particles might move out of the plane within the two frames. The raw images are hence, processed using statistical methods to find the highest correlation between the position of the particles in the two frames. In the case of weak correlation, the interrogation area might contain an erroneous vector, which is termed as bad vector. A weak correlation might be generated due to several factors such as insufficient particles inside an interrogation area, too large time steps, insufficient illumination of the particles or improper focus by the camera. If the number of the bad vectors is within a tolerable limit, interpolation techniques or average from several image pairs (in case of steady analysis) are applied to repair them.

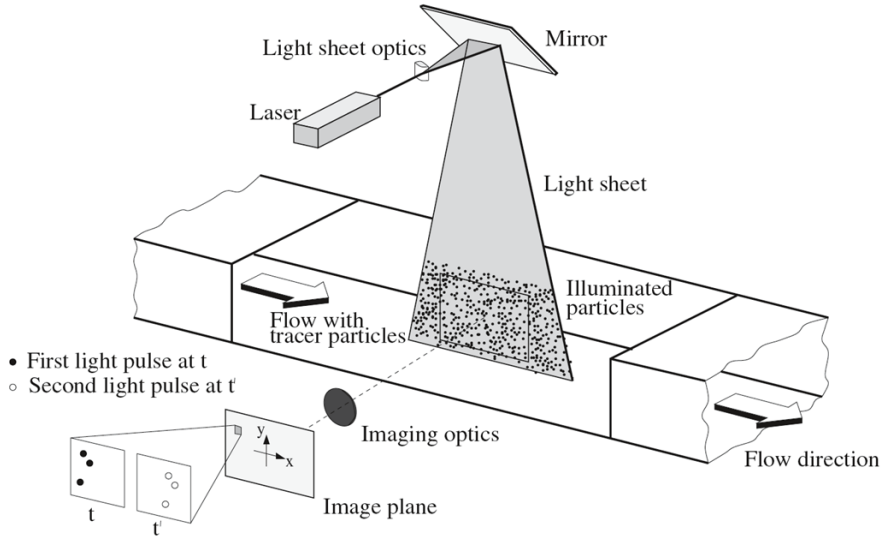

Figure 2.8: General layout of PIV measurement [11]

An average spatial shift from one image to the second image can be described with a linear digital signal processing model, as shown in Figure 2.9. The function f(m,n) is the light intensity within the interrogation area recorded at time t, and the function g(m,n) is the light intensity recorded at time t + Δt. The output image can be considered as the result obtained from the transfer function s(m,n) including the noise function d(m,n). The capitalized functions represent Fourier transforms of the corresponding lower case functions, and (u,v) represents co-ordinates in the spatial frequency domain. The major task in PIV is the estimation of the spatial shifting function s(m,n) on the basis of the measured values, f(m,n) and g(m,n).

In cross-correlation technique, the discrete cross-correlation function ϕ_{fg} (m,n) of the sampled regions f(m,n) and g(m,n) is given by the expected value:

$$\phi_{fg}(m, n) = E[f(m, n), g(m, n)] \tag{2.15}$$

$$\phi_{fg}(m, n) = \sum_{k=-\infty}^{k=\infty} \sum_{l=-\infty}^{l=\infty} f(k, l).g(k + m, l + n) \tag{2.16}$$

Figure 2.9: Image displacement function

A high cross-correlation value is observed, where the particles match up with the corresponding spatially shifted partners (true correlations), whereas small cross-correlation peaks may be observed with the particles match up with other particles (random correlations). In practise, Fourier transforms are used in PIV to speed up the cross-correlation process.

When the initial and final particle-positions are not possible to be obtained in separate camera frames, auto-correlation techniques are used. The successive light-sheet pulses expose one camera image map, and the recorded image is correlated with spatially shifted versions of itself. Auto-correlation produces larger central peak in the correlation plane compared to cross-correlation technique because the recorded image is correlated with itself. However, this technique might lead to ambiguity in the measurements, since it is not possible to track the initial and final positions of the particles.

2.4 Computational Fluid Dynamics (CFD)

The simulations carried out in this study uses a 3D-Reynold's Averaged Navier Stokes to solve the governing equations for an incompressible and isothermal flow. The governing equations (equation of continuity and momentum) for an incompressible and isothermal fluid are written in the form of Navier-Stokes equations given as:

$$\rho\left(\frac{\delta\vec{V}}{\delta t} + (\vec{V}\Delta\vec{V})\right) = \rho\vec{g} - \Delta p + \mu\Delta^2\vec{V} \tag{2.17}$$

Where,

$$\Delta^2 = \frac{\delta^2}{\delta x^2} + \frac{\delta^2}{\delta y^2} + \frac{\delta^2}{\delta z^2} \tag{2.18}$$

This equation has four unknows: velocity components in all directions, velocity $\vec{V}$ and pressure p. This is a highly non-linear Partial Derivative Equation (PDE), which generally requires computational approaches to solve. This study follows Reynolds average method, where a variable, for example, u_i is divided into an average component, $\bar{u_i}$ and a fluctuating term, u_i'. The substitution of these new terms in the original transport equation gives:

$$\frac{\delta\bar{u_i}}{\delta x_i} = 0 \tag{2.19}$$

And,

$$\frac{\delta \bar{u_i}}{\delta t} + \bar{u_j}\frac{\delta \bar{u_i}}{\delta x_j} = -\frac{1}{\rho}\frac{\delta \bar{p}}{\delta x_i} + \frac{\delta}{\delta x_j}\left(\nu\frac{\delta \bar{u_i}}{\delta x_j} - \overline{u_i' u_j'}\right) \tag{2.20}$$

Where, u_i = time-averaged velocity components, p = time-averaged pressure, ρ = fluid density, ν = fluid kinematic viscosity, u_i' = fluctuating velocity components, t = time

The Reynold's averaging does not change the continuity equation, but this will result in an additional stress term acting on the mean flow due to the fluctuating velocity, which are called Reynold's stress, $\tau_{ij} = -\overline{u_i' u_j'}$. These terms arise from the non-linear convective term in the un-averaged equations and represents the effect of the turbulence on the mean flow. Consequently, the governing equation contains 6 unknowns, which are solved using different turbulence models.

The RANS turbulence models can be divided into eddy-viscosity models and Reynolds stress models. The eddy viscosity model assumes that the Reynolds stress is related to the mean velocity gradients and eddy (turbulent) viscosity by the gradient diffusion (Boussinesq) hypothesis, such that:

$$\tau_{ij} = -\overline{u_i' u_j'} = \nu_t\left(\frac{\delta \bar{u_i}}{\delta x_j} + \frac{\delta \bar{u_j}}{\delta x_i}\right) - \frac{2}{3}\left(k + \nu_t\frac{\delta \bar{u_k}}{\delta x_k}\right)\delta_{ij} \tag{2.21}$$

$k = 1/2(\overline{u_i' u_j'})$ = turbulent kinetic energy, δ_{ij} = Kronecker delta, ν_t = Turbulent or eddy viscosity

In two-equation eddy-viscosity turbulence models, the velocity and turbulent length scale are solved using two separate transport equations, one for kinetic energy, k and one for turbulent dissipation rate, ϵ, or the specific dissipation rate, ω. In $k-\epsilon$ model, the turbulence viscosity, ν_t, is related to the turbulence kinetic energy, k and the dissipation rate, ϵ by the relation:

$$\nu_t = C_\mu\frac{k^2}{\epsilon} \tag{2.22}$$

Where, C_μ=Constant [12].

Although $k-\epsilon$ model was used widely for its robustness and faster computations compared to other turbulence models, the model shows limitations in adverse pressure gradient, flow containing separations, rotation and near wall regions. In the near wall boundary region, $k-\omega$ gives more accurate result, but this model is strongly sensitive outside the boundary layer. A blending between the $k-\omega$ model near the boundary and $k-\epsilon$ model in the free stream was developed by Menter [13]. BSL turbulence model was introduced as the first step by introducing a blending function F1. In addition to this function, the SST model accounts for the transport of the principal turbulent shear stress in the prediction of the eddy-viscosity.

In this thesis, the mesh sensitivity study has been carried out using GCI method [5]. It is a method to estimate the error associated with discretization in CFD. The simulations are carried out in three significantly different sets of grids, such that the grid refinement factor $r = h_{coarse}/h_{fine}$ is greater than 1.3. For three-dimensional calculations,

$$h = \left[\frac{1}{N}\sum_{i=1}^{N}(\Delta V_i)\right]^{1/3} \tag{2.23}$$

Considering $h_1 < h_2 < h_3$ and $r_{21} = h_2/h_1, r_{32} = h_3/h_2$ and ϕ be any variable measured, the extrapolated value, based on medium and fine mesh can be estimated from:

$$\phi_{ext}^{21} = \frac{r_{21}\phi_1 - \phi_2}{r_{21} - 1} \tag{2.24}$$

The errors can be estimated using following equations:

Approximate relative error,

$$e_a^{21} = \left| \frac{\phi_1 - \phi_2}{\phi_1} \right| \tag{2.25}$$

Extrapolated relative error,

$$e_{ext}^{21} = \left| \frac{\phi_{ext}^{21} - \phi_1}{\phi_{ext}^{21}} \right| \tag{2.26}$$

Fine-grid convergence index,

$$GCI_{fine}^{21} = \frac{1.25 \times e_a^{21}}{r_{21} - 1} \tag{2.27}$$

GCI_{fine} provides an estimation of the discretization error for the fine mesh. The same procedure can also be used to calculate the error for the medium mesh (GCI_{medium}).

Chapter 3

A Review on Flow and Erosion in Francis Turbines

Hydropower covers about 90% of the total renewable energy worldwide, used for electricity generation [14]. It has been shown that Asia covers largest potential for hydropower in the globe, with 6,800,000 GWh/year. However, the untapped hydropower in this continent is more than 70% of the total potential. The geological and climatic conditions also play an important role in accelerating the hydropower development. It is reported that out of 7×10^9 tons of suspended sediment carried to the ocean yearly from all rivers globally, about 70% is derived from southern Asia [2].

Due to excessive sediment and hard mineral contents in it, the turbines in the power plants under Himalayan River faces operation challenges due to erosion [3]. Although the problem is predominant in South Asia, other parts of the world, such as Europe and South America are also continuously facing the consequences of sediments [15]. In one of the power plants in Switzerland (1×2.6 MW Pelton turbine and 7×0.4 MW Girard turbines), the efficiency dropped by about 4% during only six days of sediment season [15]. In a power plant in Northern India (1×130 MW Francis turbine), the turbines are maintained every year due to the sediment concentration of 500 to 600 ppm in its river [16]. In the same power plant, the average erosion rate of 4.5 mm/year was measured in the runner blades. An economic impact analysis was calculated from a power plant in Colombia (10 MW Francis turbine), which showed a total loss (including efficiency loss, material loss, repair and management) of more than 12 million US Dollars per year for the electricity value of 0.17 US Dollars per KW-h [17].

3.1 Wear and Erosion

Erosion can be classified under one of the various forms of wear. According to the standard of ASTM 640-88, wear is defined as “damage to a solid surface, generally involving progressive loss

of material, due to relative motion between that surface and a contacting substance or substances." Hence, the major cause of wear and energy dissipation is friction and it is estimated that one-third of the world's energy resources in present use is needed to overcome friction in one form or another [8]. The classification of the wear, in recent years have taken a very broad concept, compared to 1950's, when only adhesive, abrasive, surface fatigue and corrosion were considered as the types of wear [18]. The addition of erosion by solid particle and droplet impact were done by Bhushan [19]. The wear rate, which is the rate of material removal, depends upon the geometry of the interacting surfaces, types of interaction, material properties, load and surface pressure, surrounding temperature, humidity, atmosphere, surface properties and relative velocities between interacting surfaces [3].

A detailed survey on abrasive wear in hydraulic machinery was done by Truscott [9]. This study consisted of some of the critical findings related to the factors affecting wear that were studied in several works since 1950's. Brekke [20] characterized sand erosion in turbo-machines in three categories: i) Micro erosion, where fine particles with grain size less than 60 μm strikes the turbine surfaces with high velocity, ii) Secondary flow vortex erosion, caused by obstacles in the flow field or secondary flow in the corners of conduits and iii) Acceleration erosion, where acceleration of particles normal to the flow direction separates the particles from the flow direction and collide with the surface.

Laboratory tests conducted by Wellinger and Stauffer [9] show that for metals in general, wear increases rapidly once the particle hardness exceeds that of the metal for both scouring and impact abrasion. While most literature [21] state that in general, the absolute wear rate increases with grain size and sharpness, Wellinger and Worster [9] state that wear is directly proportional to size for sliding abrasion, but is independent of size for direct impact. Wellinger also shows the effect of particle shape, with angular grains causing about twice the wear as compared to the round ones. Although the particle shapes are described qualitatively such as round, angular and semi-round, the actual shapes of particles are complex and cannot be quantified in simple mathematical terms. In the case of river sedimentation, concentration of particles is expressed in terms of ppm (parts per million), which is equivalent to mg/liter or kilogram of particles in 1000 m^3 of water. It is mostly accepted that the wear increases with the concentration of particles [22]. Similarly, the increase in the temperature of the operating condition softens the material and hence the erosion rate increases. The conveying medium such as air, water or oil also plays a significant role on erosion rate depending upon their density, viscosity, nature of the flow (laminar or turbulent) and microscopic properties. Stachowiak and Batchelor [8] show that small amount of lubricant in the liquid medium reduces erosion rate due to restriction in the change in material properties during particle impingement.

The erosion resistance of a material is seen to depend upon the material hardness and the impingement angle. Some materials such as cobalt have a very good erosion resistance at low impingement angle but the resistance decreases severely once the impingement angle is high [8]. The formation of the martensites results in the improved hardenability and erosion resistance except at low impingement angles and in the case of low allow steels, the ferritic phase with sufficient spheroidal carbide to induce strengthening is very effective against erosion wear. The erosion resistance of austenitic steels (21Cr4Ni) strengthened with Nitrogen was seen to be higher than a martensitic steels (13Cr4Ni) due to the distribution of hard carbides in the matrix of stabilized austenite [23]. Some materials such as ceramics are recommended for applications where the working temperature is high. However, these materials are brittle and might result in the brittle fracture. In the case of hydro turbines, the

prevention of the erosion is also done by applying coating on the surfaces of the vulnerable regions. The most common type of the coating is the Tungsten-Carbide (WC-Co), that uses 86-88% WC and 6-13% Co [6]. These coatings have excellent hardness, with better adhesion and large toughness.

3.2 Erosion in Francis turbines

Brekke [20] has classified the erosion in several components of this turbines which includes, i) The inlet valve system, ii) The spiral casing, iii) The pressure relief and/or by pass system, iv) The guide vane system, v) The runner and runner seals, vi) The draft tube and vii) The shaft seal. In Francis turbines, the highest absolute velocity is found to be at the guide vane outlet. It is the region where the maximum hydraulic energy of water is converted into kinetic energy, producing highly unsteady flow. The velocity distribution inside Francis turbine operating in best efficiency point is shown in Figure 3.1a). It shows that before the flow reaches at the inlet of the runner, about 50% of the potential energy is converted into kinetic energy. The kinetic energy increases from about 10% to about 50% from guide vanes inlet to the runner inlet for a high head Francis turbine. This infers that the flow should contain very high acceleration inside the guide vane. Such high acceleration results in secondary flow, aggravating the erosion problems in case of sediment carrying fluid. The erosion removes the material away from the surface, causing more disturbances in the flow. Figure 3.1b) shows an example (Lio Power Plant, 45 MW) of efficiency drop due to increase in the clearance gap from erosion [24]. The guide vane span in this case is 230 mm, and only by increasing the clearance gap by 1 mm (about 0.5% of the total span), the efficiency drops by about 2%. Similarly, highest relative velocity in Francis turbines is found at the runner outlet. This causes erosion at the runner outlet due to high turbulence. The minimization of erosion in Francis turbines, unlike Pelton turbine, significantly depends on the hydraulic design of the vanes other than the turbine material and coating. It can be found from literatures that several investigations have been carried out so far to minimize the erosion by changing the blade angle distribution of the runner blades [25][40][27].

3.2.1 Erosion in stay vanes

In stay vanes, the erosion occurs due to turbulences formed from high velocity. Although the velocity in stay vanes is less than in guide vanes and runner, the detached material from this region after erosion travels downstream, which causes more severe impact on the turbine.

3.2.2 Erosion in guide vanes

In guide vanes, the erosion can be classified into four types, based on the flow conditions. They are:

i) Turbulence erosion: Fine particles can erode the outlet of the guide vane due to high velocity, specially towards the suction side. At this region, the Reynolds number is in the order of 10^8, which

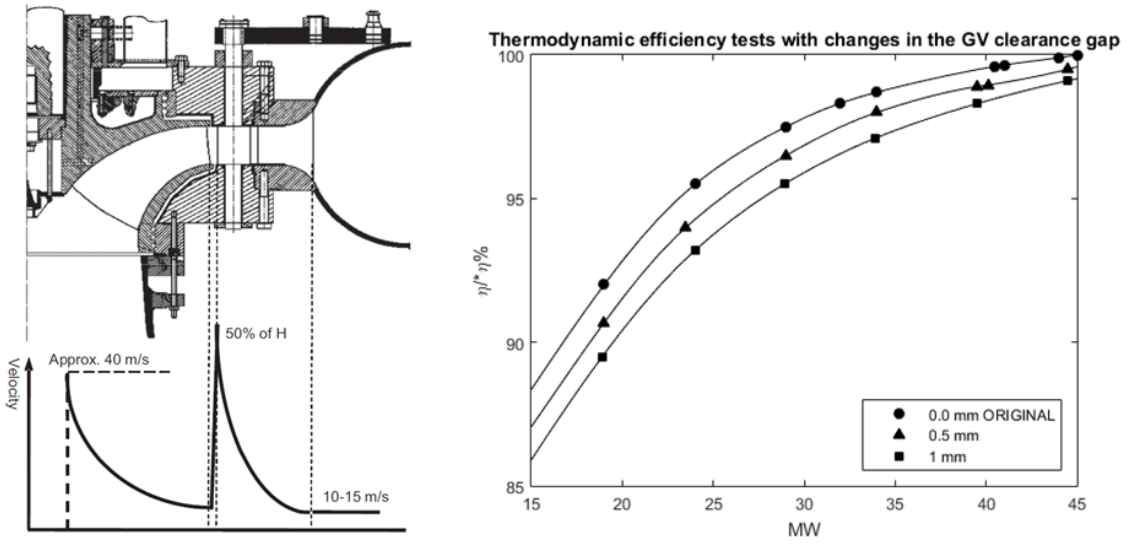

Figure 3.1: Velocity distribution inside Francis turbine [28] and Loss in efficiency due to clearance gap in guide vanes (Adapted from [24])

is under highly turbulent regime. At such a high turbulence, erosion can be severe on guide vane surfaces as well as on facing plates.

ii) Secondary flow: Guide vanes are accompanied with complex nature of the flow, which gives rise to several forms of vortices. In this case, secondary flow is referring to the accumulation of flow in the corner between facing plates and guide vanes, which gives rise to horseshoe vortex. These vortices increases the size of the gap, which brings more consequences as discussed in the next category.

iii) Leakage erosion: Guide vanes are accompanied with a small clearance gap at both ends to adjust the opening angle based on various operating conditions. In the case of sediment affected power plants, the hard fine particles mixed in water erode the connecting ends due to horse-shoe vortices. This erosion together with the head cover deflection due to water pressure increases the size of the gap. Due to the adjacent pressure and suction sides in guide vane, the flow passes through the gap from high pressure side to low pressure or suction side. At high acceleration, when the sediment particles enter in to the gap, it further causes abrasion on the guide vane ends and facing plates. This leakage flow disturbs the main flow in the suction side, which can be observed in the form of a vortex filament.

iv) Acceleration erosion: The rotation of the water in front of the runner creates acceleration normal to the streamlines, which separates the coarse sand particles from the flow. This impacts the steel surface, which could lead to catastrophic destruction in the guide vane surfaces.

3.2.3 Erosion in runner

In runner, the erosion can be classified into four types:

i) Turbulence erosion: In the runner, the highest relative velocity occurs at the outlet region. This increases the turbulence erosion due to fine sand particles.

ii) Acceleration erosion: The highest acceleration is found close to the blade inlet. As discussed in the erosion categories of guide vanes, due to acceleration normal to the streamlines, the coarse sand particles are detached from the flow, which causes erosion of both guide vane and runner inlet surfaces.

iii) Erosion due to incorrect stagnation angle: The inlet region is sensitive to incorrect pressure distribution and large difference in pressure between pressure and suction sides. The stagnation angle at inlet of the runner may change depending on different guide-vane opening angles. It is also seen that the leakage flow through the clearance gap of guide vane mixes with the main flow in suction side, which forms vortex filament that hits the runner blade near hub and shroud. This vortex pushes the stagnation angle, which not only erodes the corners, but also induces cavitation.

iv) Cross flow erosion: In some cases, cross flow from hub to shroud caused by incorrect blade leaning also increases horseshoe vortex in the blade roots. This may create sand erosion grooves at the blade inlet similar to guide vanes.

3.2.4 Erosion in labyrinth sealing

The clearance between the stationary and rotating parts in labyrinth seals is between 0.5 to 1.5 mm depending upon the size of the turbine [20]. The erosion is severe in this region due to a strong turbulence in the flow. Figure 3.2 shows the efficiency of Jhimruk HPP in an interval of two months. The total hydraulic efficiency loss after erosion in wet season is around 5%. At the same time, the leakage loss through the labyrinths was measured. It can be seen that the total loss due to leakage is between 2-4%. Hence, it can be inferred that the losses contributed by the leakage due to erosion of labyrinth seals is significant. Figure 3.3 shows some eroded components of Francis turbines. From

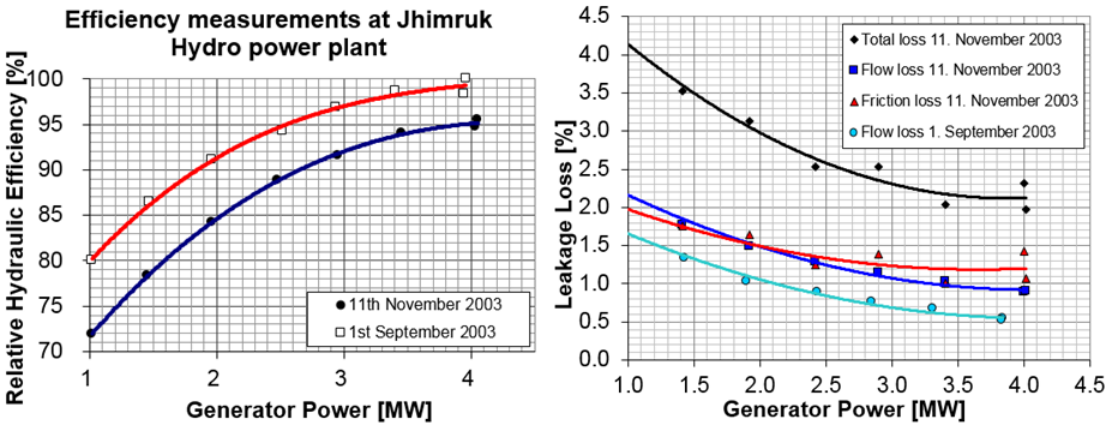

Figure 3.2: Efficiency measurements at Jhimruk HPP and losses from the leakage through labyrinth seal

these figures, it can be seen that the erosion in Francis turbine is predominant in particular places. The erosion depends on the nature of the flow in that location. In Figure 3.3a), erosion is shown at the outlet of the runner. It is the region where the flow leaves the runner with high relative velocity. Due to high turbulences, erosion occurs due to turbulence, as explained above. In Figure 3.3b), runner inlet towards the shroud end is seen to be more eroded than other places. This could be due to the incorrect stagnation angle driven by leakage flow through the guide vane's clearance gap. In Figure 3.3c) abrasion is occurring at the guide vane ends due to leakage flow. The connecting shafts are also heavily eroded due to flow separation towards the trailing side of the shaft. In Figure 3.3d) eroded grooves are formed on the facing plates due to horseshoe vortices. The grooves are formed within the range of some angles towards full GV opening. Hence, it can be inferred that these vortices affect the GV during full flow operation, for example, in the monsoon period, when the concentration of sediment in the flow is high.

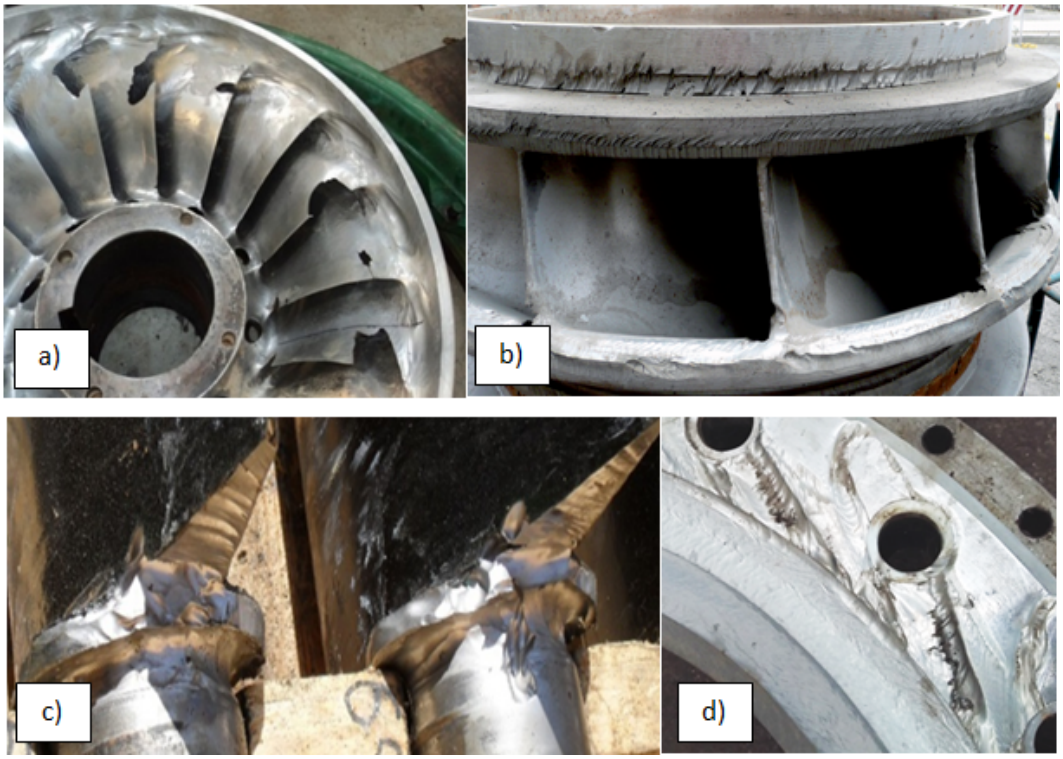

Figure 3.3: Erosion in Francis turbines at a) Runner outlet, Jhimruk HPP, b) Runner inlet, Cahua HPP, c) Guide vane faces, Middle Marsyangdi HPP, d) Facing plates, Jhimruk HPP (Picture Courtesy: O.G. Dahlhaug, R. Koirala)

3.3 Effect of the flow phenomena on erosion

Truscott [9] in 1971 performed a rigorous review on abrasive wear in hydraulic machinery and found the most common expression for wear, which was wear $\propto$ (velocity)^{n}. He also indicated that a lower

specific speed design at a given condition results a reduced wear, although that is more expensive and heavy. This study established a relationship between the flow and the wear in hydraulic machineries.

Later, Stachowiak and Batchelor [8] performed a more in-depth study of the wear mechanisms and its relationship with the particle material, angle of impingement, impact velocity and particle size. For ductile material, they found that the maximum erosion occurs at impingement angle of 30°, whereas for brittle material, it occurs at 80 – 90°. They also modified the expression between wear rate and impact velocity for medium to high speeds as $dm/dt = kv^n$, where m is the mass of worn specimen and n is the exponent whose value is between 2 to 3. They also explained the acceleration of erosive wear due to turbulence of the medium, as more particle impingement occurs than in laminar flow. This turbulence can be reduced by reducing the Reynold's number of the system.

There has been a number of empirical models developed so as to characterize the erosion in terms of fluid and material properties. Table 3.1 shows some of those models which are categorized under erosion in hydraulic machineries. Apart from some of the site specific models, general trend shows that erosion depends on the flow velocity, impingement angle, properties of the sand including shape, size, hardness and concentration, and properties of the eroded material. It can also be seen from this table that there are many ways to express the erosion or erosion rate of the material. Most common way is to define the erosion is in terms of the loss of material in mm/year [29][30][53], whereas, it is also expressed as mg/kg of eroding particles [3] and the depth of material eroded in mm [10].

Flow phenomena in Francis turbines are highly unsteady, and several studies have been conducted in order to predict and prevent the consequences of such flow behaviors. Trivedi et al. [32] showed the effects of transients on Francis turbine in terms of runner life, cost of plant operation and loss of power generation through experimental, numerical and analytical investigations. He explained that currently, Francis turbines are needed to operate over a wider range, approx. $\pm$30% away from BEP. However, turbines are generally designed to operate at the BEP and/or $\pm$5% of BEP. The turbines running at higher or lower operating point experience more wear.

Hasmatuchi et al. [33] performed an experimental investigation of the flow hydrodynamics of a radial pump-turbine under off-design conditions in turbine mode. A high-speed visualization was made as shown in Figure 3.4 with air bubbles injection in the vaneless space between guide vanes and the impeller in three operating conditions. It was seen that a uniform flow was obtained for normal operating conditions, but the flow pattern was disturbed due to vortices and backflows in runaway and low discharge cases.

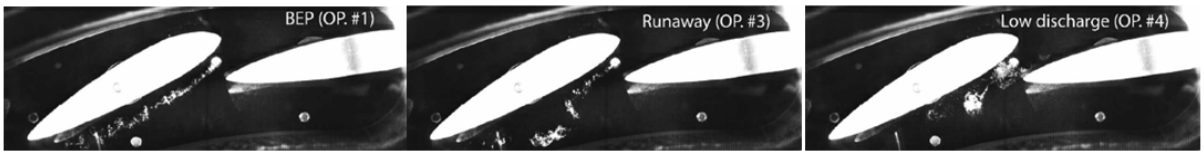

Figure 3.4: Vortex formations around guide vanes at different operating conditions [33]

Kobro [34] performed an onboard measurement of dynamic pressure in Andritz Hydro AG Francis runner of Tokke power plant. This analysis also showed that the wake leaving the guide vanes is

the most severe source of dynamic pressure in the runner. He also described that the level of pressure pulsations in the runner decreases as the clearance between the runner inlet and guide vane outlet increases. However, this increases the overall dimension of the turbine, leading to the cost disadvantage. Nicolet et al. [35] explained that the pressure field at the inlet of the runner is a combination of the guide vane outlet including wakes and non-uniform pressure distribution of the runner itself. This explanation is shown in Figure 3.5.

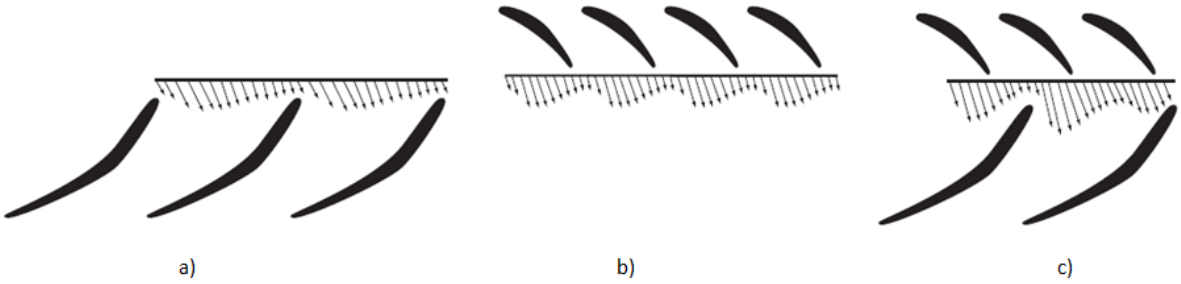

Figure 3.5: Distortion of the flow field at the inlet of runner due to a) Runner pressure field b) Guide vane wake c) Combination of the two effects [35]

Some advance techniques have emerged to measure the flow velocity and capture the flow structure, even in a very high velocity regions of Francis turbines. These techniques include Particle Image Velocimetry (PIV), Laser Induced Fluorescence (LIF) and Laser Doppler Anemometry (LDA). Finstad [36] studied the dynamics present in wake flow and RSI through experimental TRPIV (Transient Particle Image Velocimetry) from a hydrofoil in a stream of 9 m/s. This study also presented the effect of Vortex Generators (VG) on RSI and found a slight improvement of rotor leading edge pressure reduction at AoA = 0 and AoA =2. The experimental details of this study are shown in Figure 3.6.

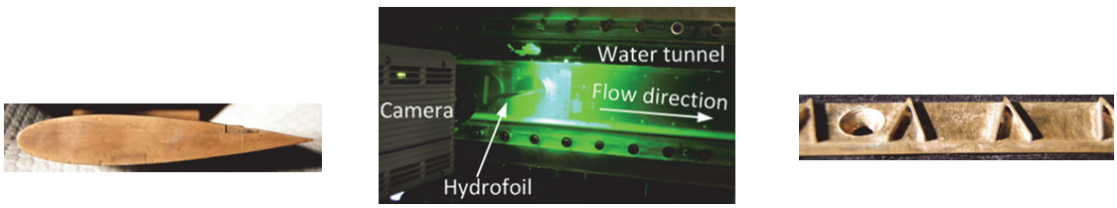

Figure 3.6: PIV experiment with a) Hydrofoil of chord length (k) 81 mm b) Setup with camera, water tunnel, hydrofoil and laser c) 1 mm V-shaped VG mounted on the suction side at x/k = 0.38 from the foil tip [15]

Su et al. [37] performed a PIV experiment in a complete Francis hydro-turbine model of diameter 0.15 m, with 15 runner blades, 24 guide vanes and 23 stay vanes. The visualization of the flow field inside the turbine was done by making some guide vanes and stay vanes transparent and drilling a hole on the casing at a corresponding position. The experimental setup and the result of this study is shown in Figure 3.7. It was seen that the main frequency of the flow around the guide vane was related to the Blade Passing Frequency (BPF).

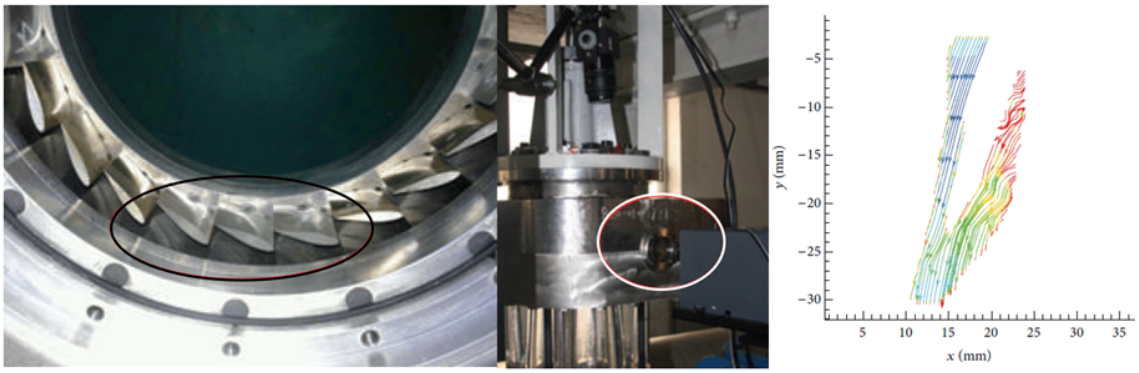

Figure 3.7: Experimental apparatus for PIV with a) Transparent guide vanes b) A hole drilled in casing and c) flow field observed around a guide vane [32]

Similarly, Laser Doppler Anemometry (LDA) measurements were conducted in a cascade rig with different guide vane profiles by Antonsen [38]. This study showed a direct relation between the pressure distribution at the inlet of the runner and the dynamic load due to RSI. Four guide vane profiles were compared, which showed that the one with an asymmetric profile with flat surface pointing the runner had more uniform pressure distribution than others. Figure 3.8 shows the cascade rig equipped with LDA, along with the results of the velocity deficit caused due to wake formation downstream of two guide vane profiles, compared with CFD results.

The review done in this section shows that the flow around the regions containing blades inside Francis turbines possesses several unsteady phenomena. Depending upon the properties of the particles carried by this flow, each of the phenomena results in surface erosion at different locations. Some state-of-the-art technologies have emerged over time to estimate the flow behavior inside a turbine. Although the results give a good indication of the behavior of the particles moving with the flow and how erosion occurs, sand particle tracking through experimental techniques have not been implemented so far. However, computational analysis to predict the particle tracking and erosion in turbine components are gaining popularity now-a-days [39][41][40], which are discussed in the next section.

3.4 Erosion quantification and its effect on flow

The purpose of this section is to understand the potential effect of the eroded profiles on the flow phenomena. When the turbine components are eroded, the surface roughness increases and this non-uniformity in the layer aggravates the flow, accumulating more losses. Although no such studies are recorded which derives a direct relationship between the eroded quantity and the consequent losses, there are some indications in few studies [42][20] that favors this statement that the losses are more severe in the case of erosion than smooth geometries. In fact, the quantification of erosion itself has been a challenging topic because of a large number of depending variables like a) particle shape, size, concentration, density and injection b) geometry, material and operating conditions of the turbine c) flow behavior. These variables make it difficult to predict the actual amount of erosion in the turbines

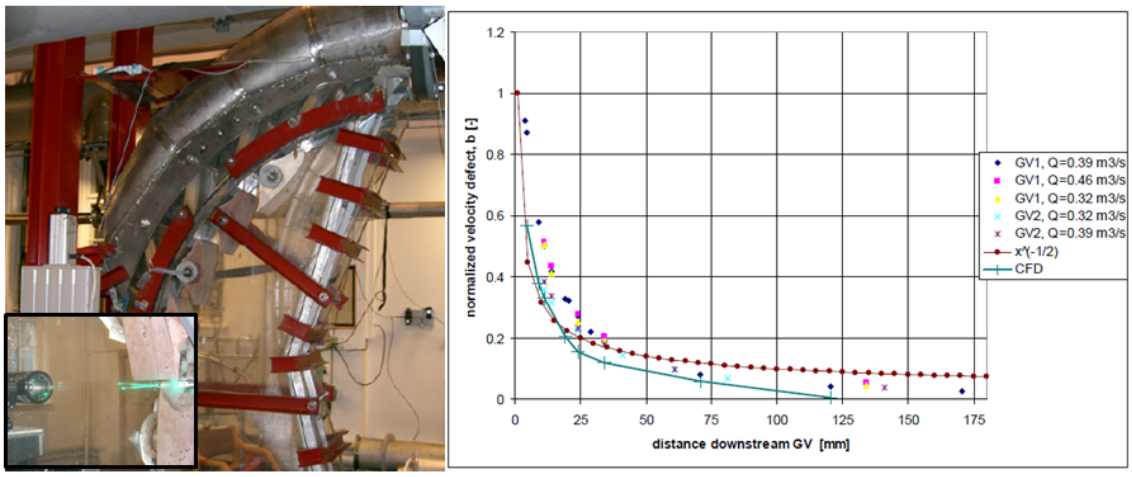

Figure 3.8: a) Cascade rig equipped with LDA b) Normalized velocity deficit from measurements compared to CFD [38]

in a real scenario.

Some attempts have been made in order to quantify the erosion in simplified models, such that their results can be mapped or approximated on actual circumstances. Thapa et al. [43] used Rotating Disc Apparatus (RDA), in which a disc or an arm is rotated in a mixture of erodent and fluid medium, to study the synergistic effect of sand erosion and cavitation. The effects were observed on a) Plain stainless steel and b) WC-Co-Cr ceramic coating applied by High Velocity Oxygen Fuel (HVOF). When cavitation inducers are fitted on the rotating disc, it was seen that in the coated specimens, as shown in Figure 3.9, the erosion groove increases the depth rather than propagating further. The combined effect was found to be more predominant than the individual effects.

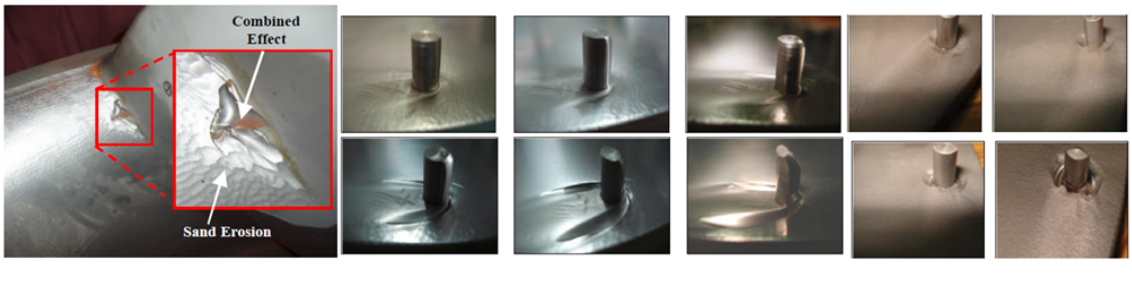

Figure 3.9: a) Combined effect of sand erosion and cavitation in the runner inlet b) Progressive erosion pattern in non-coated region in minutes: 30, 45, 60, 90, 180, 270 c) Progressive erosion pattern in coated region in minutes: 30, 90, 180, 270 around cavitation inducers [43]

Koirala et al. [44] used the RDA to conduct sediment sample and erosion potential analysis of Upper Tamakoshi Hydroelectric Project. The percentage of quartz content in the sand was found to be 62.18% for the size between 0.15 mm and 0.2 mm, but only 55.54% for the size less than 0.075 mm. The RDA was used to test the erosion potential of particles ranging from 0.075 mm to 0.2 mm

and it was seen that the rate of erosion is directly proportional to the particle size.

Decrease in efficiency due to increase in erosion of turbines was also recorded in Maneri Bhali Stage II (4 x 76 MW) [45]. The efficiency of one of the units was measured to decrease from 2.38% at 100% load to 4.87% at 50% load. In Kaligandaki HPP (3 x 48 MW), the size of the clearance gaps were measured in one of the units [46]. Towards leading edge, the average clearance gap was found to be 2.5 mm after 16,500 hours of operation, compared to the designed clearance gap of 0.6 mm. Towards trailing edge, the average increment was found to be 4.2 mm after 16,500 hours of operation. This shows that the pressure difference towards the trailing edge is higher than the leading edge, which results in high velocity of particles, causing more erosion at these regions. It was also shown that optimizing the guide vane's profile could minimize the overall erosion rates in guide vanes and increase the performance of the turbines [47].

Neopane [39] used the concept of critical diameter of the sand particles for showing the relationship between the sand size and the erosion. Above critical diameter, the particle remains rotating in the swirl flow hitting the guide vane wall, but the smaller particle flows through the turbines. Figure 3.10 shows that smaller turbines are more prone to erosion due to smaller critical diameter. The author also suggests that if the particle size is bigger than the critical diameter, the turbine should be avoided to operate at low guide vane openings.

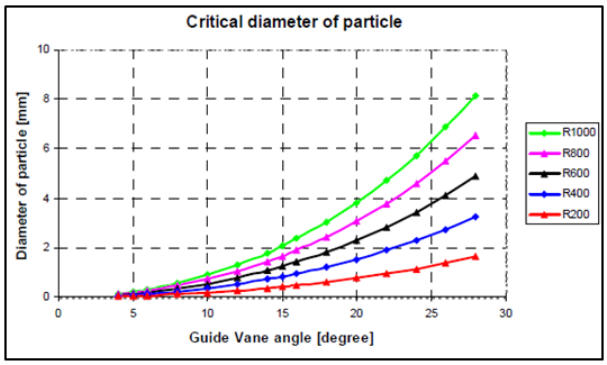

Figure 3.10: Critical diameter of the particle on the basis of turbine size [39]

The RDA setup was later modified by Rajkarnikar et al. [48] with a provision of testing erosion in Francis runner blades. Four blade models of Jhimruk Hydropower with a scaled down ratio of 1:4, and made up of Aluminum with 6% Copper and 4% Zinc, were fitted in the rotating disc as shown in Figure 3.11. It was found that the erosion occurred mostly in the far outlet region due to micro erosion from high rotational motion of the sand particles.

Guangjie et al. [49] used a thickness gauge to measure thickness on the runner blades and guide vanes over grid surfaces as shown in Figure 3.12, three times within 28 months. It was seen that the tungsten carbide coating on the surfaces wear in the following manner: a) 10.50 μm/month on the back of the runner blade b) 6 μm/month on the blade face c) 3.43 μm/month on the guide vanes face d) 1.79 μm/month on the back of the guide vanes.

Apart from the visual inspection, measurements of weight and loss of thickness in numerous

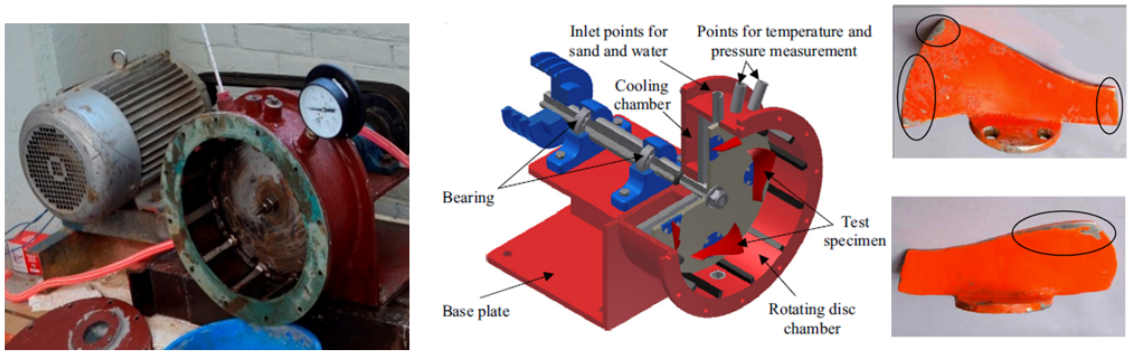

Figure 3.11: a) RDA apparatus b) Components of the apparatus c) Erosion pattern obtained on the blade [48]

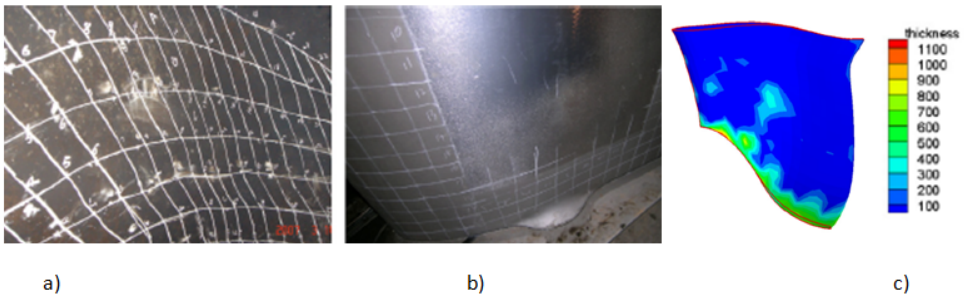

Figure 3.12: Mesh map of the a) Blade runner and b) Guide vane coating and c) Distribution map of the measured wear rate [49]

locations of the eroded surfaces, an advance technique of using 3D scanner exists now-a-days to quantify erosion. This technique was used by Rai et al. [50] to model an eroded Pelton bucket. Such techniques enable understanding the exact location of erosion and the quantity eroded in each location. This further facilitates numerical analysis to compare the flow dynamics between eroded and non-eroded profiles.

A common numerical approach for understanding the flow around hydraulic machineries is the use of Computational Fluid Dynamics (CFD) technique. By implementing an appropriate particle tracking method and erosion model, the erosion in any wall boundary can be predicted computationally. The prediction of erosion with this technique in Francis turbine is seen to be conducted in many studies [37][40][41].

The surface integrity deterioration caused by sand erosion not only deficits the efficiency of the turbine, but it also intensifies the cavitation. The study of Thapa et al. [43] showed that the combined effect of sand erosion and cavitation erosion is more than the sum of their individual effect. Later review work of Gohil et al. [51] also supported that the cavitation in sediment flow is more severe than in pure water. In case of Francis turbine runner, the regions of the occurrence of these two phenomena is different, as explained in Figure 3.13. The sediment erosion is more prone at the outlet due to turbulence of fine grain sand and at the inlet due to horseshoe vortex, incorrect blade leaning and acceleration of coarse sand particles. Cavitation, on the other hand, is a result of the implosion of

micro-jet bubbles formed due to low pressure.

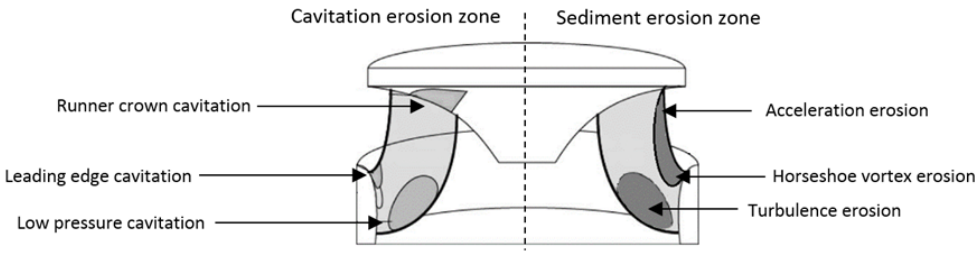

Figure 3.13: Cavitation and sediment erosion prone zones in Francis runner (Adapted from [51])

A one GV cascade rig was recently built to study the effect of the increasing clearance gap on the flow. The rig is capable to produce similar flow field around one GV, compared to that in real turbine. A 3D model of the rig is shown in Figure 3.14. The velocity field around the GV was measured using PIV technique. The figure also shows the sectional view of the GV in the test rig containing pressure taps for the pressure measurement. Although the measurements were taken in a 2D plane, the vortex moving out of the plane could be predicted by measuring at several span positions. Clearance gap was present at one end of the GV and other end was attached to the wall. Since the GV was divided into plexi and steel parts, the size of the clearance gap could be increased by milling the steel part. It was concluded from this study that the symmetric GV profiles are not suitable for sediment affected turbines because of bigger pressure difference and higher leakage flow through the gap [28].

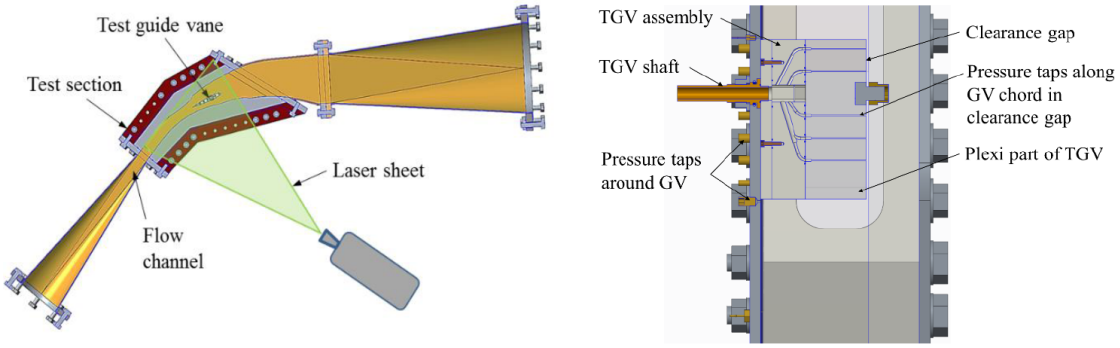

Figure 3.14: One GV cascade rig and sectional view of test section along GV chord [4]

3.5 Endeavors for minimizing the secondary flow and erosion

The simultaneous and combined effect of sediment erosion and secondary flow in Francis turbines also need multidisciplinary solutions. This means that each of these problems need to be tackled separately. The overcoming of one problem, however, aids for the minimizing of the combined effect, as the erosion has a direct influence on the flow and vice versa. This section reviews some of the important works done to minimize these effects separately.

Truscott [9] showed that in ferrous metals, very hard alloys such as Tungsten Carbide (WC) are extremely resistant to erosion. The paper also discusses about the effect of chemical composition, microstructure and work hardening on wear resistance of metals. It showed Austenitic Cr-Ni (12-14%), Mn alloy steels and Ni-hard (Ni-Cr) cast iron had a superior resistance to erosion.

Stachowiak and Batchelor [8] proposed that the wear resistance of a material can be improved from hardening of steel to form Martensite, except for low impingement angles and the formation of massive or lamellar carbides. They also suggested the inclusion of the ferritic phase with sufficient spheroidal carbide in low alloy carbon steels an effective method against erosive wear. The review work of Padhy [54] discussed about the benefits of HVOF coating over other techniques, but had demerits of micro cracking, de-bonding and digging out of WC particles. Also, plasma nitrided 12Cr steel performed better than plasma nitrided 13Cr-4Ni steel due to higher micro-hardness and ability to absorb more nitrogen [55]. However, for hydropower plants affected with sand particles, HVOF sprayed WC is the most optimum erosion resistance material to overcome low and high-energy erosive wear.

Apart from the properties of the eroding material, the wear rate also depends on the erodent properties. Desale et al. [56] performed experiments in a pot tester to evaluate the effect of erodent properties on ductile materials. The study showed that the erosion of ductile materials is not only a function of erodent size and hardness, but also of their shape and density, such that the particles with high density and low shape factor causes deep craters and high surface roughness. As the properties of the erodent cannot be controlled, the research works on materials and coatings became insufficient. Hence, the concept of 'erosion-friendly' turbines by changing the turbine design philosophy emerged as a new area of research to minimize erosion in hydraulic turbines.

The most common hydro-abrasive erosion resistant coating materials in hydraulic machines is thermal sprayed tungsten carbide cobalt chromium, WC-CoCr [57]. These coatings have a Vikers' hardness of 900 to 1200 HV at 0.3 kg loading [9], which is harder than feldspar (Mohs' hardness 6) and similar hardness as quartz (Mohs' hardness 7). Although it was difficult to apply coating on the surfaces of small and medium sized Francis runners, with recent technologies and use of robots, it has become possible to coat them completely. According to IEC 62364, coatings might initially result in reduction of the efficiency due to increased roughness, but can maintain a higher efficiency compared to the uncoated turbine over time.

A new production method was developed for Cahua HPP by applying a tungsten carbide based coating to Francis turbine runners and guide vanes [58]. The coated turbine increased the energy production by about 50 percent compared to the energy generated by the uncoated turbine during the same time period. However, most of the hydro-abrasive erosion resistant coatings are not effective against cavitation. A high intensity implosion of cavity might locally destroy the coatings. In addition, the dimensional tolerances of the coatings have to be considered before applying the right coating. Hard-coatings are also sensitive to impacts of larger particles, such as gravels and stones. Since the thickness of the coating is around 300 to 500 μm, it could also hinder the detention of potential cracks in the base material [59].

An effective maintenance strategy must be implemented to get maximum output from a power

plant. Frequent maintenance is required to run the turbines with good condition. Although power plants contain spare turbine parts, the downtimes during assembly and disassembly adds to the total cost, due to losses in electricity generation. Hence, design of turbines for easy dismantling, maintenance procedure and overhaul time is being continuously optimized for best production. These days, power plants employ pit stop maintenance for making the maintenance actions more efficient, saving both time and money. This philosophy implies more focus on preparation, planning, follow-up and evaluation than during shutdown maintenance. IEC 62364 gives some criteria to determine the overhaul time due to hydro-abrasive erosion. Some parameters are listed below:
i) When the efficiency has deteriorated to an extent that it is economically beneficial to restore the unit to its design efficiency.
ii) Water outflow through balancing pipes from the head cover indicating erosion of labyrinth seal.
iii) Increase in the axial thrust indicating erosion of labyrinth seal.
iv) The time taken by the unit to stop after the guide vanes are closed and the inlet valve are kept open, indicating erosion of the guide vanes and covers.
v) Pressure in the spiral casing with closed inlet valve and opened bypass, indicating erosion of the guide vanes and covers.
vi) For internal inspection, if runner blade outlet is eroded more than two thirds of its thickness (for large turbines) or completely abraded (for small turbines), clearance of the runner labyrinth is more than doubled and for coated surface, if the area of coating removed exceeds 5-10% of the total coated area.

Brekke [60] recommended some reshaping techniques at the outlet of guide vanes to minimize the oscillatory problems due to vortex shedding from blades. These techniques are: a) Skewed cut with an angle smaller or equal to 45° at the outlet edge measured relative to the pressure side of the vanes, and b) Avoid sharp corners with ± 3 mm wide skew cut parallel to the suction side of the next guide vane. Furthermore, he also recommended a negative blade lean at the inlet of the runner to minimize the cross flow from hub to shroud on the pressure side of the runner blades causing unstable swirl flow in the draft tube. This statement was also supported by Chitrakar et al. [61] through computational results that the blades with negative linear lean in high head Francis runner gives better performance with respect to the total pressure loss from end-wall effects.

Previous section of this paper also discussed about a study in which the investigation of the effect of Vortex Generator (VG) on a guide vane shaped hydrofoil was performed [36]. The results of this study also gave an indication of the improvement of the flow at some opening angles (AoAs). Similarly, an LDA experiment performed by Antonsen [38] on four different profiles of guide vanes showed that asymmetrical profiles with particular orientation gives more uniform pressure distribution at the outlet.

3.6 Case study of Jhimruk HPP

Jhimruk HPP (4.1 MWx3) is a run-of-river type power plant in Nepal operating at a net head of 201.5 meters and designed discharge of 2.35 m^3/s for each turbine. There are three units of horizontal Francis turbines running at 1000 rpm. The plant is facing severe operational and maintenance issues

due to excessive sediments in its river. The concentration of sediment varies with respect to the discharge throughout the year. Figure 3.15 shows the sediment concentration graph within a period of around 3 months between September and November. It shows that the problem of sediment is more predominant during wet season (between July – September), when the available discharge is maximum. Apart from excessive sediments, the percentage of quartz in sediment sample taken from this power plant was found to be between 60-70% [3].

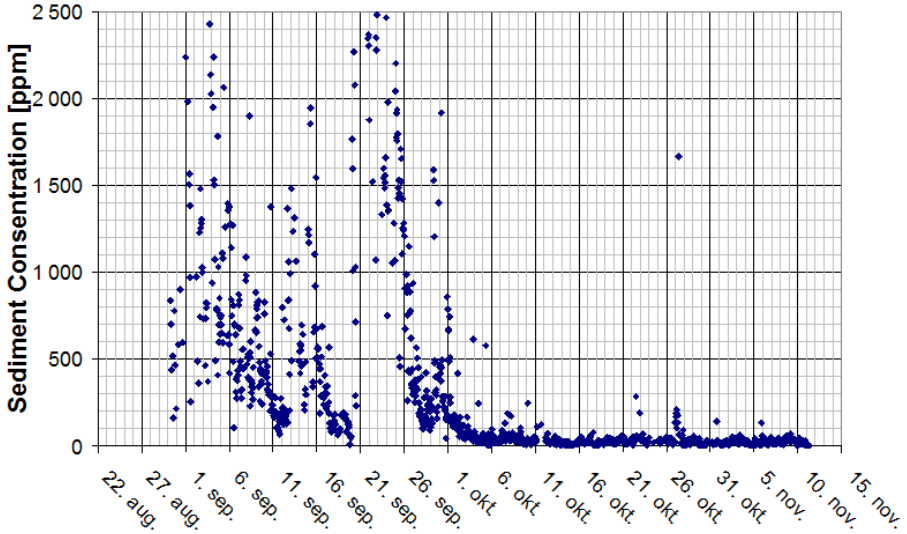

Figure 3.15: Sediment Concentration in Jhimruk HPP (Picture Courtesy: O.G. Dahlhaug)

Suspended sediments of size less than 0.5mm, which are not trappable, are mostly harmful for the turbines. These particles move together with the flow and because of the highly turbulent flow inside the turbines, the particles hit several components causing erosion. Out of the components that are eroded, guide vanes and runner are found to be most vulnerable. This is because of high velocity and acceleration in these regions. Figure 3.16a) shows the outlet of the runner, where erosion occurs due to high relative velocity of water containing sediments. Some past research works have shown that the erosion in these regions can be reduced by changing the blade angle distribution in the runner blade without affecting the efficiency of the runner [25][27]. Figure 3.16b) shows the inlet of the runner. A distinct erosion pattern can be seen towards the connecting ends between blades and hub/shroud. This paper focuses on investigating the cause of these erosion patterns. More discussions are shown in Figure 3.17. Figure 3.16c) shows an erosion pattern on the surface of the guide vanes. The eroded surface consists of ripple patterns, which is due to fine sediment particles. These patterns are also found in the needles of nozzle systems in Pelton turbines [30]. The formation of ripple might be due to the formation of Kelvin-Helmholtz vortices. Figure 3.16d) shows eroded facing plates due to horseshoe or corner vortices, aggravated by abrasion due to leakage flow through clearance gap of guide vanes.

In this thesis, more focus has been given to the cause and effect of the erosion in the clearance gaps of guide vanes. Figure 3.17a) shows erosion at one end of guide vanes. More erosion was found towards the second half of the chord, after shaft. One reason for such erosion is the high turbulence behind the shaft due to seperation of flow through the cylindrical shaft. Another reason is the abrasion

Figure 3.16: Erosion in different components of Francis turbines (Picture Courtesy: O.G. Dahlhaug)

Figure 3.17: Erosion at a) GV's facing ends b) Facing plates and c) Runner blade inlet (Picture Courtesy: O.G. Dahlhaug)

from the particles due to cross-flow or leakage flow inside the gap from one side to another. It has been found that the pressure difference between the adjacent sides of the guide vanes directly influence the intensity of leakage flow and consequently, the abrasion [28]. Figure 3.17b) gives a closer view of the erosion on facing plates. Horseshoe vortices are formed at corners between guide vanes and facing plates, forming eroded patterns in the shape of guide vane profile. Due to opening and closing of guide vanes, the eroded patterns are formed throughout the range of guide vane's opening angles. More erosion occurs on its surface due to continuous leakage flow through the gap. The erosion at the ends of guide vanes and the facing plates eventually increases the size of the gap. The gap size is also added by the deflection of the covers due to water pressure [62]. Figure 3.17c) shows closer view of the erosion at the inlet of the runner blade towards one of the edges. This erosion might have occurred due to the disturbances caused by the interaction of the leakage flow with the main flow. In some cases, cavitation might also occur because of the improper stagnation angle at these regions.

Table 3.1: List of some erosion models developed for hydraulic machineries

Model	Equation	Parameters
Tsuguo [29]	$W = \beta C^x a^y k_1 k_2 k_3 V^m$	• W=loss of material in mm/year • β=turbine coefficient at eroded part • V=relative flow velocity • a=average grain size coefficient on the basis of unit value for grain size 0.06 mm • k_1 =shape coefficient of sand particles • k_2 =hardness coefficient of sand particles • k_3=abrasion resistant coefficient of material • x and y=concentration and size coefficient
Thapa [3]	$y = 6E - 5x^{3.13}$	• x=velocity of eroding particles impinging at 45° • y=the loss of material in mg/kg of eroding particles striking the surface
Bajracharya et al. [30]	$E_r \propto a(size)^b$	E_r=rate of erosion in mm/year If Quartz content 38%, a = 351.35 and b = 1.497 If Quartz content 60%, a = 1199.8 and b = 1.802 If Quartz content 80%, a = 1482.1 and b = 1.812
Thapa et al. [53]	$E_r = CK_{hardness}K_{shape}K_mK_fa(size)^b$	• C=the silt concentration kg/m^3 • K_{shape}=shape factor • $K_{hardness}$=hardness factor • K_m=material factor • K_f=flow factor

Chapter 4

One GV Cascade Rig

This chapter consists of experimental and numerical study of the flow around guide vane (GV) in one GV cascade rig. Pressure and velocity measurements were carried out using pressure sensors and Particle Image Velocimetry (PIV) technique respectively. The numerical study consists of Computational Fluid Dynamics (CFD) analysis conducted in the same rig. The results of CFD are compared with the experiment and further analyses are carried out numerically, to investigate the change in the flow around the GV using different GV hydrofoils. Finally, some of these hydrofoils are compared with the reference hydrofoil experimentally.

4.1 Design of the rig

The experimental setup consisted of one guide vane cascade representing the flow in the wicket gate of a low specific speed Francis turbine (0.086 with the equation defined by IEC guidelines). The guide vane inside the rig is the real scale test specimen made suitable for PIV measurements. Jhimruk Hydroelectric Center (4.1x3 MW) in Nepal is chosen as the reference turbine, having 24 guide vanes. The flow channel was enclosed with adjacent guide vane sides, so that the angular position of the rig covers 1/12th of the total angular positions of the turbine. This simplified and reduced model of the rig was designed based on hydraulic optimization through CFD, such that the flow inside the rig matches with the flow around one guide vane of the real turbine [4].

The preliminary design procedure of the rig is shown in Figure 4.1. It shows the guide vane ring of the turbine located with origin at the center of the turbine. The dimensions are shown in meters, such that the inlet diameter of the runner is 0.89 meters. For the construction of one GV cascade rig, three GVs are considered such that the total passage of the rig is extended from pressure side of the first GV to suction side of the third GV. To maintain the swirl component of the flow, upstream and downstream walls of the GVs are designed using free vortex theory. In the real turbine, the same theory is used to design the stay vanes, so that its effect on the flow is minimum.The inlet of the rig is

a straight cylindrical pipe, unlike the turbine, which contains spiral casing to develop some rotational component before entering the GV. In this rig, the spiral casing is replaced with the curves shown as black dashed lines in Figure 4.1. These curves were optimized using CFD, such that the flow field around GVs is similar to that in real turbines [4]. The inlet and outlet of the rig is a cylindrical pipe of diameter 400 mm and 200 mm respectively, which connects to the test rig through diffuser. The final model of the rig was shown in Figure 3.14. The rig was made suitable for PIV measurement by using Plexy glass plates around the passage, such that the laser sheet can pass through the flow.

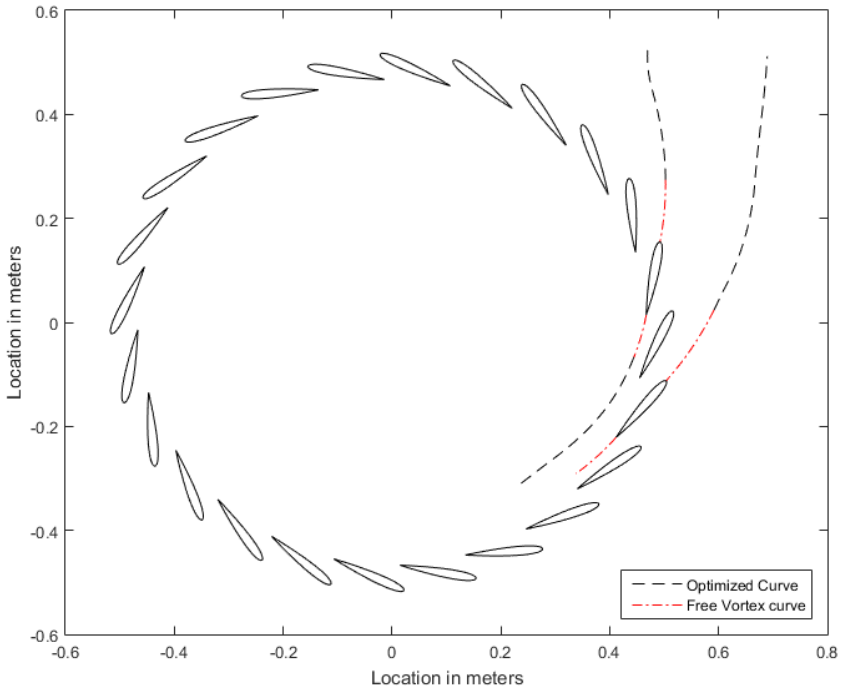

Figure 4.1: Design of one GV cascade rig

4.2 Experimental setup

4.2.1 Layout of the measurement

The test setup was assembled inside a closed loop of the lab. The layout of the entire measurement is shown in Figure 4.2. This loop contains a pump, which was used to deliver a maximum flow of 155.5 litres/sec. This flow corresponds to around 80% of the BEP operating condition for the real turbine. A maximum pressure of 750 kPa was developed inside the pressure tank, using an air compressor. A flowmeter was mounted on the outlet pipe of the test rig, whereas two pressure taps were fixed at inlet of the rig and outlet of the GV to maintain the correct operating point of measurements. The outlet absolute pressure was maintained between 200 kPa to 250 kPa to avoid cavitation inside the system.

However, at low rpm of the pump, the seeding of the particles for PIV was done in the smallest region of the rig by maintaining a negative pressure in that region.

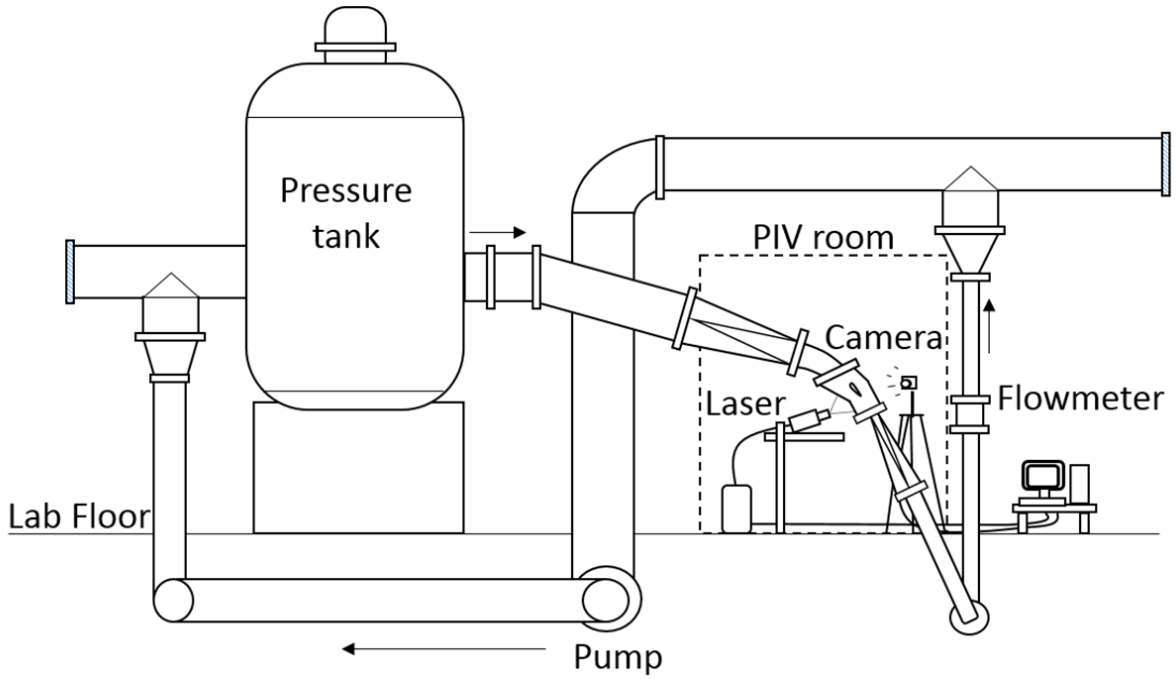

Figure 4.2: Layout of the measurement

4.2.2 Pressure measurement

The back cover plate was fitted with fourteen piezo-resistive pressure sensors around the guide vane surface. These sensors were distributed around the guide vane symmetrically, with 2 mm offset from the guide vane surface. This arrangement is shown in Figure 4.3. For the pressure measurement, an average of 2000 samples were taken for each pressure point at 5 HZ.

4.2.3 PIV setup

The actual PIV measurement was done inside the PIV room, indicated in Figure 4.2 and shown in Figure 4.4 using Dantec System. A light plane was generated from two double cavity Nd-YAG lasers, which provides 120 mJ by pulse. This plane was visualized as paired images by a HiSense 2M CCD PIV camera. Fluorescent seeding particles with a density of 1.016 kg/m^3 and mean diameter of 55 μm were used. These particles were inserted into the rig from the low pressure seeding point, as indicated in the figure. The paired image was acquired at 70 μs, such that the particle movement was between 3-6 pixels depending upon the high and low velocity regions in the frame. The PIV system was calibrated using a 2D calibration target in the planes of measurement. The particle density inside each interrogation area was maintained between 8-15.

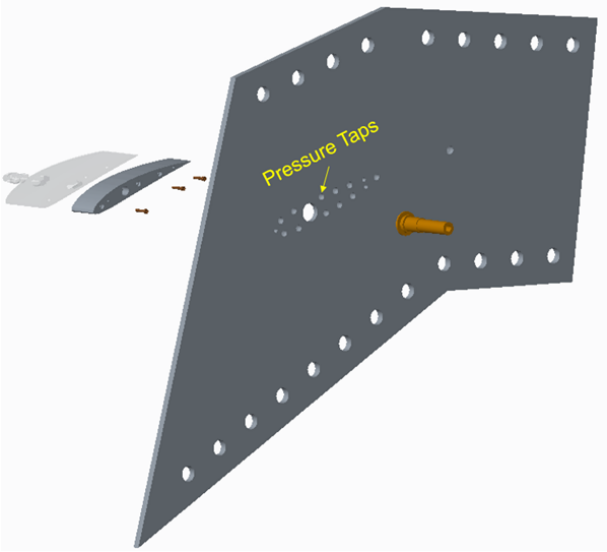

Figure 4.3: Pressure measurement in one GV rig

As shown in Figure 4.5, the total span length of the guide vane was divided into two sections: i) Plexy glass section (P1), which allows the laser sheet to pass over the guide vane and ii) Metal section (P2), which is needed to withstand the water pressure. The total length of the GV span was 97 mm, out of which P1 was 60 mm and P2 was 37 mm for the case without any clearance. Whereas the Plexy glass had a fixed length, the length of the metal section differed, depending upon the size of the clearance gaps being incorporated. Figure shows positions of two parallel laser planes, L1 and L2. L1 represents the plane inside the clearance gap and L2 represents the plane inside the guide vane span. The guide vane was mounted on a Plexy surface from one side, where the image was captured and on a metal cover plate from another side, where the pressure taps are fitted.

The GV inside the rig contains a clearance gap of 2 mm height on one end. Although this study uses a 2D PIV technique, the velocity fields were obtained in the direction of the GV span by measuring velocities at several spans of the GV. For the clearance gap of 2 mm height, this study measured the velocities in 6 planes inside the clearance gap and 19 planes beyond the gap up-to the GV mid-span. Figure 4.6 shows the bottom view of the GV and various planes of measurement. The 'Number' in the figure indicates the number of planes, where the measurements were taken, whereas 'Length(mm)' indicates distance of the planes with respect to the wall. The thickness of the laser sheet was maintained below 1 mm for all the planes. For the laser planes which are less than 1 mm apart, the center of the total thickness of the sheet was considered as the measuring plane.

The particles' flow inside the rig was captured using a CCD camera with a resolution of 1280x1024 pixels and the pixel size of 7.4 μm. The distance between the camera and the front cover plate of the rig was maintained at 1.6 meters throughout the experiment. The processing of the obtained images were done using 32-pixel resolution cross-correlation technique with 50% overlap. This is equivalent to a physical size of 4.7 x 4.7 mm per interrogation space. Velocity vectors were obtained inside the un-masked area of the rectangular field, which contained 1100 vector points for the area of 0.026 m^2 of the flow channel. These vector points are shown in Figure 4.7. The erroneous vectors in each image was maintained below 10% of the total vector points. It was seen that a sufficient amount of image

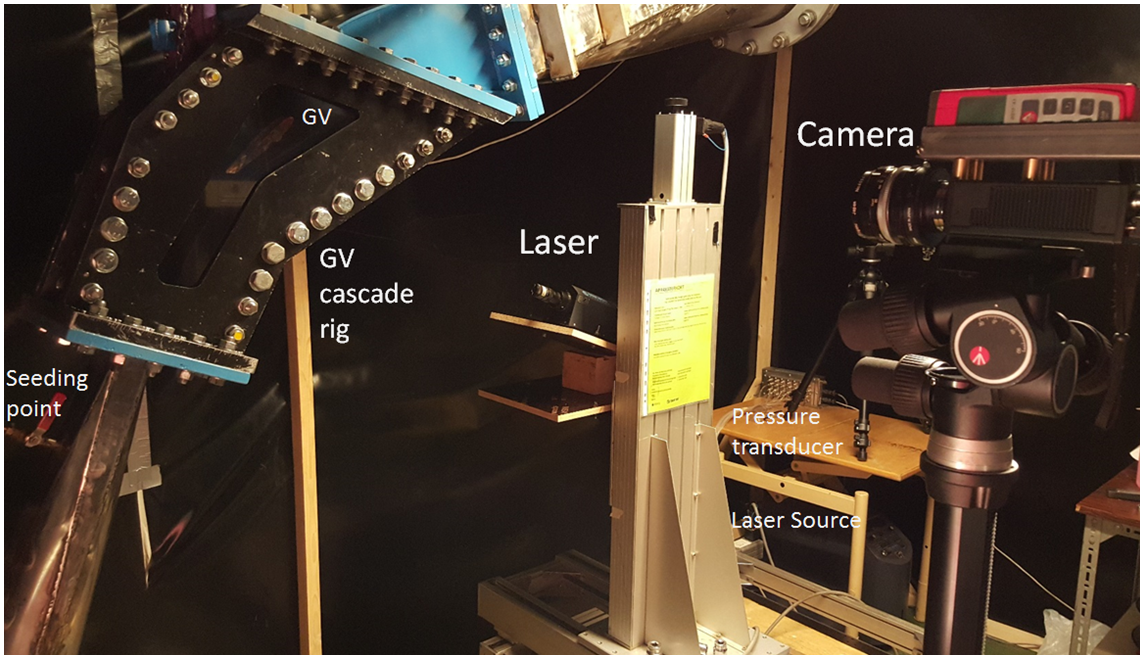

Figure 4.4: Pressure measurement

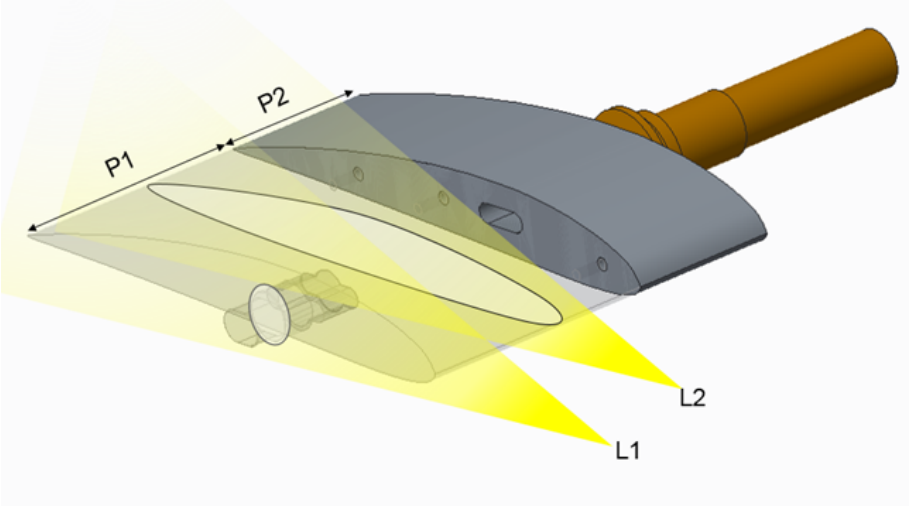

Figure 4.5: Description of the GV test specimen

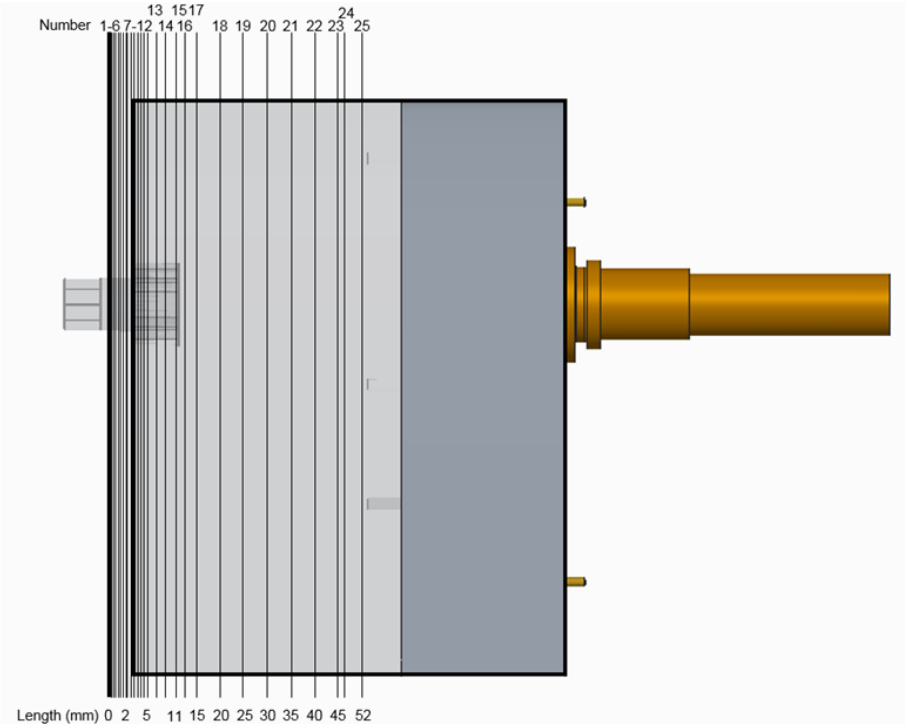

Figure 4.6: PIV measurement planes

pairs can be averaged to compensate the instantaneous erroneous vectors for steady state solutions. In this study, an average of 250 vector pairs were taken, without changing the operating conditions for measurement. The synchronization between the laser and the camera was done using Dantec DynamicStudio 3.40 PIV processor. Figure 4.7 also shows the circumferential locations corresponding to GV outlet (GVout) to runner inlet (Rin) of the real turbine. The area between these two curves represents the vaneless space between GV and runner.

4.3 Numerical model

The fluid domain is extended from the conduit outside the pressure tank flange to the first bend after the guide vane outlet. The diameter of the inlet pipe is 400 mm and the chord length of the guide vane is 142.77 mm. The entire domain, shown in Figure 4.8 is composed of around 13 million hexahedral cells generated with ICEM. O-grid technique was used at inlet and outlet round channels. The near-wall regions of the domain was refined to resolve high gradients. Similarly, the mesh density was higher in the regions of wakes and separations. With the same pressure and flow conditions as carried out in the experiment, the y+ value around the guide vane was 9.3 in average. For the clearance gap of 2 mm, 50 elements were used with finer distribution near wall boundaries.

The mass flow rate at the inlet of the test rig at the designed condition is 195.83 kg/s. This value corresponds to two guide vane passages. For experimental validation of CFD, the flow rate corresponding to the experiment, i.e. 155.5 kg/s was chosen. This case is referred as the reference

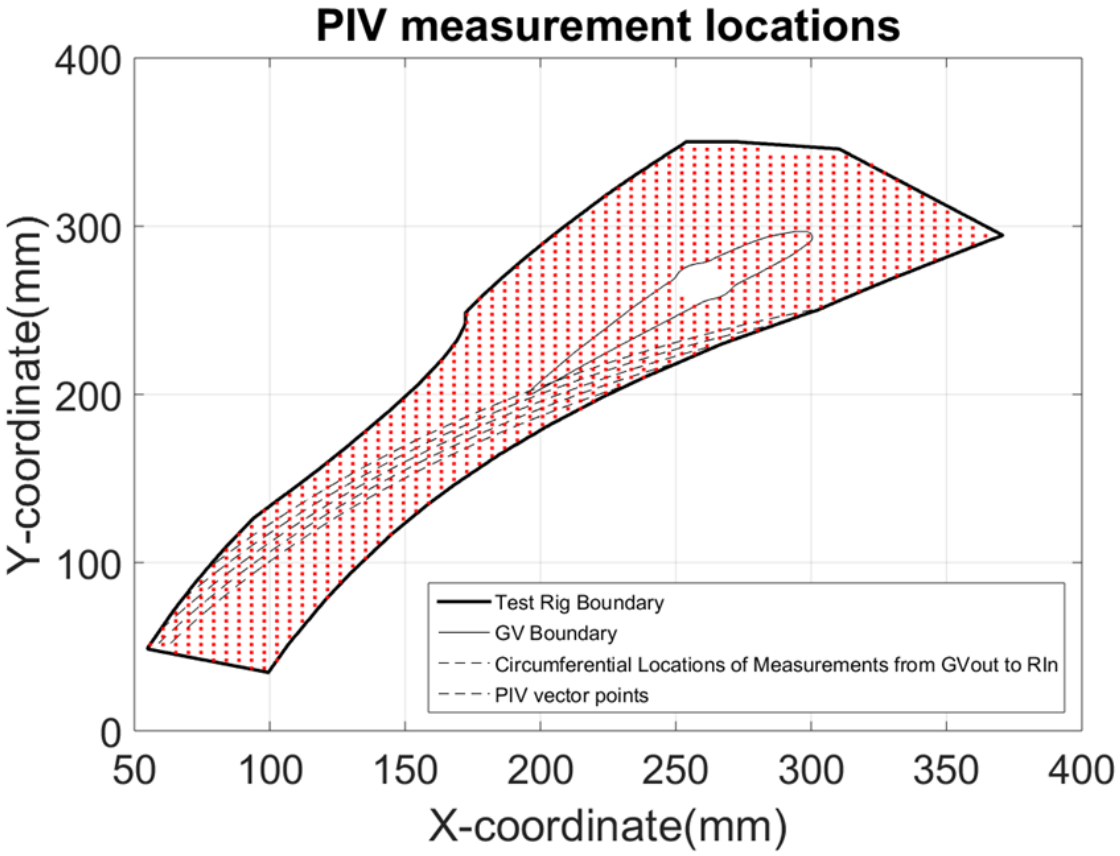

Figure 4.7: Position of vectors and circumferential location corresponding to the real turbine

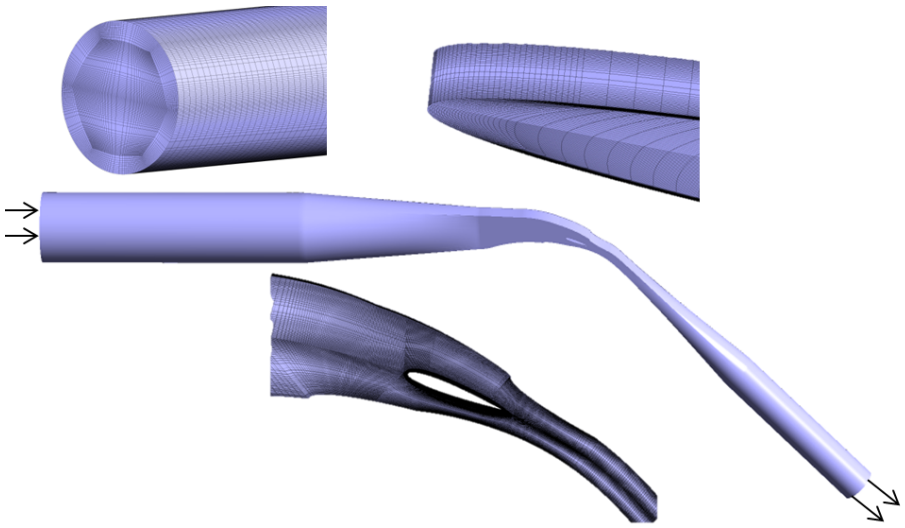

Figure 4.8: Domain for CFD and mesh

case in this paper. In the reference case, the guide vane has NACA0012 profile in both CFD and experiment. The validated reference model is used to compare 4 hydrofoils at the designed condition. A static pressure of 900 kPa was specified at the outlet. The blade and the pipes were defined as non-slip smooth walls. At the inlet, a turbulence intensity of 5% was used.

The estimation of the discretization error and extrapolation values were done by using the GCI method [23]. This technique is found to be effective in predicting the numerical uncertainties for the case of Francis turbines [63]. The general formula for estimating the errors were shown in Equations 2.25, 2.26 and 2.27. Three different mesh sizes corresponding to the mesh count of 0.22M, 1.52M and 12.83M were used in the independence test. The mesh refinement was done by increasing the distribution in each direction, i.e. the grid refinement factor (r) by 2X. The tangential velocity (C_u) at the mid-point of GVout and Rin, corresponding to Figure 4.7 were chosen as the monitored variable. These values obtained by the three mesh densities are noted as C_{u1}, C_{u2} and C_{u3}, where C_{u1} represents the fine mesh and C_{u3} represents the coarse mesh. The approximate and extrapolated relative errors were calculated using the GCI method, from Equations 2.25, 2.26 and 2.27 (replacing ϕ with C_u).

Table 4.1 shows the uncertainties and extrapolated values at the two locations. The numerical uncertainties in the tangential velocity at the mid-point of the runner inlet was calculated to be 3.6% and 4.0% for the medium and fine grid densities respectively. At the mid-point of the guide vane outlet, the uncertainties were 14.21% and 7.7% respectively. This is the position where the flow is distorted due to boundary wake from the guide vane.

Figure 4.9 shows the tangential velocity at 30 circumferential locations corresponding to the GVout and Rin curve shown in Figure 4.7 respectively for three mesh densities. These figures also show the discretization error bars computed using Equation 2.27 for the fine mesh. For the fine mesh at GVout, the uncertainty ranges from 0.03% to 7.7%, which is equal to $\pm$0.01 m/s and $\pm$1.55 m/s

Table 4.1: Discretization error in one GV rig

Parameter	GVout	Rin
r_{21}	2.03	2.03
r_{32}	1.87	1.87
C_{u1}(m/s)	20.12	33.96
C_{u2}(m/s)	21.41	33.85
C_{u3}(m/s)	23.55	33.76
C^{21}_{uext}(m/s)	18.87	34.07
e^{21}_{a}	0.0641	0.0033
e^{21}_{ext}	0.0660	0.0032
GCI^{21}_{fine}	0.0774	0.0036
GCI^{32}_{med}	0.1421	0.0040

respectively. The maximum uncertainty is near the trailing edge, where the effect of the wake is prominent. For the fine mesh at Rin, the uncertainty ranges from 0.0021% to 12.2%, which is equal to $\pm$0.0006 m/s and $\pm$2.60 m/s respectively. The maximum uncertainty is found to be near wall boundaries, where the velocity gradient is highest.

4.4 Results and Discussions

4.4.1 Comparison between CFD and experiment

The first half of this section contains the validation of the numerical model for the reference case. To make the comparison easier, the static pressure at the outlet in CFD was adjusted such that the pressure at the stagnation point was same between CFD and the measurement. The pressure comparison was done based on the normalized pressure (C_p), which is the ratio of the pressure at a point to the pressure at inlet. The value of (C_p) takes into account the distribution of the pressure along the stream. Figure 4.10 shows (C_p) distribution around GV from leading edge (LE) to trailing edge (TE). In the x-axis, another dimensionless term x/c is used, which represents the position (x) from LE with respect to the chord length (c). The figure also shows the location of the pressure taps with reference to GV in both CFD and PIV. The maximum pressure was found at LE, where stagnation occurs. The distribution of pressure around GV measured in the experiment matched with the CFD result. In the pressure side (PS), the average deviation between experiment and CFD was calculated to be 0.6%. In the suction side (SS), this deviation was 3.3%. It can be noticed from this difference between the two deviations that the pressure in the SS is not as stable as the PS due to fluctuations in this region during the measurement because of unaccounted clearances from wall roughness and manufacturing tolerances.

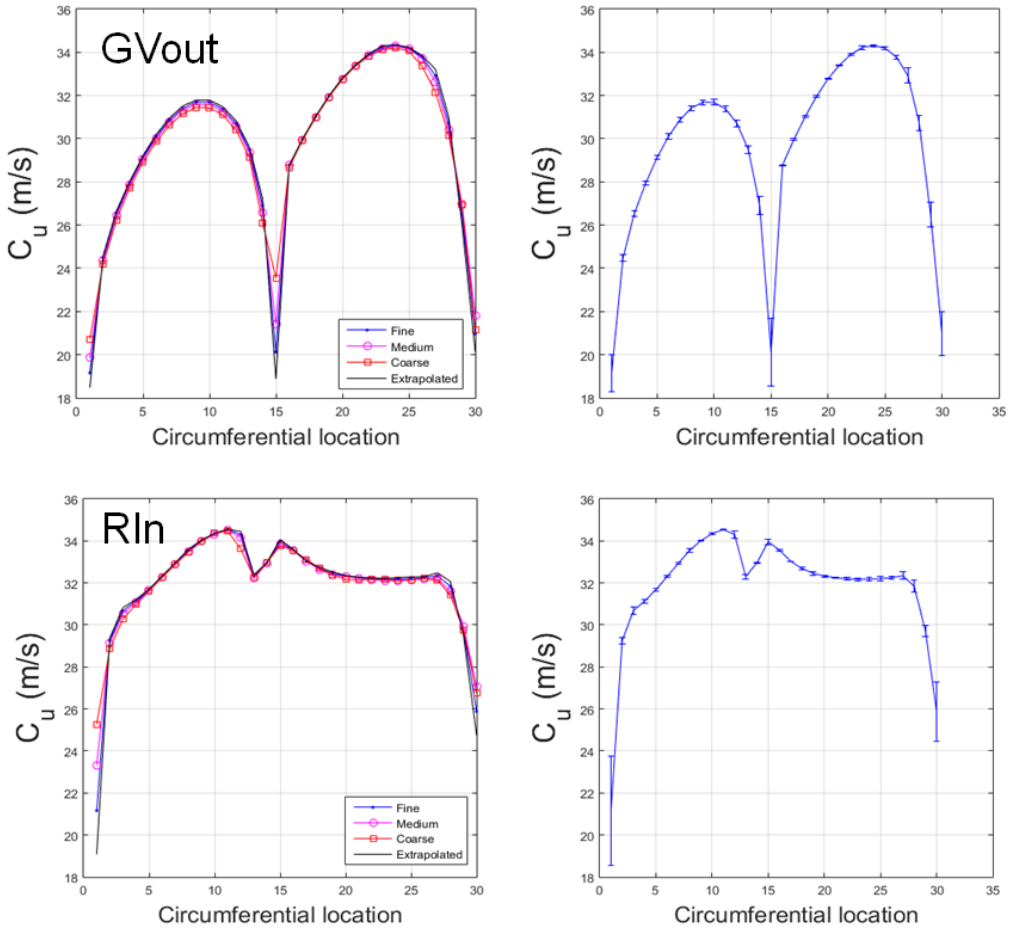

Figure 4.9: Discretization error

The velocities measured by PIV and CFD at the circumferential locations of GV outlet (GVout) and Runner Inlet (Rin), shown in Figure 4.7, were compared. Figure 4.11 and Figure 4.12 shows the average velocities at GVout and Rin for mid-span. The curve starts from PS (upper) wall and ends at the SS (lower) wall. In each curve, there are 29 points located at equidistant positions. At mid-span, PIV and CFD follows the same velocity profile trend. As discussed above, PIV shows the dissipation of the wake before passing into the runner. At GVo, the mean of the average velocity was found to be 29.94 m/s in PIV, whereas this value was 30.45 m/s in CFD. The deviation was 1.67%. The deviation calculated at each of the 29 points was 4.7% in average, with maximum at the region of the wake. At Rin, the mean of the average velocity was found to be 32.97 m/s in PIV, whereas this value was 33.14 m/s in CFD. The deviation of the mean of the average velocity at Rin between CFD and PIV was 0.5%, whereas the deviation of individual point was 1.57% in average. The lower values of the velocity in PIV was due to the losses from the wall roughness, which were not accounted for the CFD analysis.

The flow field obtained by PIV was post-processed using 32-pixel resolution cross-correlation technique with 50% overlap. Velocity vectors were obtained inside the un-masked area of the rect-

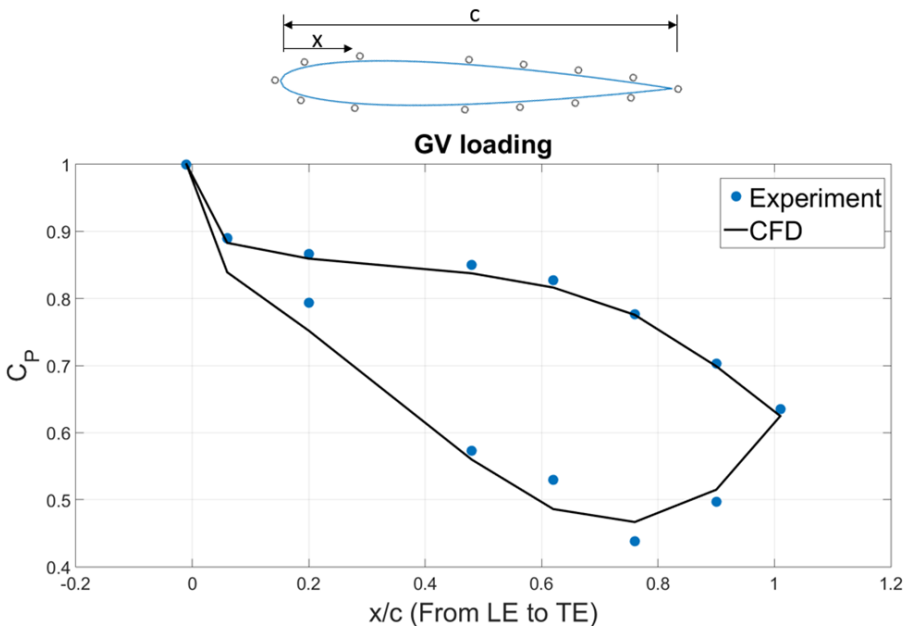

Figure 4.10: Pressure distribution around GV

angular field, which were time-averaged for 100 images at 4 Hz. There were around 1100 approved vector points for each plane inside the PIV boundary shown in Figure 4.7. The velocity field on the whole plane was interpolated based on these approved vectors, to create the velocity contours. The velocity field obtained on these points are represented in Figure 4.13 in the form of contour for GV mid-span. The figure also shows the velocity contour obtained in CFD in the same region. The velocity field predicted by the two method is found to be comparable, as both the pictures represent same color-map. The stagnation point at LE, 'C' profile of the velocity around TE, velocity field around GV and downstream velocities were accurately predicted by the two methods. However, the PIV contour were affected by some factors. An abrupt change in velocity can be seen near the upper corner due to shadows from the bent of LE. It can be observed that the wake from TE travels downstream inside the runner in CFD, but dissipates before the runner in PIV. Some potential reasons for the faster dissipation of wakes in PIV are: i) the vectors were calculated in the interrogation space of 32x32-pixel size in PIV, corresponding to a physical size of 4.7 x 4.7 mm, which was not enough for capturing wakes. In CFD, the boundary mesh refinements make it possible to capture the velocity gradients within smaller width ii) statistics involved in averaging the images in PIV tend to cancel out instantaneous odd vectors. Whereas averaging provides better estimation of the flow in steady regions, the unsteady secondary flow regions could have undergone the average-out procedure iii) the frequency of the paired image was around 14 Hz, which was not comparable to the high frequency wake phenomena. These results give some important conclusions about the limitation of the current PIV.

Figure 4.14 shows the velocity contour inside the clearance gap for both CFD and PIV. The leakage flow is related to the GV loading discussed in Figure 4.10. Towards LE, the flow inside the GV follows the mainstream flow because the pressure difference in this region is less compared to the region around TE, where the flow is diverted into the suction side. The shaft area in PIV is masked out, but the effect is seen downstream, where the velocity is reduced due to circulations. The accelerated flow near the TE can be observed in both the cases. However, the pattern in PIV is more irregular due to

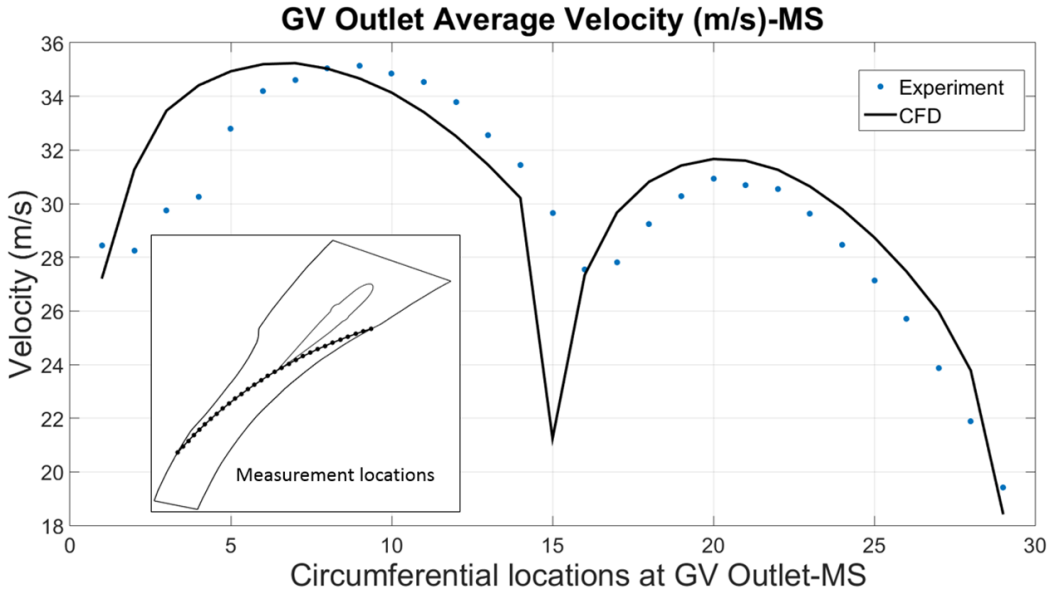

Figure 4.11: Average velocity at guide vane outlet

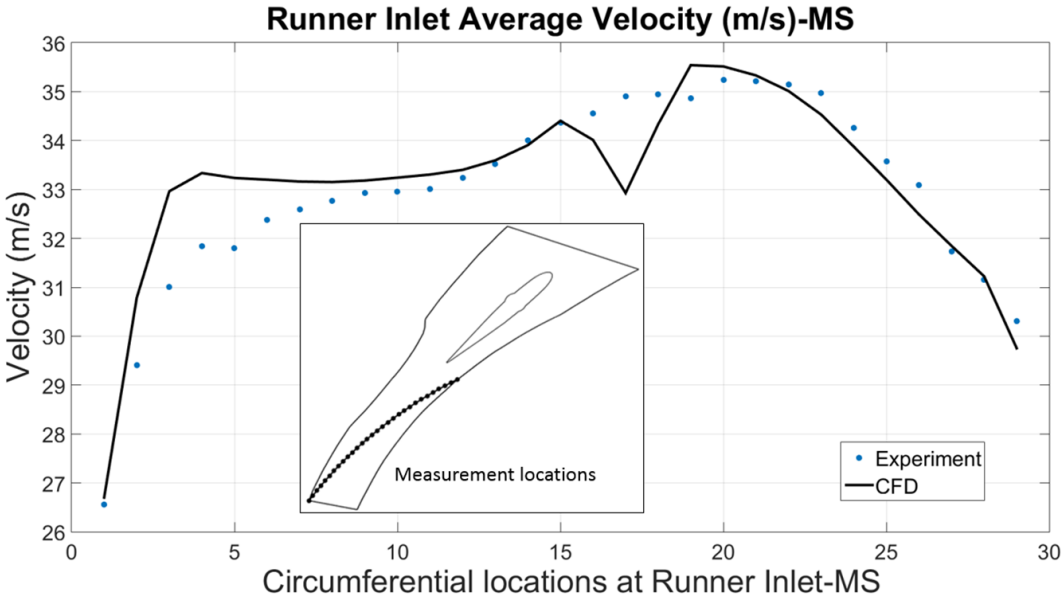

Figure 4.12: Average velocity at runner inlet

the effect from the wall. The fluctuations could have also happened due to induced cavitation inside the low-pressure clearance zone.

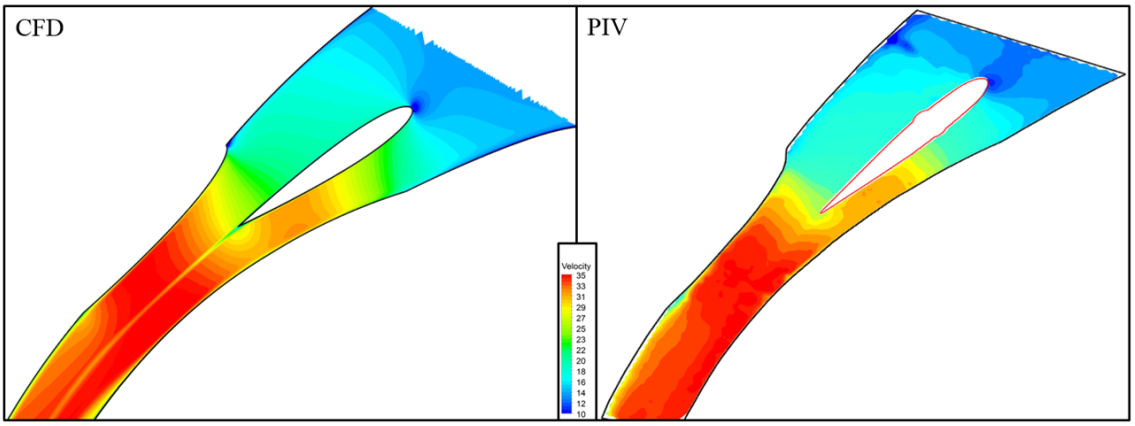

Figure 4.13: Velocity contour at midspan

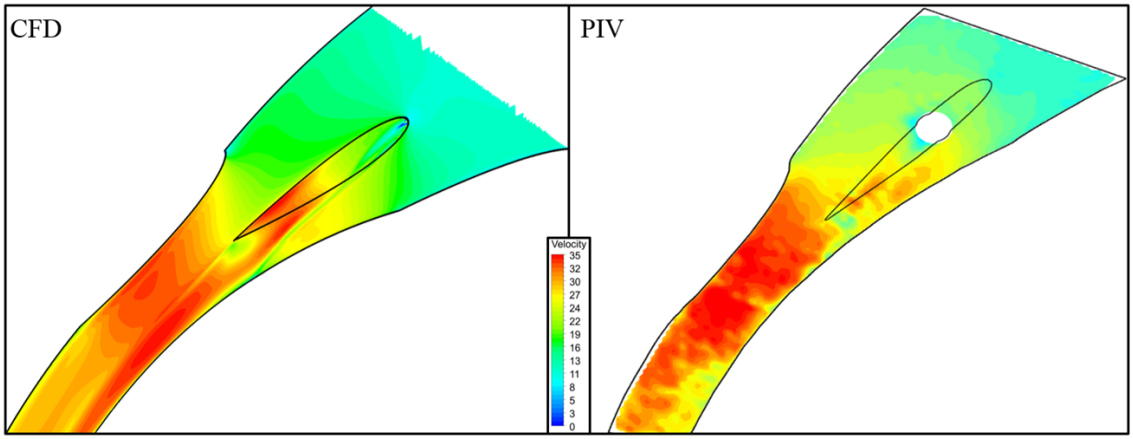

Figure 4.14: Velocity contour at the clearance gap

The leakage flow shown in Figure 4.14 mixes with the SS flow and forms a vortex passage, which has the tendency to shift towards mid-span, while travelling downstream. Figure 4.15 illustrates shifting of the passage vortex in CFD compared to the picture of the rig taken while PIV was being conducted. The intensity of this vortex was found to be gradually dissipating. The streamlines show that the leakage flow is occurring after the mid-chord position of the GV. The comparison of the vortex between CFD and the experiment is also shown in Figure 4.16. The water stream from pressure side mixes with the main flow in suction side, forming the vortex filament. When these vortices strike the runner blades, it could have a negative effect on the performances of the runner. The shifting of the vortex away from the wall can also be explained from Magnus effect, which in this case, is the force induced on the rotating fluid in a direction at an angle to the axis of spin. The rotation of the flow in the suction side due to the leakage of the flow from the pressure side is explained in Figure 4.17.

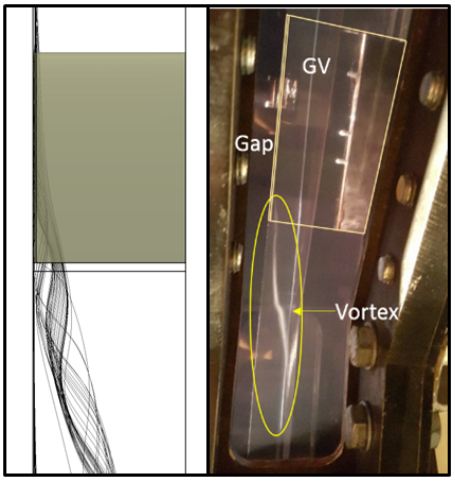

Figure 4.15: Vortex from the clearance gap (bottom view)

Figure 4.16: Vortex from the clearance gap (side view)

4.4.2 Comparison of GV profiles - CFD

Figure 4.18 shows the velocity component normal to the chord length (Vy), as defined in Figure 4.22 from LE to TE of all hydrofoils. In the case of 0012, the Vy component gradually grows from LE and after mid-stream position of the chord, the growth rate increases. At 75% of the chord, the Vy component is maximum. After 75%, Vy decreases with the same rate and becomes minimum at TE again. This trend of Vy was found in all the hydrofoils. In the case of 4412, negative values of Vy was observed until mid-stream position. After mid-stream, the values were positive, but less than other profiles. The negative value shows that the flow is directed from SS to PS, which is the result from the negative pressure difference between PS and SS. The Leakage flow factor (L_{ff}) calculated according to Equation 7 for all the hydrofoils are shown in Table 4.2. The reference velocity, Vo in the equation was taken as the average velocity at the outlet of the stay vane. The table shows that L_{ff} is maximum in 0012. Compared to the minimum L_{ff}, which was measured in 4412, the L_{ff} in 0012 is 4.45 times greater.

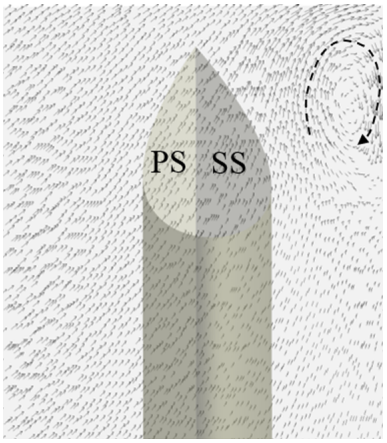

Figure 4.17: Rotation of the flow

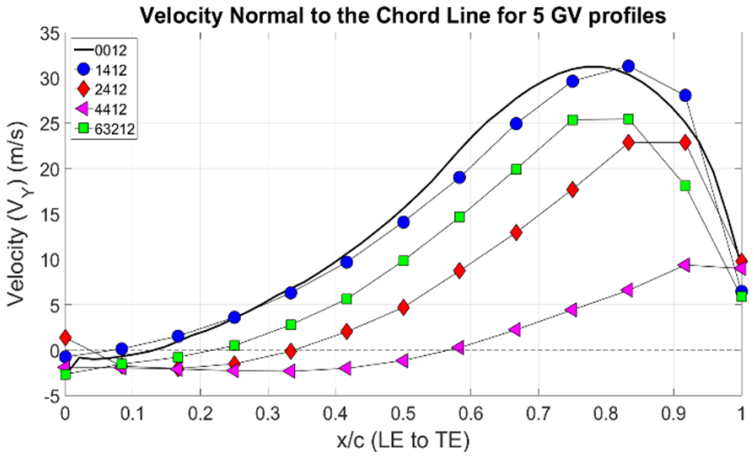

Figure 4.18: Comparison of GV profiles using CFD

It was seen that L_{ff} affected the SS flow travelling downstream. For easy comparison, the leakage flow shown in Figure 4.15 was categorized into four sections. This category is shown in Figure 4.19. The first category (i) is the flow in between the guide vanes close to the SS inside the clearance plane. This type of flow is not contributing to the leakage flow directly, but mixes with them to form the passage vortex. The leakage flow with high velocity traveling from PS strikes the SS flow and induces a pressure difference between the two flows. This difference in pressure results in the formation of a passage vortex, which travels downstream in the form of a vortex filament. In the case of 4412, the SS flow is not disturbed by the PS flow. The second category (ii) represents the flow entering the clearance gap from the position just upstream of GV. In the case of 0012, this type of flow enters the LE and after around 30% of the chord length, moves away from the clearance gap and leaks through the SS. In 4412, the flow moves into SS, but since the velocity gradient is not prominent, this behavior can be regarded as the effect of hydrofoil geometry. The third category (iii) is the flow in the PS end that flows into the gap due to the pressure difference between the two sides of the GV in the clearance gap plane. In 0012, the velocity gradient is higher than 4412 and it can be inferred from Figure 4.14 that this category of the flow has the highest influence on the leakage flow. The fourth category (iv) is the region in PS below the clearance gap plane. This flow is entrained by the high-pressure gradient along the span, which makes it move into the clearance gap plane. Higher the leakage flow due to ii)

Table 4.2: Leakage flow factor for different NACA profiles

NACA Profiles	0012	1412	2412	4412	63212
L_{ff}	0.815	0.788	0.464	0.183	0.577

and iii), higher is the pressure gradient along the span and higher is the effect of iv). Hence, in 4412, the effect is nullified due to reduced impact of other categories of flow.

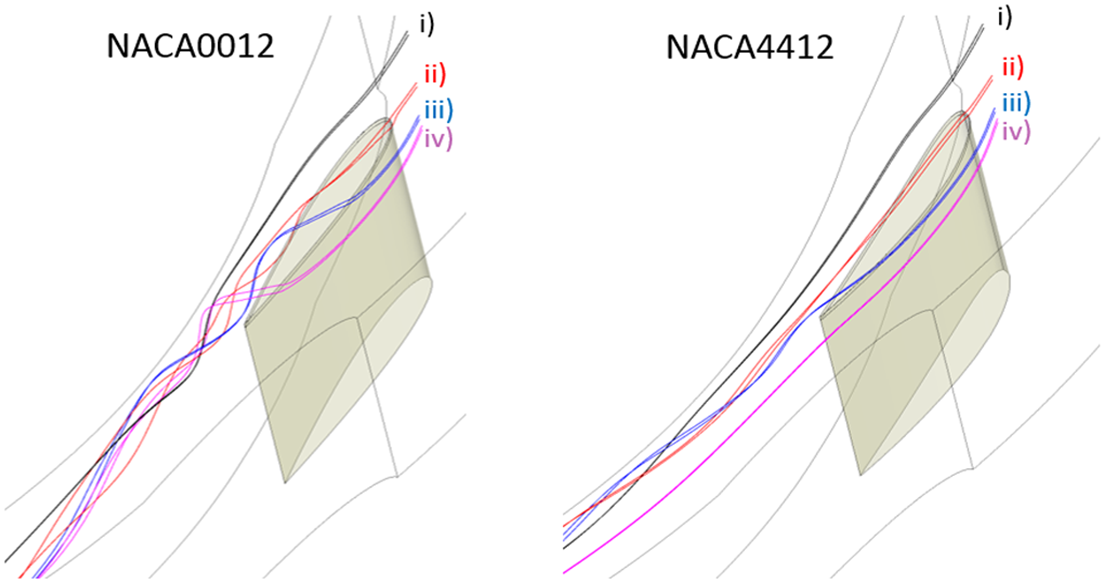

Figure 4.19: Comparison of the vortices through clearance gap

4.4.3 Comparison of GV profiles - Experiment

The pressure distribution around the guide vanes with two cambered hydrofoils are shown in Figure 4.20. The placement of these sensors were shown in Figure 4.3. In the plot, the values in the X-axis represent chord-wise position starting from leading edge (LE) to trailing edge (TE) of the guide vane (GV). The values in the Y-axis represent absolute pressure normalized by the pressure at LE. The closed curve is formed due to the difference in pressure between the two sides of the GV. The area enclosed by these two curves is responsible for generating a net force in the direction of the resultant force, i.e. from pressure side (PS) to suction side (SS). This force is also referred as blade or GV loading. The pressure distribution around the two hydrofoils shown in the figure shows that the resultant force produced in NACA4412 is less than in NACA2412. This difference in the GV loading has a consequent effect on the flow through clearance gap. These effects are shown further in the results of PIV measurement.

Figure 4.21 shows contour plots of the average velocity at two span positions of the guide vane for

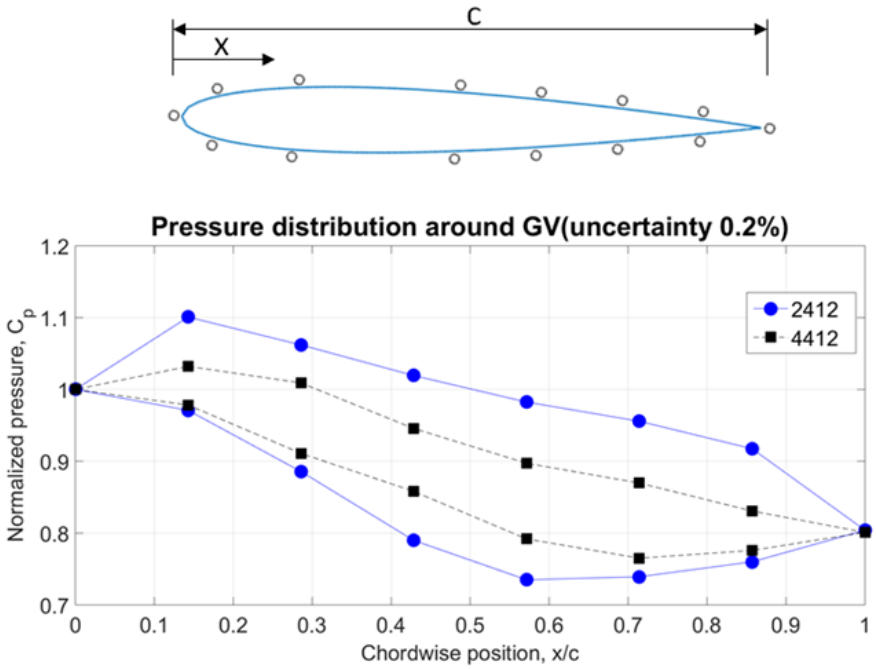

Figure 4.20: Pressure distribution around GV obtained from experiment

three GV profiles. The cambered profiles NACA2412 and NACA4412 is compared with the symmetric profile NACA0012. The flow at mid-span plane in all the profiles is found to have similar pattern. At some positions, the results are affected due to the shadow of the geometrical edges and curvatures. The velocity distribution around the guide vane indicates the effect of changing the hydrofoil profiles on the flow phenomena. In NACA4412, the velocity gradient in the adjacent pressure and suction side is reduced, compared to that in NACA2412 and NACA0012 profiles. The consequence of this difference in velocity distribution is not significantly seen in the mid-span plane. However, the effect is noticeable in a plane inside the clearance gap. The difference in pressure between two sides of the guide vane drives the leakage flow inside the clearance gap, at an angle relative to the GV chord. In NACA0012 and NACA2412, the leakage flow is seen from PS to SS inside the clearance gap. This flow affects the primary flow in the SS forming a vortex filament traveling downstream. In NACA4412, due to smaller pressure difference between PS and SS, the leakage flow is less diverted from the GV chord. The vortex filament mixes with the wake from GV boundary while traveling downstream.

It was also seen from the visual inspection that changing the GV profiles have a direct consequence on the types and intensity of the vortex filaments produced. Although the cavitation inside the setup was controlled, the high intensity vortex in NACA0012 resulted in localized cavitation flows, disturbing the PIV measurement inside the clearance plane. These disturbances can be observed in the PIV result, shown in Figure 4.21.

The amount of leakage flow from the clearance gap was quantified in terms of velocity component normal to the guide vane's chord. The velocity component in the direction of the chord line is considered as the ideal condition. Under the action of the pressure difference between the two sides

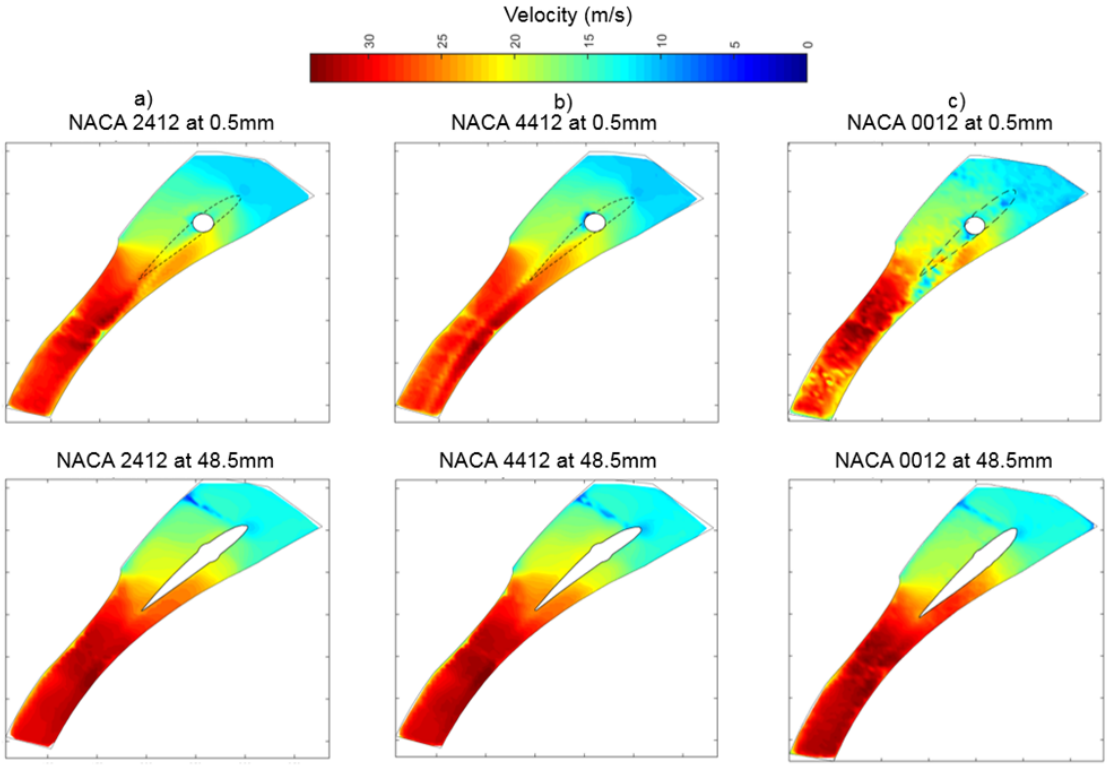

Figure 4.21: Contours obtained from PIV

of GV, the velocity vector makes an angle with the chord line. This vector was resolved into two components: Vx, which is in the direction of the chord line and Vy, which is perpendicular to the chord line. The component Vy represents the leakage flow inside the gap at 1 mm from wall, which is plotted against the GV chord in Figure 4.22. In this figure, the horizontal line at Vy = 0 represents the ideal flow. From LE to TE, 100 points were sampled at uniform distance. The position of the shaft has been indicated in the graph. In front of this area, the Vy component is close to ideal but negative. The negative Vy is justified by the stagnation point as shown in Figure 4.21, which is in the lower side of LE. Downstream of shaft area, the Vy component differs according to the hydrofoil shapes. The Vy was found to be maximum in the case of NACA0012, whereas it is reduced in NACA2412. In NACA4412, the negative Vy after the shaft area indicates that the flow is driven from lower to upper side of the GV. This diversion is also seen in Figure 4.21 towards the upper end of GV TE inside the clearance plane.

The leakage flow through the clearance gap mixes with the main flow towards the suction side. This results in a rotational velocity component that forms a vortex filament. The nature of this vortex depends upon the types of hydrofoil and consequent pressure difference between the GV sides. To study about the characteristics of these vortices, several planes were observed perpendicular to the GV chord after TE. These planes are shown in Figure 4.23 with the average velocity contour at their respective locations. The X-axis of this graph shows the positions normal of chord from top to bottom of the rig, which are at equidistant location. The Y-axis of the graph shows the distance in mm from the wall. These locations were also shown in Figure 4.6. The first 2 mm of this axis indicates the clearance gap, whereas the mid-span is at 48.5 mm. The vertical velocity deficit area

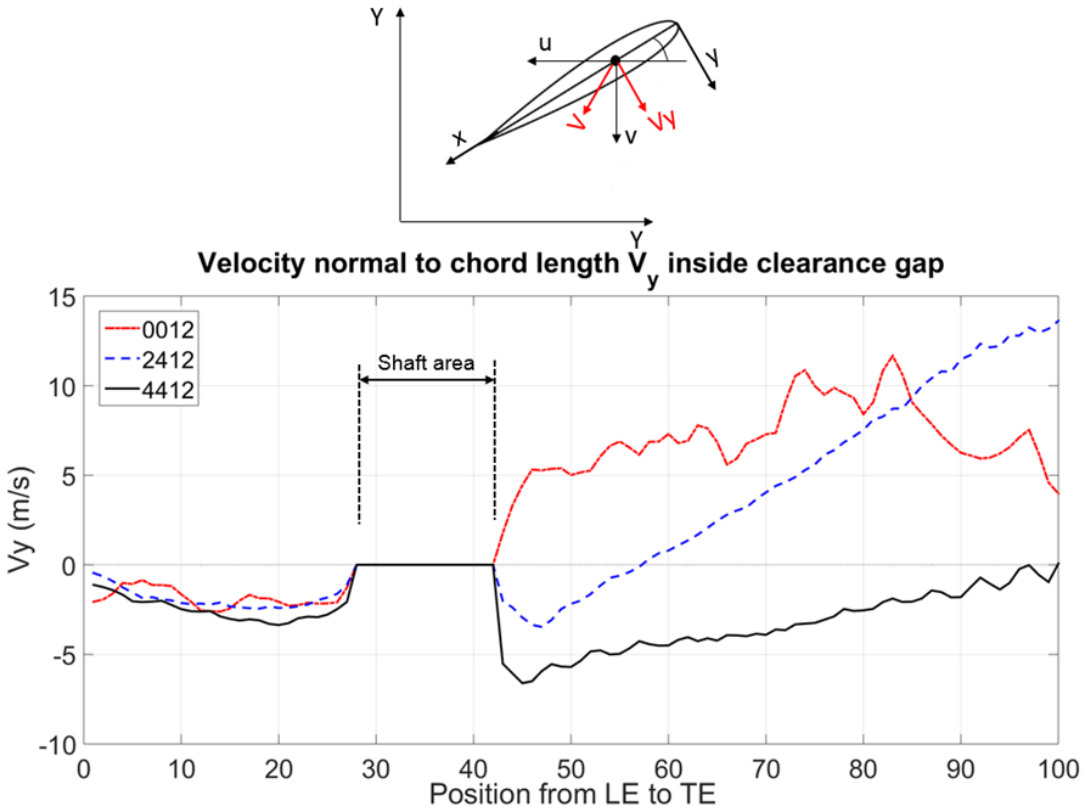

Figure 4.22: Pressure distribution around GV obtained from experiment

in all the figures towards X = 60 indicates the wake region due to GV TE. In this figure, the planes at a distance of 0 mm, 4 mm and 10 mm from the GV TE are shown. The upper 3 plots are from NACA2412 and the bottom 3 are from NACA4412. The velocity at the plane 10 mm from TE shows higher passage velocity than the upstream regions, because of the narrower passage area. Circular low velocity contours can be observed in all the cases at the location near the TE in the clearance end. These concentric circles represent the position of the vortex as it travels downstream from GV. It has to be noted that although the plots are showing the average velocity, the average is only determined by taking the velocities in circumferential and meridional directions. The plots have not taken into account the velocity component in the radial direction. Incorporating the radial or rotational component in the average velocity might increase the values of these circular contours. However, it is possible to infer the location of these vortices and how they travel and dissipate, while travelling downstream. The movement of the vortex filament is according to the GV loading in both the cases. It can be seen that in NACA2412, the vortex shifts from left to right, towards the suction side away from TE as traveling downstream. The intensity of this contour is observed to be gradually dissipating. In NACA4412, the vortex remains closer to the TE and is slightly deviating in opposite direction at some locations. However, the intensity of the vortex is observed to be dissipating as well.

Whereas the rotational component in the vortex is responsible for material wear in runner inlet, the deviation of the flow in the circumferential and meridional direction is responsible for incorrect stagnation angle. Due to deviation of the flow from clearance gap to the suction side, the angle of incidence with which the runner was designed is also deviated, especially near the clearance gap re-

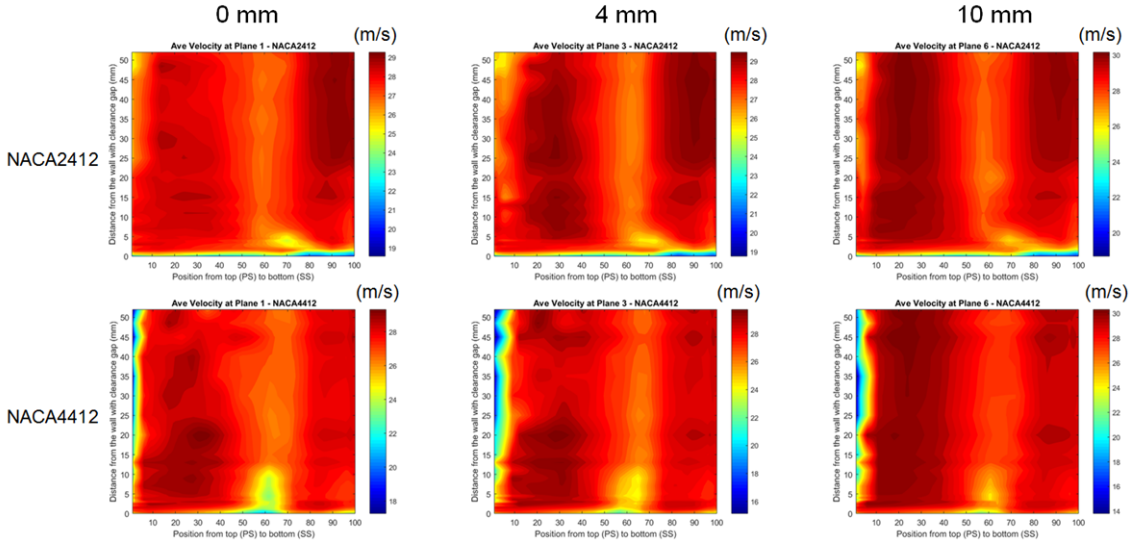

Figure 4.23: Pressure distribution around GV obtained from experiment

gion. A plane was made at the locations of GV outlet and Runner inlet, which was shown Figure 4.7 throughout the measuring plane. This plane is shown in Figure 4.24, with the contour plot of the angle between the meridional and circumferential velocity components (α). The Y-axis of this plot is equivalent to that in Figure 4.23, whereas the X-axis represents the circumferential locations corresponding to the GVout and RIn, as shown in Figure 4.7 starting from bottom to top. In NACA2412, the α angle increases near the clearance gap region in TE. This increase in the angle indicates that the meridional component of the velocity increases, resulting in the incorrect stagnation point at the inlet of runner connecting hub and shroud. The incorrect stagnation angle has a consequent effect on the efficiency loss of the turbine and material wear of the runner inlet. In NACA4412, although the vortex filament is observed from Figure 4.23, the deviation in the angle is not as predominant as in NACA2412. However, the angle is reduced, which infers that the flow develops more circumferential component. This can be explained from Figure 4.22, where the deviation of the flow was seen in the opposite direction. Runner of the Francis turbines are designed for a certain inlet angle α, which gives the velocity triangle for a given flow. The non-uniform inlet angle distorts the velocity triangle near the clearance gap region. When the runner is hit by such non-uniform flow angle, a local separation of the flow occurs near the regions of hub and shroud. This separation causes the turbulence losses and wear of the material due to sediment and cavitation erosion. It has to be noted that the current test rig only contains the stationary components of the turbine. Since the runner was not installed, the effect of rotor-stator interaction on the flow pattern has not been included. In the presence of runner, the frequency of vortices from the leakage flow needs to be taken into account for the stability aspects of the turbine.

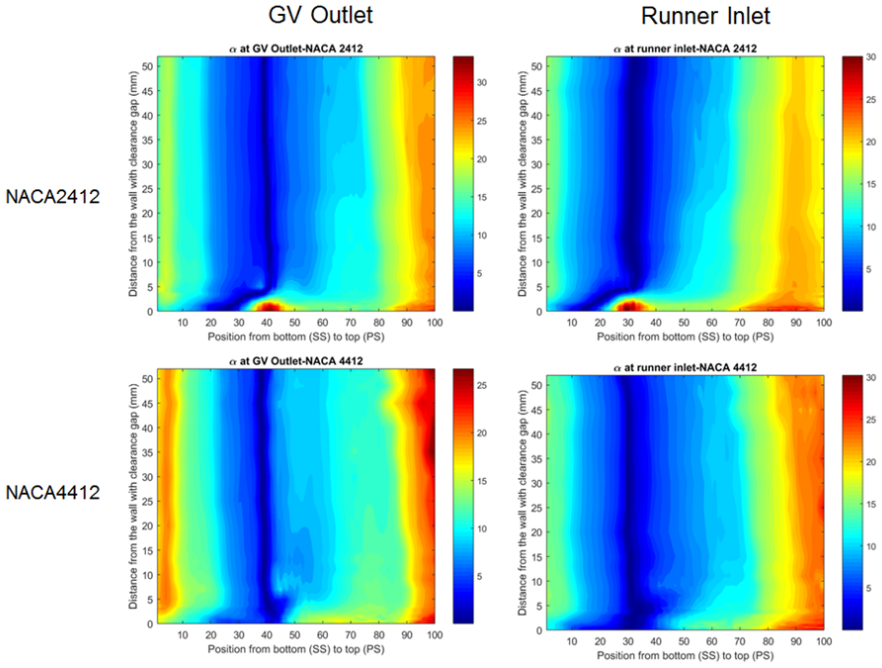

Figure 4.24: Pressure distribution around GV obtained from experiment

4.5 Summary of the study in one GV rig

This chapter focused on the study of the leakage flow through clearance gap of GV in one GV cascade rig. A reference model, containing NACA0012 hydrofoil shaped GV with 2 mm clearance gap was used to validate the numerical result with experiments. The normalized pressure (C_p) distribution around the GV showed the average deviation of 0.6% on the pressure side and 3.3% on the suction side between CFD and experiment. At mid-span, the velocity contour of CFD and PIV showed a good agreement in the leading edge, pressure and suction side and the 'C' profile around the trailing edge. The mean of the average velocity at GVout in mid-span was found to be 29.94 m/s in PIV and 30.45 m/s in CFD. The mean of the average velocity at Rin in mid-span was found to be 32.97 m/s in PIV and 33.14 m/s in CFD. Some discrepancies were seen in the clearance gap plane because of the wall effect. The acceleration of the flow from PS to SS in the clearance gap region was observed in both CFD and PIV, which contributed to the formation of a vortex filament.

The validated numerical model was used to do the in-depth study of the leakage flow and compare the performances between five GV hydrofoils. The streamlines contributing to the leakage flow was divided into four categories depending upon their positions at the inlet of GV. These streamlines form a vortex filament, which has the tendency to move away from the wall, while travelling downstream. A dimensionless term, 'Leakage Flow Factor' (L_{ff}) was used to compare the potential leakage flow through the clearance gap of five hydrofoils, including the reference case. Compared to the L_{ff} of 0.815 in the reference case, NACA4412 showed the reduction by 4.45 times. The value of L_{ff} is directly related to the pressure difference between the two sides of GV.

The two GV profiles, NACA2412 and NACA4412 were also tested using PIV and pressure mea-

surements. It was illustrated that symmetrical guide vanes have a negative impact on the turbine's performances, due to high pressure difference between PS and SS. The difference is reduced for hydrofoils having flatter SS. The minimization of this gradient influences the velocity field. Leakage flows downstream of GV shaft are observed for all the cases. In NACA0012 and NACA2412, positive leakage flow was observed, which distorts the main flow in the suction side forming a vortex filament. This vortex has a tendency to shift away from the wall while traveling downstream due to the rotational velocity component. In NACA4412, some negative leakage flow was observed due to small pressure difference. The vortex in this case has a tendency to remain attached to the wall due to the rotational component in opposite direction. It was seen from the contour plot of α angle that a sharp increase in the runner inlet angle occurs near the clearance region for NACA2412. Change in the stagnation angle compared to the designed parameters might aggravate the erosion and turbulence losses in the turbines due to the separation in the LE of runner.

These results were shown for designed GV opening angles. In one GV cascade rig, it was not possible to test the flow in off-designed conditions. The results in various opening angles are discussed in next chapters.

Chapter 5

Three GV Cascade Rig

Previous chapter showed some limitations of one GV rig. One of the major limitations was the interference of the walls surrounding the GV and its effect on the flow. By upgrading the one GV rig to three GV rig, this limitation of one GV rig could be overcomed for the middle GV. This results in the closer estimation of the flow around GV compared to real turbines. In addition, the measurements can be performed for various GV opening angles instead of only designed conditions.

The design principles of three GV cascade rig is similar to that of one GV rig. In this case, instead of one GV, three GVs were taken to model the complete rig. The preliminary design of the cascade rig is shown in Figure 5.1. Similar to the one GV rig, the main passage of the rig contains free vortex and optimized curve. In the case, the total angular position covered by the passage is $1/6^{th}$ of the circular ring. This chapter presents the CFD technique to measure the velocity field around GVs including clearance gap for two GV profiles and seven opening angles. The results of the CFD is compared with the solutions obtained from one GV rig.

5.1 Numerical model

The complete CFD domain for three GV cascade is shown in Figure 5.2. The guide vanes were modelled with 2 mm clearance gap on one end. The mass flow rate at inlet corresponds to four GV passages, which is equal to 391.67 kg/s. At outlet, pressure needed to avoid the negative pressure in the narrowest region of the rig was defined. The inlet diameter of the pipe is 400 mm, whereas the chord length of each guide vane is 142.77 mm.

The meshing was done using ICEM. O-grid was used at cylindrical inlet and outlet boundaries. Near the GV, the mesh was refined to resolve high gradients. The entire domain consisted of around 4.5 million hexahedral mesh elements. The clearance gap of 2mm consisted of 80 elements.

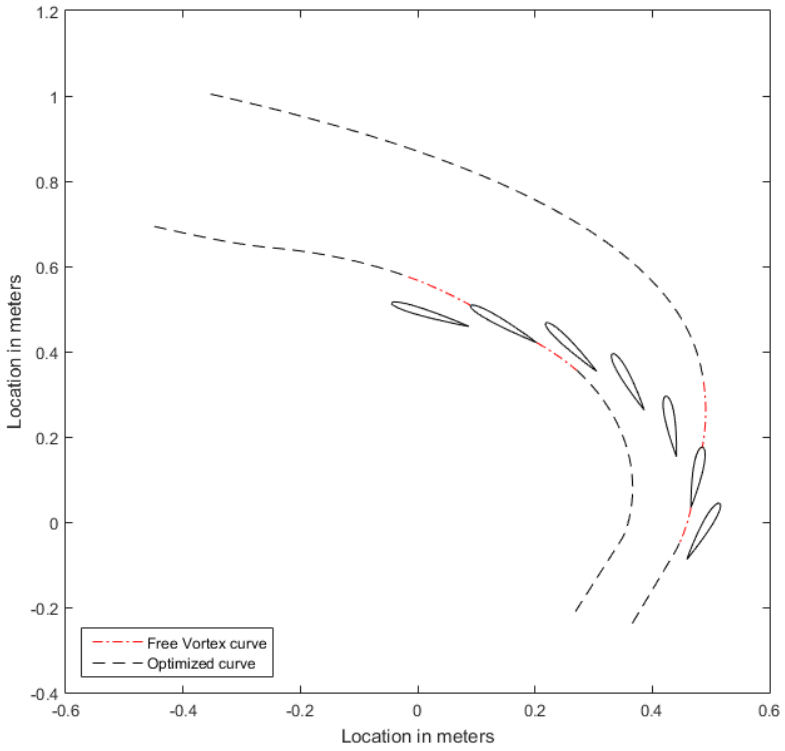

Figure 5.1: Design of three GV cascade rig

The estimation of the discretization error was done using GCI method [5] for 0° GV opening. In this method, the domain needs to be discretized with three different sizes of the mesh, with uniform increment. In this case, the grid refinement factor (r) was chosen to be 1.5×. Figure 5.3 shows the locations in the rig, where the parameters were measured. In the figure, the curve, SVout and GVout represent the circumferential position corresponding to stay vane outlet and guide vane outlet respectively.

Table 6.1 shows the significant parameters that were measured for the mesh sensitivity study. In the table, r_{21} is the exact value of the grid refinement factor between fine and medium mesh, whereas r_{32} is that between medium and coarse mesh. ϕ represents the variable measured, which in this case is a component of the velocity. The subscript, 'ext' is the extrapolated value of the variable based on the three solutions. GCI is the numerical uncertainty values for different sizes of the mesh. In this case, Point 1 has the minimum uncertainty, because in this region, the unsteadiness in the flow is less, compared to Point 2 and Point 3.

Figure 5.4 shows average velocity in the GVout curve for different sizes of the mesh. The velocity deficit regions apart from the wall represent wake from each GV's trailing edges. The figure shows that the uncertainty in the result is high near wall regions. In other regions, the uncertainty was found to be within 2%.

Figure 5.2: 3 GV CFD model

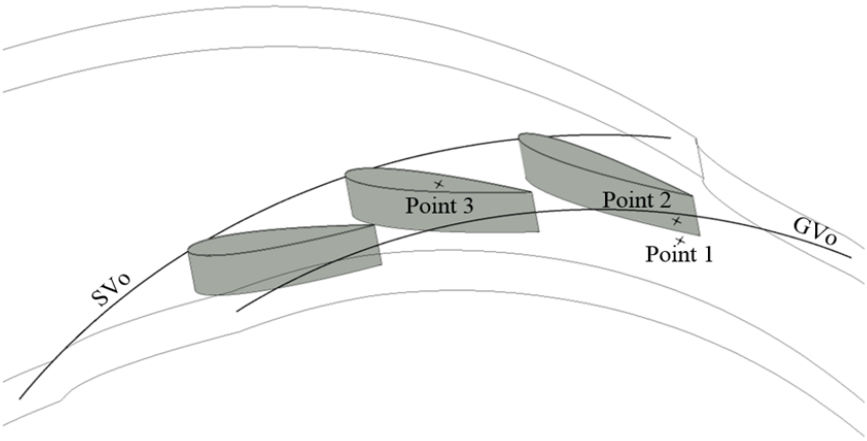

Figure 5.3: Points and curves for mesh convergence study

5.2 Results and Discussions

The results are discussed in four sections. In the first part, the result of three GV cascade rig is compared with CFD and PIV done in one GV rig. It is to observe how closely the three results match with each other. In the second part, pressure along the GV stream (leading to trailing edge) is measured and compared between NACA0012 and NACA4412 at the midspan profile. The consequent vortices are then compared in terms of leakage flow factor and vortex travel. Finally, the torque at various chord-wise positions of the two profiles at all opening angles were compared.

5.2.1 Comparison between one and three GV rig

In this study, the comparison is done by taking the velocity contours at the mid-span plane for all the cases. Figure 5.5 shows the contour plot. The distribution of velocity in the test rig for all the cases are similar, specially around the leading edge, where the stagnation occurs, trailing edge profiles and pressure and suction side flows. The discussion about the comparision between CFD and PIV in one

Table 5.1: Discretization error in three GV rig

	Parameter	Point 1	Point 2	Point 3
Velocity u(m/s)	r_{21}	1.55	1.55	1.55
	r_{32}	1.7	1.7	1.7
	$\phi_{coarse(3)}$	5.82	-19.78	-14.6
	$\phi_{medium(2)}$	5.73	-18.74	-16.16
	$\phi_{fine(1)}$	5.77	-19.29	-17.4
	ϕ_{ext}	5.84	-20.28	-19.65
	GCI^{21}_{fine}	0.0158	0.0648	0.1619
	GCI^{32}_{med}	0.0279	0.0987	0.1717

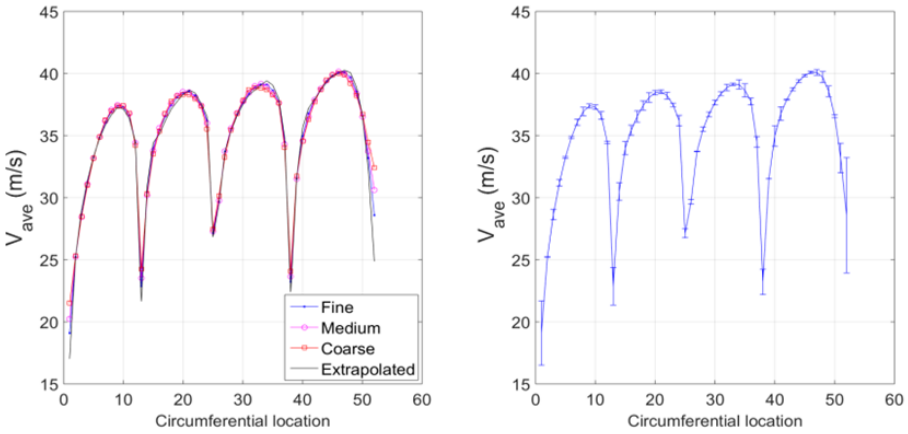

Figure 5.4: Average velocity along GVo curve

GV rig was presented in the previous chapter. In three GV rig, the contours are more periodic between adjacent GVs, which is closer to the real turbine. Due to the smaller cross section downstream of GVs in three GV rig, compared to the inlet mass flow rate, the maximum velocity in three GV is bigger than one GV rig.

5.2.2 GV loading

The area integral of the pressure difference between the two adjacent sides of a single GV gives a resultant force acting on the GV. The flow through the leakage gap depends on this resultant force. This GV loading was measured at midspan by measuring the pressure along the GV profile as shown in Figure 5.6. The measured pressure was normalized with the pressure at leading edge, which has been termed as Cp in the GV loading graph. This normalized pressure was plotted against the chord-wise position (x/c) from leading edge to trailing edge. In the plot, the red straight lines indicate the

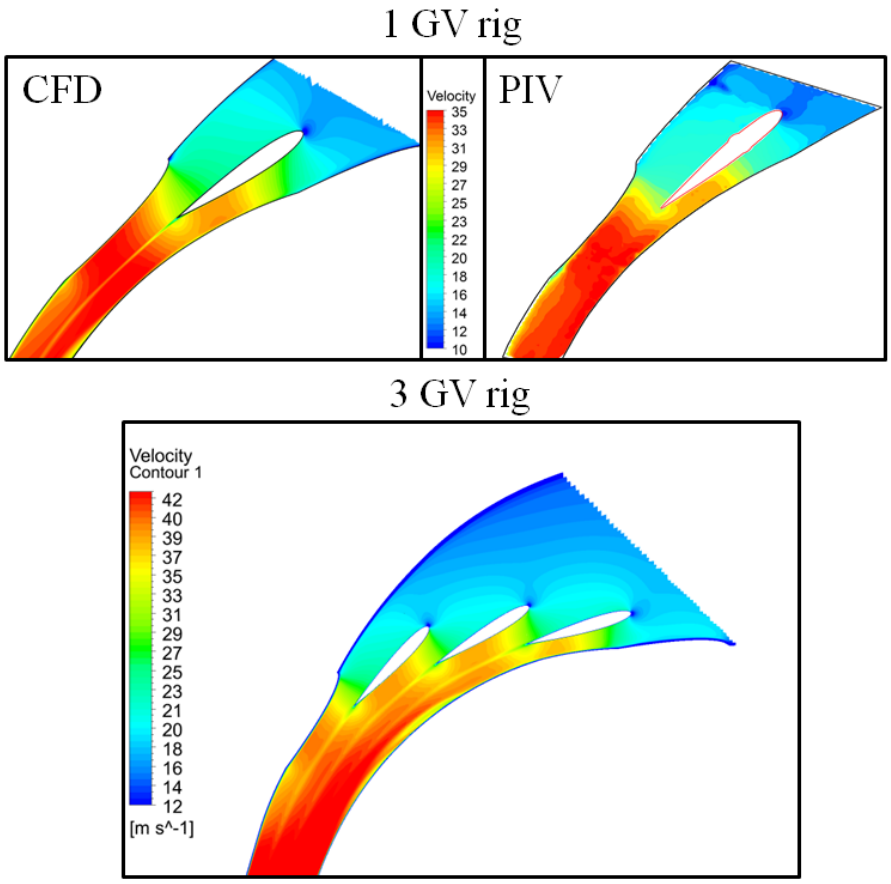

Figure 5.5: Velocity contours at midspan between one and 3 GV rig

pressure in the pressure side whereas the black dotted lines indicate the pressure in the suction side. Figure 5.6 shows that at 0° opening angle with respect to BEP position, the GV loading in NACA0012 profile is higher than in NACA4412. It can also be seen from the graph that towards leading edge (x/c = 0.08), in NACA4412, the suction side pressure drops significantly. This could be because of an incorrect stagnation angle for NACA4412. It means that when a non-cambered profile is replaced with a cambered profile, the stagnation angle for BEP needs to be adjusted accordingly. In the present case, this drop in pressure could lead to some leakage flow at the leading edge for NACA4412 profile. However, it can be inferred that in overall, the leakage flow in NACA4412 is less than in NACA0012 for BEP.

Similarly, the GV loading for all the tested opening angles is shown in Figure 5.7. The negative degree with respect to BEP represents GV closing and positive degree represents GV opening. In hydropower plants, GV closing refers part load and GV opening refers full load operation. It can be seen from the figure that the GV opening reduces the GV loading. In the case of NACA0012, high opening angles makes the pressure difference minimum, which reduces the leakage flow through the clearance gap. The same effect also takes place in the case of NACA4412. However, at some point, the pressure difference becomes zero and at even higher opening angles, the pressure side experiences lower pressure than the original suction side. In such a condition, the leakage flow changes its direction. In the case of real turbines, the consequent vortices from the leakage flow do not enter the

runner, but hit the adjacent GVs. In the case of GV closing, the pressure difference increases for both the profiles. However, this difference is less in NACA4412 than in NACA0012. This infers that in part load conditions, the leakage flow in NACA4412 is less than in NACA0012.

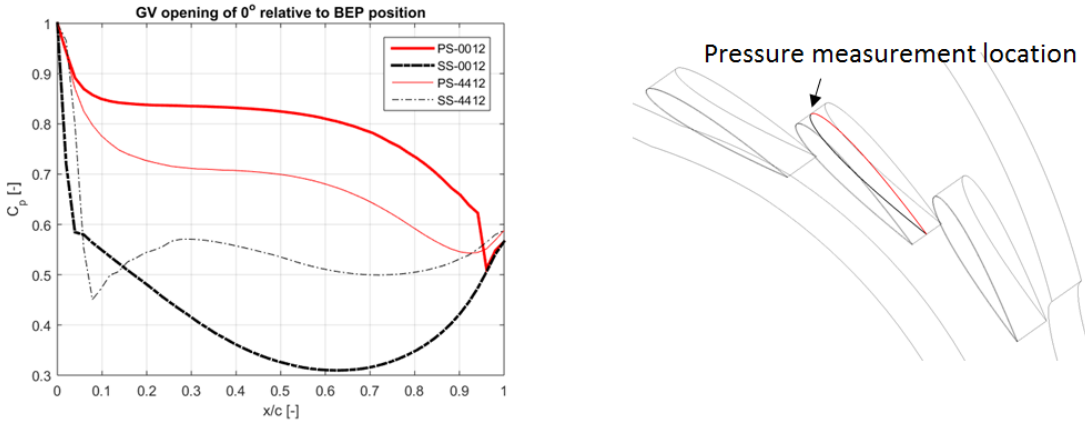

Figure 5.6: Pressure measurement at BEP

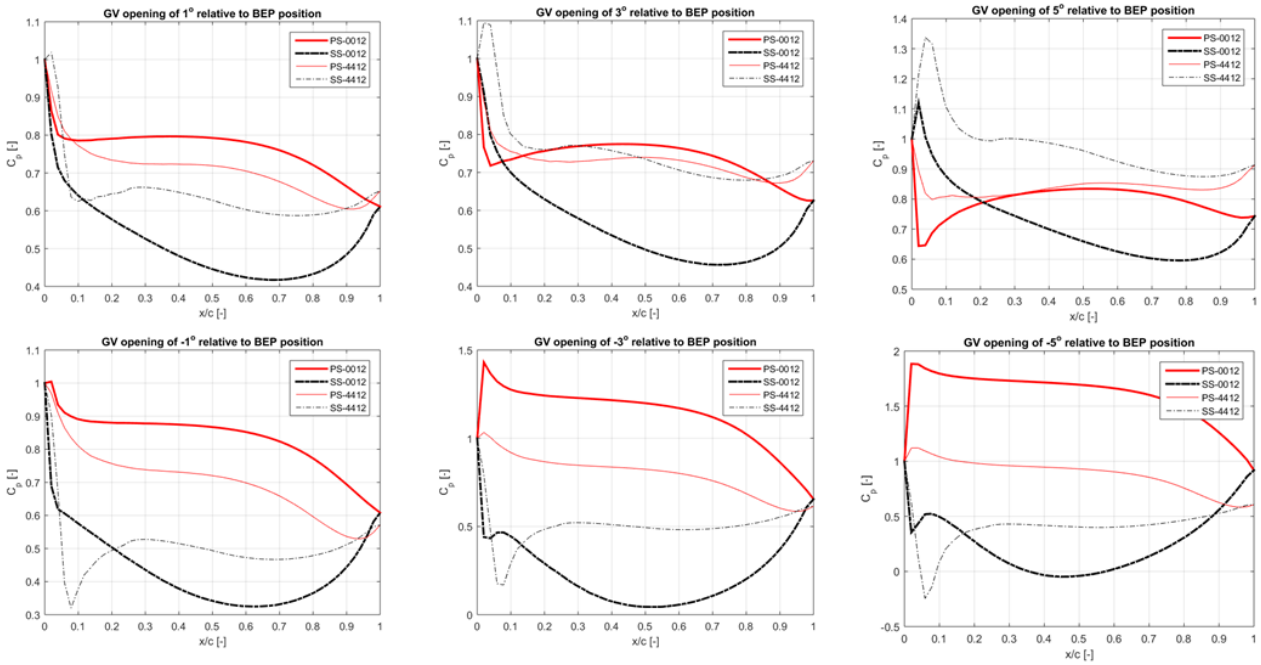

Figure 5.7: GV loading at different opening angles

5.2.3 Vortex filament

When a clearance gap is present at the ends of the GV, the pressure difference between the two sides induces leakage flow from high pressure to low pressure side. When this flow mixes with the main

flow in the suction side, it results in the formation of a vortex, which is driven downstream additing to the total losses in case of turbines. The leakage flow in this study has been quantitatively compared between the two profiles by comparing Vy, which is the velocity component normal to the guide vane chord. In an ideal case, Vy component is zero, which means no leakage flow occurs inside the clearance gap.

Figure 5.8 compares the two profiles at BEP in terms of Vy. In the graph, the Vy component is plotted against the chordwise position of the GV. This figure shows that the Vy component is high after the mid-chord position. This trend is related to the GV loading curve shown in Figure 5.6. Compared to NACA0012, NACA4412 profile shows reduced Vy. The average value of Vy in NACA0012 for BEP is 27.4 m/s whereas in NACA4412, this value is 20.7 m/s. Figure 5.8 also shows the velocity vectors along the chord for the two profiles. It shows that the velocity gradient in the case of NACA0012 is high along the chord line. Figure 11 compares the Vy of the two profiles for $\pm 1°$ and $\pm 3°$. For GV closing, the average value of Vy for NACA0012 for –1° and –3° are 25.7 m/s and 24.1 m/s respectively, whereas these values are 20.7 m/s and 22.7 m/s respectively for NACA4412. It shows that the leakage flow in NACA4412 is less than in NACA0012 for all the GV closing angles. For GV opening, the average value of Vy for NACA0012 for 1° and 3° are 26.6 m/s and 18.62 m/s respectively, whereas these values are 21.6 m/s and -11.2 m/s respectively for NACA4412. The graphs also show that the leakage flow for high GV opening angles is in the negative direction compared to the direction of Vy. The leakage flow leads to the formation of a vortex filament, which is shown

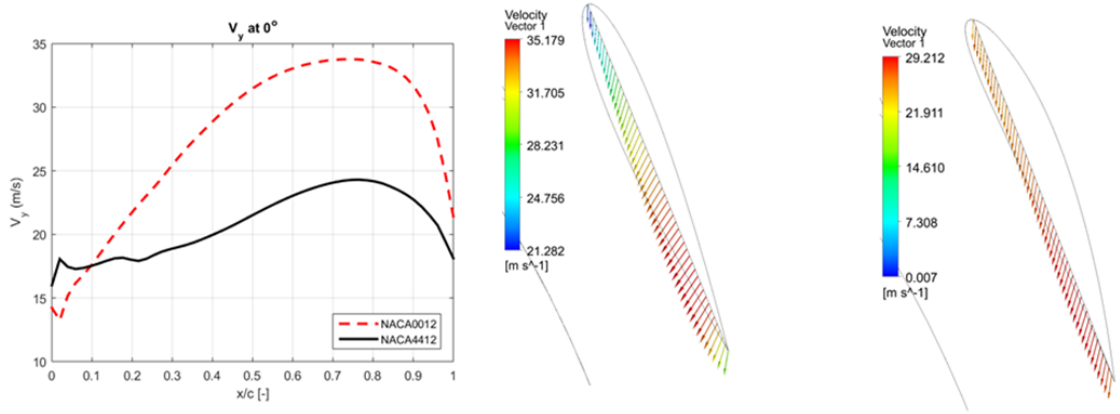

Figure 5.8: Vy component and velocity vectors along the chord line for NACA0012 and NACA4412 at BEP

in Figure 5.10, 5.11 and 5.13. Five planes are defined perpendicular to the chord line of the middle GV, which are at a distance of 20mm. In these planes, contours of total pressure normalized with the total pressure at the inlet is plotted. The value of this normalized pressure (CTP) is between 0 and 1, such that the values below 1 defines losses. The vortex filaments are represented by low CTP values. By observing the adjacent planes, the path of these vortices can be traced. With the same contour value range, it can be seen from 5.10 that the intensity of the vortex in NACA0012 is bigger than in NACA4412. In NACA4412, it can be seen that the vortex originates mostly from the leading edge. This justifies the GV loading curve shown in 5.6, where the difference in pressure towards the leading edge for NACA0012 is high.

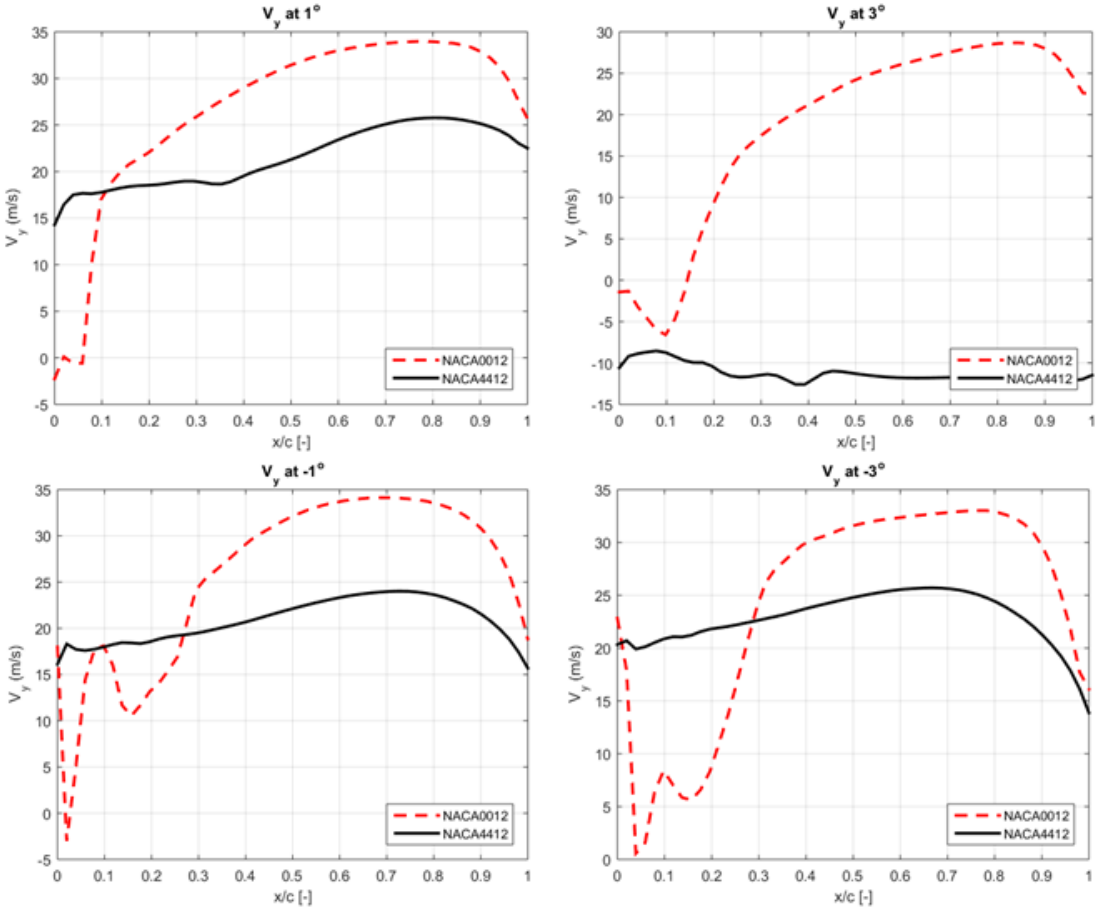

Figure 5.9: Vy component for NACA0012 and NACA4412 for 4 opening angles

Figure 5.11 shows the CTP at –5° opening angle. Due to high pressure difference in the GV at closing conditions, the leakage flow and the consequent intensity of the leakage flow also increases. However, the intensity of the vortex in NACA4412 is smaller than in NACA0012. Figure 5.13 shows the CTP at 5° opening angle. In this case, it can be seen that the intensity of the vortex in NACA4412 is slightly bigger than in NACA0012. It can also be seen that the direction of this vortex in NACA4412 is in the opposite direction compared to other cases. Instead of entering the runner in the case of real turbine, such vortices will hit adjacent GVs and could cause more problems. Nevertheless, the distance between the adjacent GVs is larger than the distance between GVs and runner blades. Larger distance helps to dissipate the vortices and thus, minimize the effect.

From Sections 3.1, 3.2 and 3.3, it can be concluded that the cambered profiles reduces the pressure difference between the adjacent sides of the GV at the designed condition. In a straight flow channel, when the angle of stagnation is 0°, the lift force in any symmetrical profile is zero. However, due to a circumferential orientation of the GV in turbines, a pressure difference is maintained between the adjacent sides at same chord length, even if the stagnation angle is 0° with respect to the chord line. Using asymmetrical profiles with flatter ends facing the runner, the difference in pressure can be reduced. This difference can be reduced for BEP and all GV closing angles. However, in GV opening angles, the difference in pressure gradually decreases for both the profiles. This decrease

in GV loading affects NACA0012 positively, but in the case of NACA4412 at high opening angles, the pressure difference becomes negative. This changes the direction of the leakage flow and the consquent vortices.

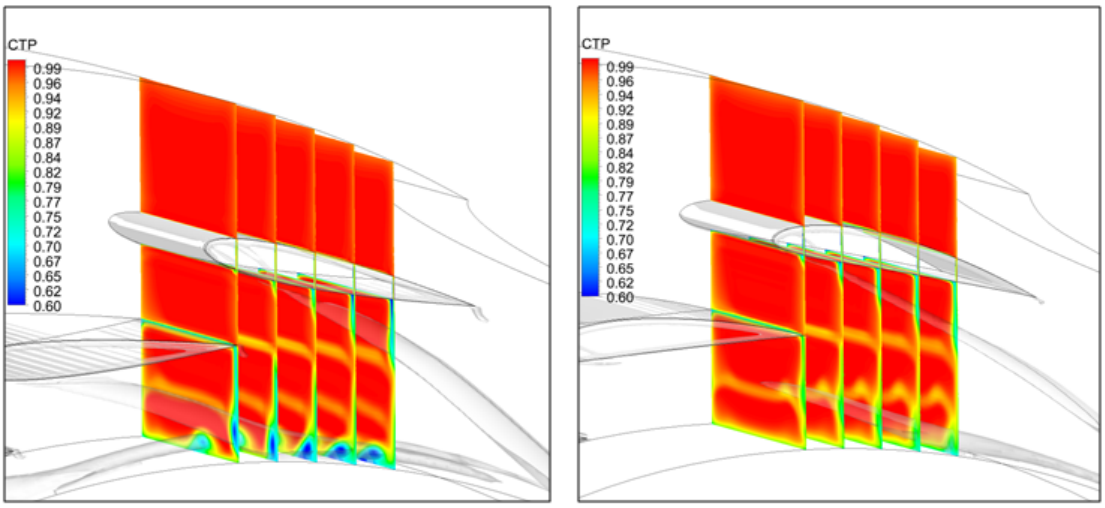

Figure 5.10: Total pressure contour at BEP

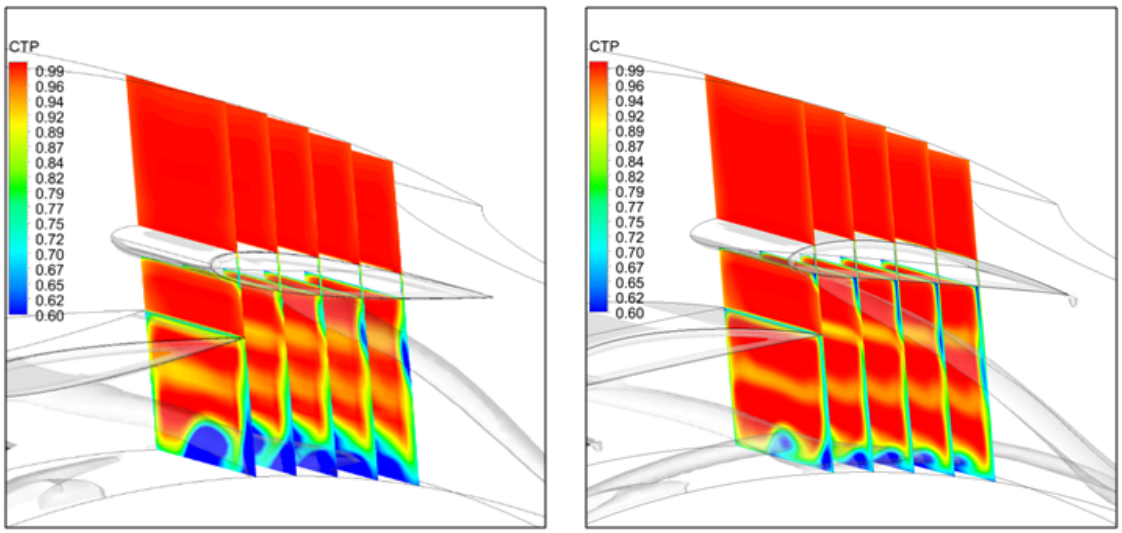

Figure 5.11: Total pressure contour at –5° with respect to BEP

5.2.4 Torque

When the GV rotates around the axis of the shaft, it induces torque in the GV due to the uneven pressure acting on it. It is desirable to have a minimum torque around the GV at all the operating conditions. The value of the torque depends on the position of the shaft. Figure 15 shows the values of the torque for all the opening angles, calculated with the shaft placed at locations from x/c = 0.35 to 0.52. It can be seen from the figure that the position of the shaft could be ideal for one operating

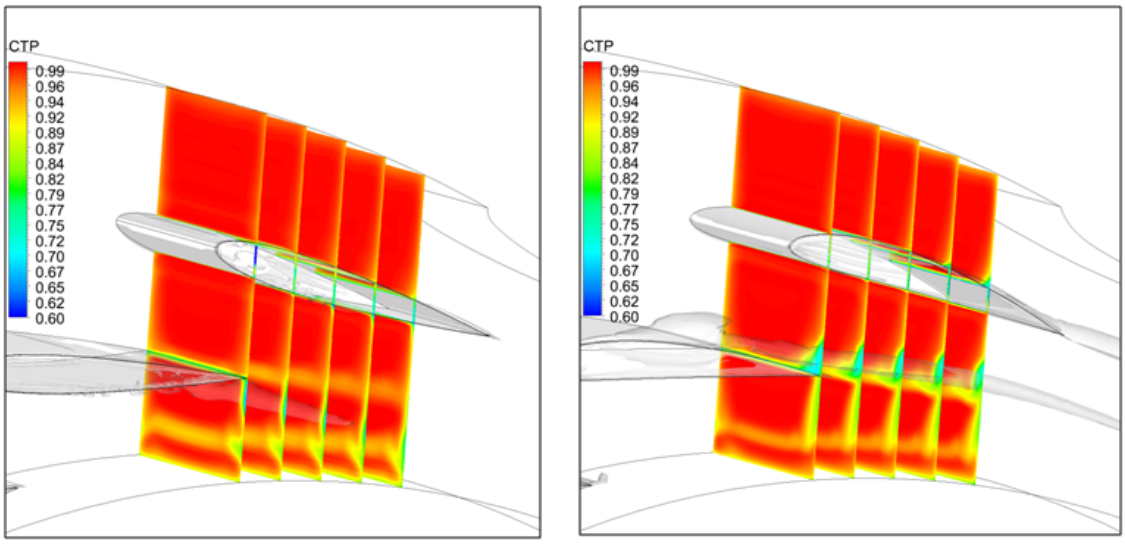

Figure 5.12: Total pressure contour at 5° with respect to BEP

condition, but it could result in a high torque in another condition. Hence an optimum position needs to be selected. In the case of NACA0012, when the shaft is placed at x/c = 0.41, a constant torque of around -50 N/m is constantly acting on the GV for all the opening angles.This contant torque can be reduced to around 15 N/m in the case of NACA4412, when the shaft is placed at x/c = 0.40.

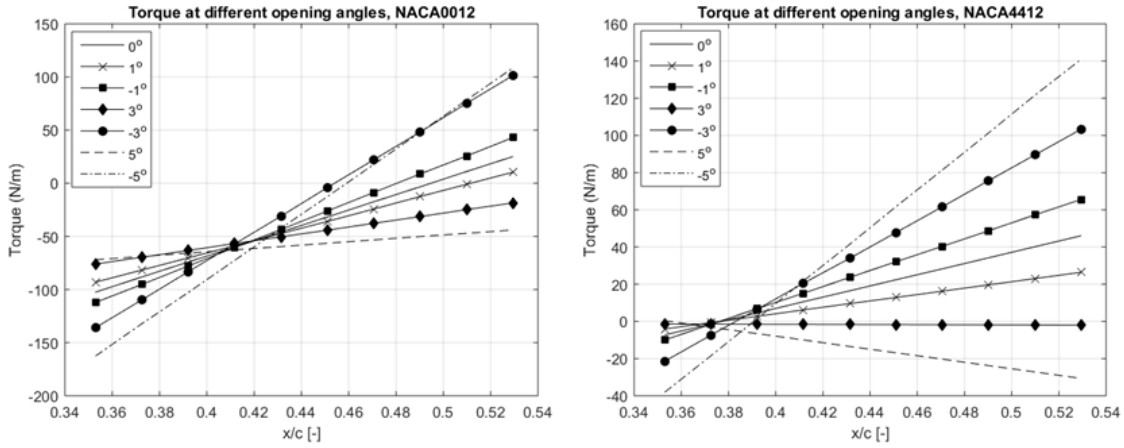

Figure 5.13: Torque acting on GV with two profiles

5.3 Summary of the study in three GV rig

A numerical investigation of the leakage flow through GV clearance gap was carried out in a three GV cascade rig. The results of the simulations were compared with the CFD and experiment, carried out in one GV rig. On comparing results of NACA0012 and NACA4412 as the GV profiles, it was seen

that the leakage flow depends on the GV loading. At BEP and in GV closing, NACA4412 reduces the pressure difference compared to NACA0012, which decreases the leakage flow and intensity of the vortex filament downstream. However, at high GV opening angles, the difference in pressure becomes negative in NACA4412. This changes the direction of the leakage flow, which makes the vortex travel in opposite direction. In the case of real turbines, these vortices will have a tendency to hit adjacent GV walls instead of entering the runner blades.

It can be inferred from these results NACA4412 as the GV profiles could be a better option for erosion and cavitation of runner blades for all operation conditions in sediment containing flow. However, more investigations need to be carried out to study the consequences of negative leakage flow for full load operations. A numerical investigation of the leakage flow in the actual turbine is presented in the next chapter.

Chapter 6

Effect of Leakage Flow on Turbine's Performance

The previous chapters included the study of flow phenomena around erosion induced clearance gap of GV cascades. The chapters focused on the mechanism of the leakage flow and its consequence on the formation of the vortex filament. The study was made in two different cascade rigs which contain periodic sections of the GV ring, such that the flow inside the rig matched with that in actual turbine. It was seen that the vortex filament originates from the leakage flow, which has a tendency to hit the runner towards inlet. In this chapter, a numerical study is performed on actual turbine by taking GV and runner blade passages of the same turbine. The results of the simulation are compared with that of cascade rigs. The effect of the vortices originating from GV on the runner is investigated. The comparison between three GV profiles is made in different GV opening angles.

6.1 Numerical model

This study primarily uses numerical analysis to study the flow field inside Francis turbine. Simulations were carried out for 3 GV profiles and 11 opening angles including BEP. Hence, 33 different combinations were tested in steady analysis. The domain for the steady analysis consists of 4 GVs and 3 runner blade passages, as shown in Figure 6.1. The full model of the turbine consists of 24 GVs and 17 runner blades. The dimension of the turbine and design of these blades correspond to the actual turbine in Jhimruk HPP excluding splitters. The domain was divided into 3 sub domains, GV (stationary), runner (rotating) and a portion of draft tube (stationary). At inlet, a mass flow rate corresponding to the designed flow of the turbine was given for BEP. This flow varied according to different GV openings, maintaining almost constant head for all the cases. Atmospheric pressure was assumed at the outlet of the draft tube for all the cases. The objectives of steady analyses were to i) study the overall performance of the turbine at all operating conditions ii) study the leakage flow through the clearance gap. The simulations used SST turbulence model, with high-resolution

discretization in advection scheme and first order upwind scheme in turbulence equations.

Transient analyses were carried out for 9 different combinations, which included 3 operating conditions for each GV profile. In this case, the domain consists of the full model of the turbine, so that the interface ratio of close to 1 is maintained between stationary and rotating components. The transient simulations were carried out for total time corresponding to 1.5 revolutions, and at a time step of 1° per step. The objectives of transient analyses were to i) predict the true transient interaction of the flow between guide vane and runner ii) calculate the pressure pulsation contributed by the leakage flow. The boundary conditions for respective opening angles were maintained same as the steady analysis.

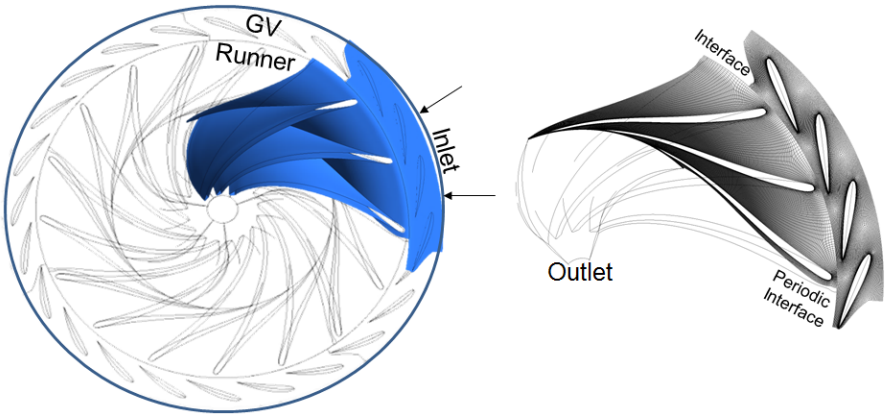

Figure 6.1: Domains and boundaries for steady analysis

6.1.1 Mesh sensitivity study

The design of the turbine's runner blade was in the form of co-ordinates at different span height of the runner. These co-ordinates were exported in the curve format, which could be used to make the mesh in ANSYS Turbogrid. The reference guide vane consisted of symmetrical NACA0012 profile, which was compared with NACA2412 and NACA4412 in this study. The model was discretized using hexahedral structured mesh. The discretization error was calculated using the GCI method [5]. The mesh refinement was done by increasing the distribution in each direction, i.e. the grid refinement factor (r) by 1.3×. The mesh sensitivity study was carried out by taking one GV and one runner blade passages. The guide vanes contained clearance gap of 1mm at both sides. For three sizes of the mesh, the clearance gap contained 5, 7 and 9 elements along the height, with total mesh count of 0.39M, 1.03M and 2.82M respectively. Pressure difference between adjacent sides of the GV and hydraulic efficiency of the turbine were chosen as the monitored variables. The calculation of the uncertainties involved due to mesh size was done using the reference [28].

Table 6.1 shows the uncertainties and extrapolated values of the efficiency. It also shows the description and formula of various parameters used in the calculation. The numerical uncertainty of the efficiency for the fine mesh was calculated to be 0.06%. This value was 0.14% for the medium

mesh.

Table 6.1: Discretization error in turbine

	Parameter	Value
Efficiency (%)	r_{21}	1.3975
	r_{32}	1.3829
	$\phi_{coarse(3)}$	94.37
	$\phi_{medium(2)}$	94.33
	$\phi_{fine(1)}$	94.31
	ϕ_{ext}	94.26
	GCI^{21}_{fine}	0.00068

Figure 6.2 shows the uncertainties and extrapolated values of the pressure difference between pressure and suction sides at mid-span of GV. The discretization error bars are computed for the fine mesh. The numerical uncertainty for ΔP ranged from 0.5% to 26% with higher errors towards leading and trailing edges. However, size of the error bars in the mid region seems to be larger than the edges in the figure. This is due to high pressure difference towards the mid-chord region.

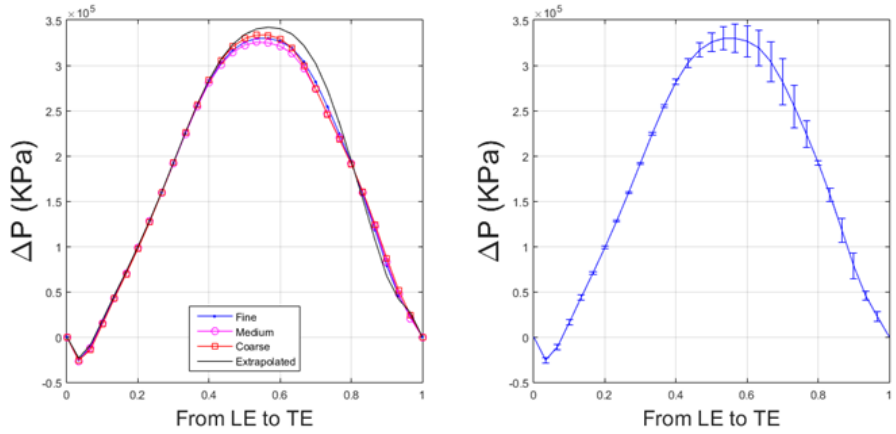

Figure 6.2: ΔP between pressure and suction side at mid-span with extrapolated values and discretization error bars

6.2 Comparison with experiment

The solution obtained in the turbine was compared with one GV cascade rig in terms of the velocity distribution around GV. The two cases contain the GVs with same shape and size, which makes the

comparison appropriate. In the previous chapter, both CFD and PIV was conducted in the GV cascade rig to obtain the velocity field around GV. Figure 6.3 shows the velocity field at the mid-span obtained in cascade and in the turbine. The velocity distribution around GV in the turbine is comparable with the rig. At the stagnation point, the velocity ranges between 10-14 m/s. The maximum velocity in the cascade is around 35 m/s, which is in the region of lowest area downstream of GV. As the turbine does not contain this region, the maximum velocity remains close to 30 m/s. At the suction side, the velocity rises after the mid chord position, signifying high pressure difference and consequent leakage flow through the gap. Hence, the overall trend of velocity distribution around GV in turbine's simulation was found to be similar with the experiment.

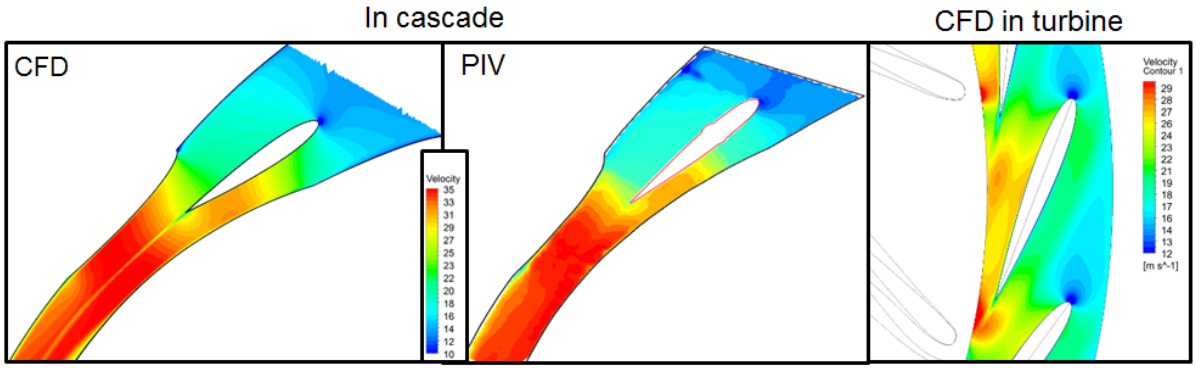

Figure 6.3: Velocity contour at GV's mid-span in one GV cascade rig and in turbine

A vortex filament was observed during the experiment, originating towards the trailing edge and travelling downstream. The vortex was also observed from the CFD of the rig and the turbine. Figure 6.4 shows the comparison of the vortices between the three cases. The origin and path of the vortices in all the cases look similar. In the picture of the rig, the white line downstream of GV represents the vortex. Since the runner blade is close to the GV's trailing edge, the energy of the vortex is transferred to the inlet of the blade. Hence, the total length of the vortex filament in the turbine is less than in the cascade. The results of CFD in turbine are in good agreement with the CFD and experiment in one GV's cascade rig. Hence, further simulations were carried out by using the same numerical model.

Figure 6.4: Vortex filament observed from CFD and experiment

6.3 Effect of the size of the clearance gap

In this study, clearance gap was considered to have a uniform surface. In a real condition, apart from the dry clearance gap, the eroded pattern is irregular as shown in Figure 3.3. The size of the clearance gap increases gradually with continuous abrasion by the sediments. Since only one size of the gap is tested for further simulations, this section compares the effect of using different size of the gap. Stagnation angle at the inlet of the runner blade (α) at different span of the blade was taken as the parameter for comparison. The angle, α is described in Figure 6.6. The comparison was done at BEP, since other opening angles might influence the flow due to separation. The two GV profiles, NACA0012 and NACA4412 were tested. The size of the gap was varied from 0.5 mm to 2 mm at the interval of 0.5 mm. The gap influences the α angle near hub and shroud, as shown in Figure 6.5. The incidence angle reduces near the edges, which is proportional to the size of the gap. It can also be seen that the angle is not affected significantly in NACA4412, compared to NACA0012 by increasing the gap. As the size of the gap influences the performance of the turbine linearly, the gap size of 1 mm was chosen for all the further simulations.

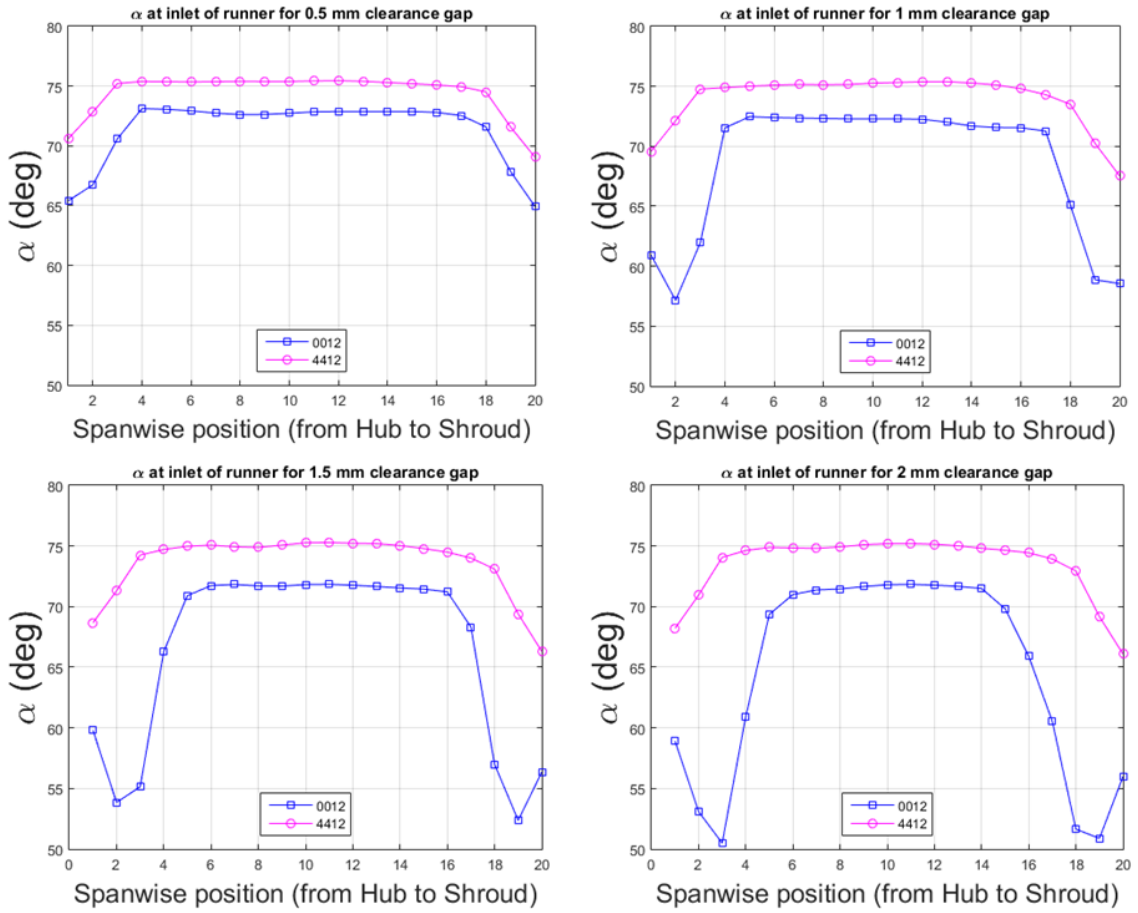

Figure 6.5: Stagnation angle at the inlet of the runner from hub to shroud

Figure 6.6 shows the effect of the reduction of the incidence angle on the velocity triangle. The reduction in the angle reduces tangential absolute velocity component (C_u) at the inlet of the runner.

From Euler's equation of the turbine, the hydraulic efficiency of the turbine is dependent on the C_u component. The reduction of C_u at inlet implies less efficiency. Improper stagnation angle might also enhance cavitation, because of a high pressure gradient between the two sides of the GV. A potential consequence is shown in the figure from Cahua HPP, where the inlet of the blade towards the shroud end experienced both erosion and cavitation.

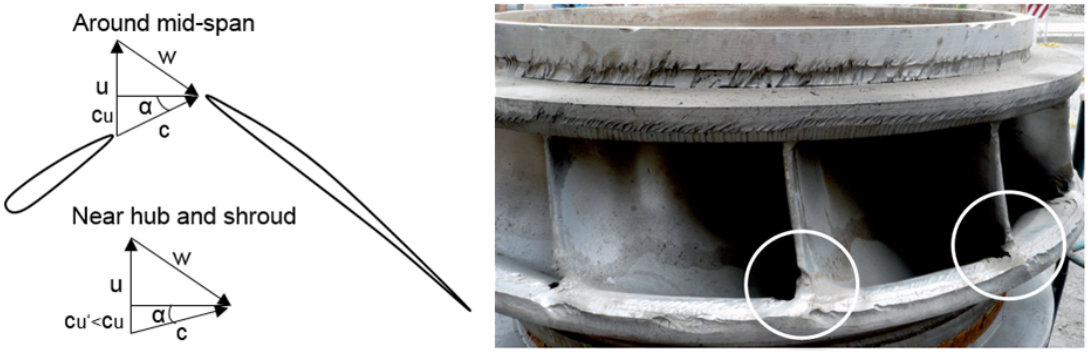

Figure 6.6: Velocity triangle due to change in the stagnation angle and its potential effect

6.4 Results and Discussions

6.4.1 Efficiency

Efficiency of the runner was calculated based on the available and extracted power by the runner. The extracted power was calculated from the torque generated in the rotating blades and the rotating speed of the turbine. The available power is derived from the discharge and the net head within the runner. Figure 6.7 is the plot of flow against efficiency at 1 mm clearance gap at both ends, where 100% flow implies BEP. The efficiency curves have a similar trend in all the three cases of GV profiles. The lowest efficiencies were found in part load conditions, when the flow is minimum. However, in all the operating conditions, it can be seen that the runner with GVs containing NACA4412 profile is the most efficient. The rise in efficiency is in the range of 1.5 – 3%, compared to NACA0012. NACA2412 produces intermediate efficiencies, which is 0.5 - 1-5% more than NACA0012. The rise in efficiency can be related with the reduced leakage flow in asymmetric profiles. Comparison of the leakage flow is done in the next sections. However, a fraction of the total efficiency rise might also be due to change in the GV outlet angle. This results in increase in the stagnation angle at inlet of the runner, as shown in Figure 6.6, which increases the swirl component, C_u.

6.4.2 Leakage flow at BEP

In this study, leakage flow is referred to the flow passed inside the clearance gap from high pressure to low pressure side of the guide vanes. The amount of leakage flow can be interpreted from the

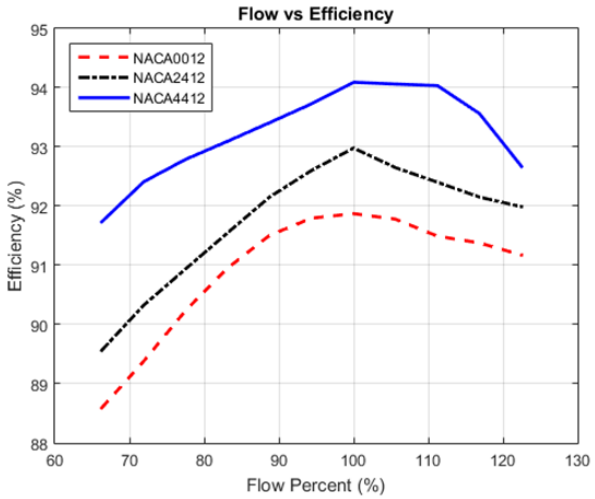

Figure 6.7: Efficiency of the runner at all operating points for 3 GV profiles

velocity vectors plotted inside the gap. Figure 6.8 shows the velocity vectors plotted along the chord (camber for the case of asymmetric profile) line inside the clearance gap for three hydrofoils. At BEP, the velocity vectors in NACA4412 follow the direction of the main flow. This is due to the similar pressure distribution around GV's adjacent sides. The velocity vectors in NACA0012 and NACA2412 seem to deviate away from the main flow significantly. This leakage flow mixes with the main flow to cause more disturbances in downstream turbine components.

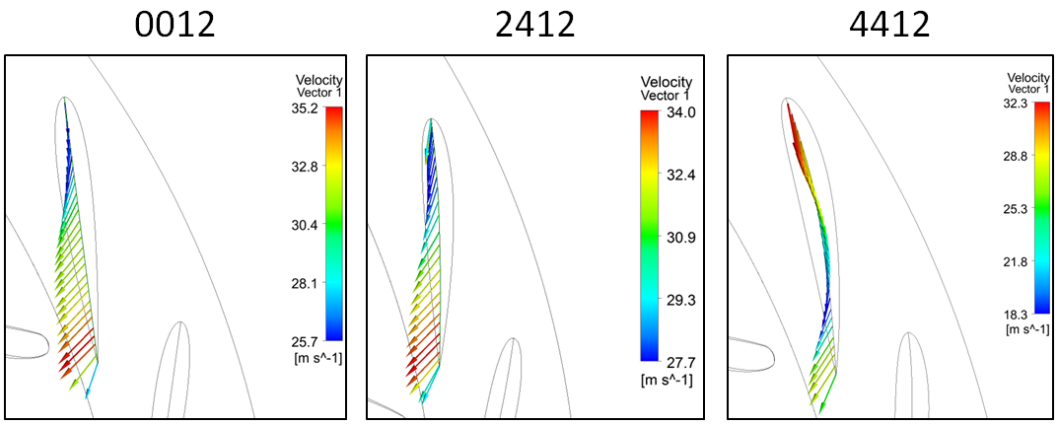

Figure 6.8: Velocity vectors along the camber-line of the guide vanes at BEP

The velocity vectors shown in Figure 6.8 can be resolved in two components, one component following the path of the camber and another one, perpendicular to the camber line (Vy). In an ideal case, when there is no leakage flow through the gap, the flow follows the camber line, with Vy = 0. Depending upon the velocity vector, Vy can be positive as well as negative, with larger values signifying more leakages. The explanation of Vy is also shown in Figure 2.7. In Figure 6.9, the Vy component is plotted against the camber line, from leading edge (LE) to the trailing edge (TE) of the guide vane in the mid-plane of the clearance gap. In all the three cases, it can be seen that the Vy is high towards the trailing edge of the guide vane, which can also be seen in Figure 6.8. Compared to

NACA0012, the trend of Vy in NACA2412 is similar, with the maximum value dropping by around 20%. In the case of NACA4412, this drop is more than 40%. Also, in most of the locations, the value of Vy is close to zero. This result was compared with pressure distribution (C_p) around GV in one GV cascade rig [13]. Comparing this plot with Figure 4.10 for NACA0012 shows a close relation between the two results. The pressure difference near the leading edge is close to zero, which directs the flow along the camber line, without producing any cross-leakage flow. The pressure difference gradually rises as the flow moves along the guide vane, increasing the Vy component. Finally, near the trailing edge, the Vy component decreases, signifying low C_p.

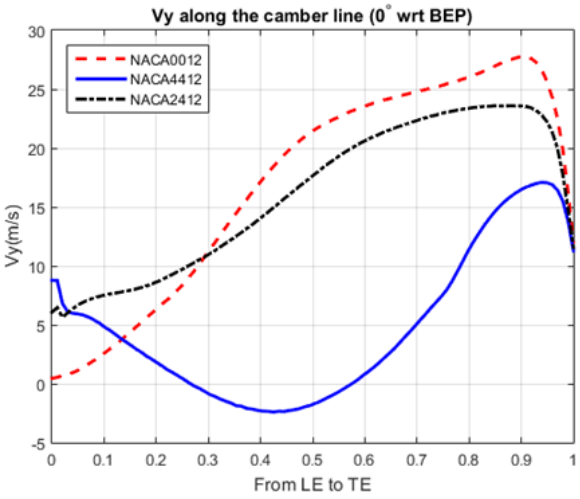

Figure 6.9: Velocity vectors along the camber-line of the guide vanes at BEP

Figure 6.10 shows the isosurface of the swirling strength at BEP obtained from transient analysis for three profiles. It is one of the methods to visualize the vortex core, which represents imaginary part of complex eigenvalues of velocity gradient tensor. The positive value of the discriminant of velocity gradient tensor for complex eigenvalues gives positive swirling strength, indicating existence of swirling motion around local centers. The three GV profiles are compared at same swirling strength and velocity on the vortex core to make the comparison easy. The isosufaces are extracted for t =0.075 s. It can be seen that the strength of the vortices and velocity of the flow in NACA0012 is highest among the three profiles. This result can be related with Figure 6.8 and Figure 6.9. The reduction in the vortex strength for NACA2412 is marginal.

Unsteady pressure at four span position of the runner inlet was investigated. Figure 6.11 shows the Fourier-transformed pressure pulsation for three GV profiles at the located points with a sampling frequency of 6000 Hz. The first peak represents average pressure value at respective points, which is at 0 Hz. This peak has not been shown in the figure. The second peak corresponds to blade passing frequency, which in this case is 400 Hz. The magnitude of this pressure is similar for one GV profile at all the monitored points. However, for each point, NACA0012 shows a maximum magnitude compared to other profiles. The plot also depicts higher order pulsations, which is predominant at point 1 and gradually dissipates towards the mid-span. This represents the pulsation from leakage flow vortices, which influences the fatigue life, as well as erosion of the runner blades. The pulsating pressure exists in all the tested profiles. However, it can be seen that the magnitude in NACA4412 is

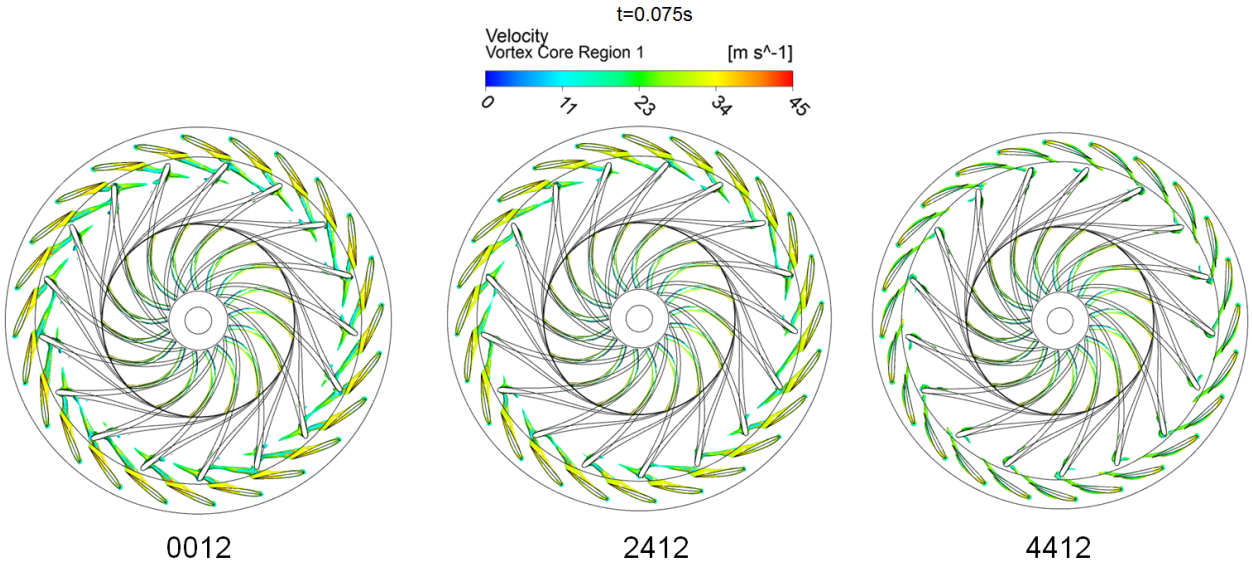

Figure 6.10: Isosurface contours of swirling strength, s (500 1/s) with velocity

the least among them.

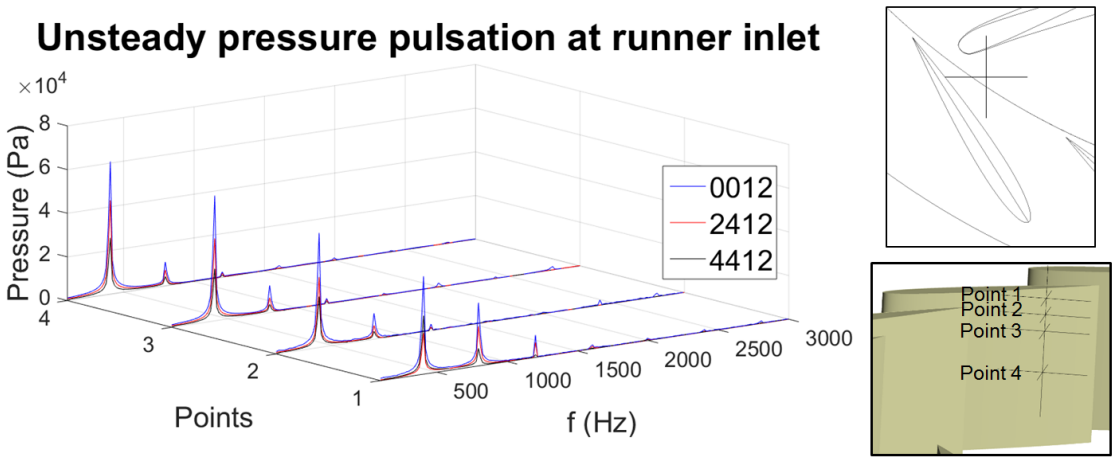

Figure 6.11: Pressure pulsation at runner inlet including the clearance gap at BEP

6.4.3 Leakage flow at off-designed conditions

Figure 6.9 showed the trend of Vy along the GV camber line at one operating condition. The same plot can be used to investigate the Vy at all GV opening angles. Alternatively, Equation 2.10 can be used to observe the Leakage Flow Factor at all the operating conditions using single plot. This factor averages the Vy values by considering negative leakage flow. In Figure 6.12, L_{ff}.Vo is plotted against the flow percentage. The flow of 100% implies BEP, lower than 100% implies part load and higher

than 100% implies full load conditions. At BEP, L_{ff} in NACA4412 reduces by more than 3 times compared to NACA0012. At part load conditions, when the GV is closing, L_{ff} increases for all the cases. This is due to increase in the pressure difference between adjacent sides of GVs at closing. NACA4412 maintains minimum L_{ff} at all the part load conditions compared to other profiles. The difference in L_{ff} between NACA0012 and NACA2412 is marginal at part load and BEP conditions.

At full load conditions, L_{ff} in NACA4412 increases gradually. This growth is representing some negative leakage flow occurring through the gap. The negative values are not shown in the graph because of the absolute terms used in equation. At the flow percent higher than 110%, the leakage flow in NACA4412 grows bigger than in NACA0012, reaching more than 30% of the reference case. Some negative leakage in NACA2412 is also seen towards higher GV opening, but total L_{ff} remains less than other profiles. It can be seen that the L_{ff} in NACA2412 can be reduced up to 2 times compared to NACA0012 at full load conditions.

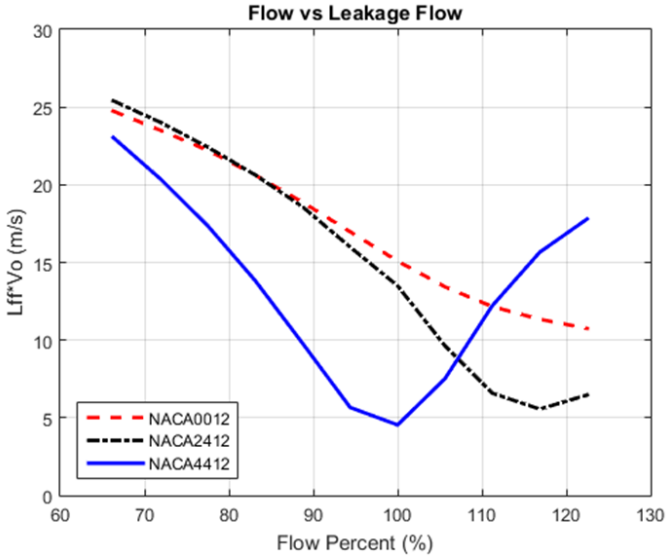

Figure 6.12: Leakage flow factor at all operating points

Turbines operate at high GV openings during wet seasons. This is the time when the concentration of sediment in the flow is maximum. It was seen from Figure 3.15 that the sediment concentration could vary a lot within a short span of time, depending upon the flow. This implies that turbines are most vulnerable to erosion in wet season. Furthermore, due to high discharge, the flow is accompanied with higher turbulences than that in dry season. In Figure 6.13, it can be seen how the vortices travel at full load conditions in NACA4412. The figure represents vorticity plot with swirling strength of 1500 Hz. The vortex starts to originate from leading edge of GV, and because of the negative leakage flow, the vortex tends to hit adjacent GV rather than going into the runner. However, due to i) larger distance between GV leading edge and the neighboring GV than between GV trailing edge and the runner inlet, and ii) lower intensity of these vortices compared to the one going into the runner for symmetrical profiles, the vortices seem to dissipate before hitting the succeeding GV. Some abrasive erosion might be seen towards the leading edge inside the gap, but the intensity of the abrasive erosion in full load operation is less because of the low pressure difference between the adjacent sides and low Vy (shown in Figure 6.9).

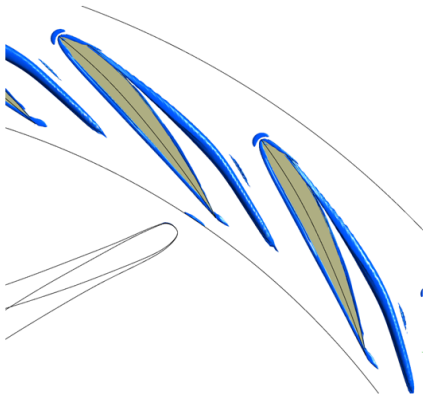

Figure 6.13: Nature of leakage flow in NACA4412 at full load operations

Figure 6.14 shows the unsteady pressure pulsation at the inlet of the runner for off-design conditions. Similar to Figure 16, the frequencies correspond to harmonics of blade passing frequency. The overall amplitude of the pressure in full load condition is higher than part load and BEP. This is due to more power extracted when the flow is maximum. Comparing the three profiles, the amplitude of the pressure in all the points and at all the frequencies is found to be maximum in NACA0012. At part load condition, the amplitudes of the pressure in Point 1 at 800 Hz are higher than the other points. However, these values are similar in full load condition. This shows that although the magnitude of rotor-stator interaction is high in all the cases at full load conditions, the effect of the leakage flow reduces.

These unsteady pressure pulsations lead to some important conclusions about the wear of the runner. The pulsations also causes reduction of the structural integrity of the runner by adding fatigue problems. It is shown from Figure 6.11 and Figure 6.14 that the amplitude of the pressure pulsations can be minimized by using asymmetric profiles. It can be seen that Point 1 is insignificantly affected due to leakage flow at full load conditions. Hence, the problem shown in Figure 6.6 might have been caused mostly in part load conditions and BEP. The use of asymmetric profiles as GVs could prove to be a good solution to these problems.

6.5 Summary of the simulations in turbine

On investigating the nature of the vortices originated from the leakage flow and erosion pattern of the runner, it was found that the vortices are responsible for both erosion and cavitation towards edges of the runner blade's inlet. Erosion occurs due to rotation of the flow and pulsating pressure in the vortex, whereas cavitation occurs due to incorrect stagnation angle at runner inlet. The phenomena of leakage flow was studied for three GV profiles. It was seen that the pressure difference between adjacent sides of the GV could be reduced by using NACA4412 profile for part load and best efficiency operation. The efficiency of the runner could be increased by 1.5 – 3 % at all the operating conditions. However, at full load operations, some negative leakage flow might appear in asymmetric profiles, which can have a risk of hitting adjacent GVs rather than flowing into the runner. In this study, the strength of

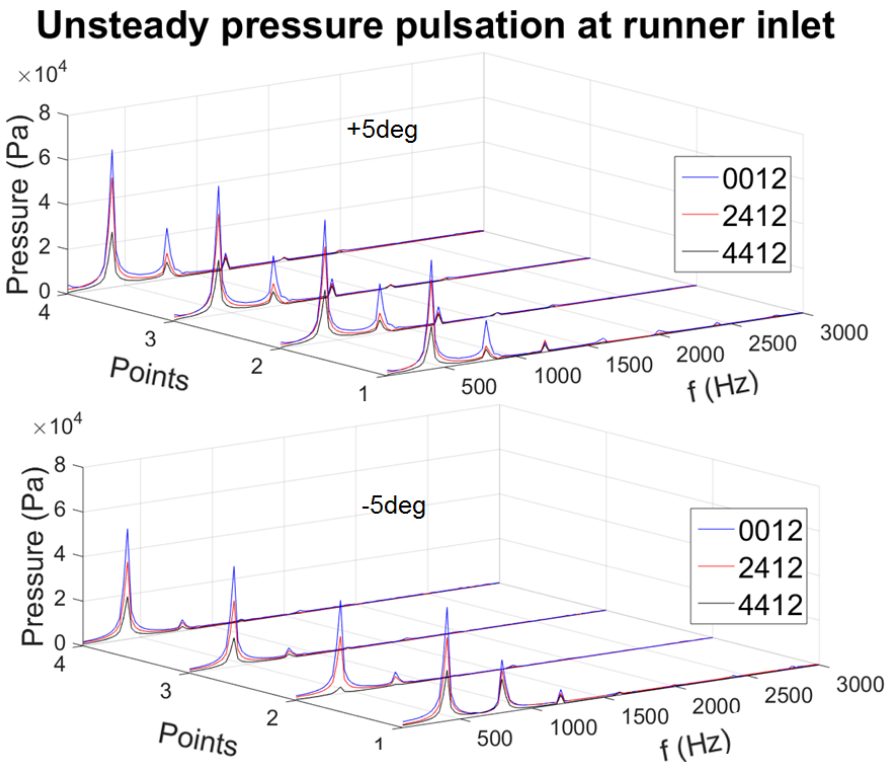

Figure 6.14: Pressure pulsation at runner inlet including the clearance gap at full load and part load conditions

such vortices was found to be tolerable. It was also found that the vortices dissipate before striking the neighboring GV. In the cases where the intensity of the vortices is intolerable and full load conditions are more significant, an intermediate profile, for example, NACA2412 can be an optimum solution.

Chapter 7

Conclusion

Sediment erosion in hydraulic turbines is a localized problem of Himalayan and Andes. The flow in Francis turbines is highly unsteady and several secondary flow phenomena adds to the losses, vibrations and fatigue problems. In the context of high sediment laden rivers, these secondary flows can accelerate the erosion, which forms wear patterns decreasing the thickness of the vanes. When the turbine surfaces are deteriorated, it causes more unsteadiness in the flow, decreasing the efficiency and increasing the impact of erosion. Hence, the effect of the secondary flow and sediment erosion in Francis turbines is simultaneous, which means that one problem is both the cause and the effect of another problem.

Although Francis turbines are acquainted with several erosion mechanisms and flow behavior, this thesis focused on erosion in guide vanes, more specifically, erosion and flow in clearance gaps of the guide vanes. In many power plants of Nepal including Jhimruk HPP, it was observed that the size of the clearance gap increases due to abrasion of the sediment particles through the gap. It was found that due to the pressure difference between two sides of the GV, the flow leaks through the gap from high pressure side to low pressure side at high acceleration, disturbing the primary flow. The leakage flow originates a vortex filament, which is vulnerable to the turbine, especially runner, in terms of the loss in efficiency as well as erosion, cavitation and fatigue problems at the runner inlet. The study of these phenomena was done in one GV cascade rig in this study, both experimentally and numerically. Following are some conclusions about the study of the flow around GV, using cascade rigs.

- A one GV cascade rig gives a close estimation of the flow field around GV compared to the real turbine. However, the flow is affected by the wall covering the rig. This affects the periodicity of the flow from one GV to another.
- Limitations of one GV rig could be overcomed by using three GV cascade rig. In this case, the flow around the middle GV would give closer estimation of the flow field than one GV rig. Moreover, such rig would also be suitable to test the flow in different GV opening angles, which was not possible in one GV rig. Hence, three GV rig could be the optimum method of testing the flow field around GV.

CFD simulation was one of the major techniques used in this work for investigating the flow fields around GV. By comparing the results between PIV and CFD, it was seen that by using a proper numerical model, the estimation of the flow field around GV could be done effectively. Following are some conclusions about the comparison between CFD and experiments.

- The pressure distribution around GV showed an average deviation of 0.6% on the pressure side and 3.3% on the suction side between CFD and pressure measurement through transducer.
- At GVout in mid-span, the mean of the average velocity was found to be 29.94 m/s in PIV and 33.14 m/s in CFD. The velocity contours between CFD and PIV at mid-span was found to be comparable. However, the results of PIV was affected by the presence of shadows and geometrical imperfections. Besides, due to grid size in the case of PIV than CFD, the regions around high velocity gradients were not properly resolved. Nevertheless, the average values between CFD and PIV showed close match. This shows that PIV could be one of the suitable methods to validate the CFD solutions. CFD can further be used to study the details of the flow physics, which would not be possible with PIV.
- It was seen from both experiments and CFD that the leakage flow mixes with the main flow in the suction side, producing a rotational component. A vortex filament originates from this rotation, which has a tendency to move towards mid-span while traveling downstream. In the case of a real turbine, runner blades are positioned near to the GV outlet, which lets these vortices hit the inlet of the blades towards hub and shroud.

In this thesis, the leakage flow through the clearance gap was related with the pressure difference between the two sides of the GV. Although the symmetrical GVs produces zero lift force, when the angle of attack in 0° and the flow passage is straight, the circular orientation of the GVs produces pressure and suction sides, which causes lift force greater than zero. This lift force drives the leakage flow and also induces torque around the GV axis. It was found that the change in the GV profiles can minimize the leakage flow. One GV cascade rig was used to test the flow in BEP, whereas other GV opening angles were simulated using three GV rig and the actual turbine. Following are the conclusions about the comparison between different GV profiles.

- It was found that in general, symmetrical profiles are not suitable for GVs in Francis turbines containing erosion in clearance gaps.
- A term 'Leakage Flow Factor' (L_{ff}) was defined to quantify the leakage flow from clearance gaps of GVs. With a gap of 2mm, L_{ff} in different asymmetrical profiles for BEP showed reduction, by as much as 4.45 times.
- CFD in three GV cascade at 7 GV opening angles showed that in NACA4412 profile, the leakage flow can be reduced for all the operating conditions. The velocity component, Vy, which is the component normal to the GV chord was found to be 27.4 m/s in average for NACA0012, whereas this value was 20.7 m/s for NACA4412, at BEP. Similarly, the reduction in Vy for NACA4412 was seen in all the opening angles. However, at high GV opening angles or full load conditions, some negative leakage flow could be seen in NACA4412. The vortex,

in this case had the tendency to hit neighboring GV at the suction side than hitting the runner blade.

Since the cascade rigs did not contain the runners, the effect of the leakage flow and consequent vortices were studied numerically, by simulation GVs and runner blade passages. The vortices orginating from the leakage flow was compared with that in cascades and it was found that these vortices were of similar nature. However, since the runner blades are located close to the GV's trailing edge, the energy carried by the rotating flow is transferred to the inlet of the runner, towards the connecting ends. 3 GV profiles at 11 opening angles were tested for clearance gap of 2mm on both sides of the GV in this work and the effect of the vortices on the runner blades and performance of the turbines were studied. Following points were concluded from this section.

- The leakage flow from the clearance gap develops vortices, which has a tendency to hit the runner blade towards hub and shroud. Due to the high rotational velocity, erosion of the runner blade is aggravated and cavitation occurs due to shifting of the incidence angle at runner inlet. Furthermore, since the swirl component at the runner inlet is reduced, the efficiency of the runner reduces.
- At part load and BEP conditions, NACA4412 showed least leakage flow, which eventually reduced the efficiency of the runner. At full load conditions, negative leakage flow was observed from NACA4412, which generates vortices in opposite direction. These vortices will have a tendency to hit the neighboring GVs. However, due to larger distance between the GVs than between GVs and runner, the vortices were found to be dissipated before striking the neighboring GV.
- In this study, GVs with asymmetrical profiles of same thickness compared to the reference profile were found be more effective in the case of erosion affected turbines. By using NACA4412, it was found that the efficiency of the runner increases by 1.5 to 3% compared to NACA0012. However, in the case of negative leakage flow with high intensity at full load conditions, an intermediate profile between NACA0012 and NACA4412 can be an optimum solution, in general.

7.1 Recommendations for further work

This thesis gave an indication that the behavior of the flow through the clearance gap of GV changes according to different GV profiles. The GVs investigated in this work consisted of standard NACA profiles with equivalent thickness. However, by using rigorous optimization techniques, customized profiles can be made such that the effect of the clearance gap is minimized at all operating conditions without any negative leakage flow.

Experimentally, this thesis included the PIV investigation of the flow in one GV cascade rig. The major aim of this experiment was to validate the numerical solutions. Advanced PIV setups can

be used to observe time dependent boundary layer wakes from the GV. A three GV cascade rig is currently under development. This rig can be used to validate the numerical investigations done in the same rig in this thesis. Also, by using seeding particles of density close to the sand particle, the behavior of these particles in the flow can be investigated.

Numerically, this thesis included the simulations for one phase flow. By inserting sand particles in the flow and defining a proper erosion model, erosion rates and patterns on the turbine can be studied. Also, by defining a multiphase flow and using a proper cavitation model, the behavior of the cavitating vortices originating from the leakage flow can be investigated. With computational advancement, the simulations can be carried out in a complete turbine (from spiral casing to draft tube).

This thesis contained GVs with uniform clearance gaps. However, in reality, the clearance gaps are irregular due to non-uniform erosion pattern by sand particles. The eroded GVs can be replicated in 3D models by using advanced 3D scanner. Moreover, the eroded geometry also requires high mesh density around this region.

In earlier studies, the runner blades were optimized for minimum erosion without affecting the efficiency. In this study, the change in the profile of the GV has been proposed. By using the combination of these studies, the optimum combination of GV and runner can be used for both simulations as well as experiments.

Chapter 8

Summary of publications

8.1 Paper 1

Title: *Study of the simultaneous effects of secondary flow and sediment erosion in Francis turbines*

Abstract

Sediment erosion of the hydropower turbine components is one of the key challenges due to the constituent of hard particles in the rivers of Himalayas and Andes. In the case of Francis turbines, the erosion is mostly observed around stay vanes, guide vanes and runner blades. Depending upon the type of flow phenomena in particular regions and operating conditions, the sediment particles having certain geometric and material properties create distinct erosion patterns on those regions. The flow phenomena in Francis turbines are highly unsteady, especially around guide vanes and runner. The unsteadiness arises in the form of leakage through clearance gap, horseshoe vortex, rotor-stator-interaction and turbulences supported by high velocity and acceleration. The erosion on the other hand deteriorates the surface morphology, aggravating the flow. Thus, this paper explains the simultaneous nature of the two effects, which in combined, contributes to more losses, vibrations, fatigue problems and failure of the turbine. It also discusses some of the research endeavors to minimize the combined effect by controlling either the erosion or the secondary flow in the turbine. This study emphasizes the need of understanding the relationship between the two phenomena and techniques of how the combined effect can be predicted as well as minimized.

Chitrakar Sailesh, Neopane Hari Prasad and Dahlhaug Ole Gunnar, "Study of simultaneous effects of secondary flow and sediment erosion in Francis turbines," Renewable energy, vol. 97, pp. 881-891, 2016.

8.2 Paper 2

Title: *Numerical and experimental study of the leakage flow in guide vanes with different hydrofoils*

Abstract

Clearance gaps between guide vanes and cover plates of Francis turbines tend to increase in size due to simultaneous effect of secondary flow and erosion in sediment affected hydropower plants. The pressure difference between the two sides of the guide vane induces leakage flow through the gap. This flow enters into the suction side with high acceleration, disturbing the primary flow and causing more erosion and losses in downstream turbine components. A cascade rig containing a single guide vane passage has been built to study the effect of the clearance gap using pressure sensors and PIV (Particle Image Velocimetry) technique. This study focuses on developing a numerical model of the test rig, validating the results with experiments and investigating the behavior of leakage flow numerically. It was observed from both CFD and experiment that the leakage flow forms a passage vortex, which shifts away from the wall while travelling downstream. The streamlines contributing to the formation of this vortex have been discussed. Furthermore, the reference guide vane with symmetrical hydrofoil has been compared with four cambered profiles, in terms of the guide vane loading and the consequent effect on the leakage flow. A dimensionless term called Leakage Flow Factor (Lff) has been introduced to compare the performances of hydrofoils. It is shown that the leakage flow and its effect on increasing losses and erosion can be minimized by changing the pressure distribution over the guide vane.

Chitrakar Sailesh, Thapa Biraj Singh, Dahlhaug Ole Gunnar and Neopane Hari Prasad, "Numerical and experimental study of the leakage flow in guide vanes with different hydrofoils", Journal of Computational Design and Engineering, vol. 4, no. 3, pp. 218-230, 2017.

8.3 Paper 3

Title: *PIV investigation of the leakage flow through clearance gaps in cambered hydrofoils*

Abstract

At the outlet of guide vanes of Francis turbines, about 50% of the total head of the system is converted into kinetic energy. This causes high acceleration of the flow in guide vanes and increase in the swirl component, which adds to the unsteadiness and losses in the turbine. In sediment affected power plants, the hard sand particles under the action of this unsteady flow erodes the turbine material. The erosion gradually increases the clearance gap between the guide vane and facing plates, which further aggravates the flow, causing more disturbances in downstream turbine components. Previous studies have shown that the shape of the hydrofoil in guide vanes has a major role in driving the leakage flow through the clearance gap. This study focuses on investigating the flow through the clearance gap of the guide vane with cambered hydrofoil shapes by using Particle Image Velocimetry (PIV) technique. The measurements are carried out in one guide vane cascade rig, which produces similar velocity fields around a guide vane, as compared to the real turbine. The investigation is done in two cases of cambered guide vane NACA profiles and the comparison of the velocity and pressure distribution around the hydrofoil is done with the results in symmetric profile studied earlier. It is seen that the pressure distribution around the hydrofoil affects the velocity field, leakage flow and characteristics of the vortex filament developed inside the cascade. NACA4412, which has flatter suction side than NACA2412 and NACA0012, is seen to have smaller pressure difference between the two adjacent sides of the vane. The flow inside the clearance gap of NACA2412 enforces change in the flow angle, which forms a vortex filament with a rotational component. This vortex along with improper stagnation angle could have greater consequences in the erosion of the runner inlet and more losses of the turbine.

Chitrakar Sailesh, Neopane Hari Prasad and Dahlhaug Ole Gunnar, "Particle Image Velocimetry investigation of the leakage flow through clearance gaps in cambered hydrofoils", Journal of Fluids Engineering, vol. 139, p. 091201, 2017.

8.4 Paper 4

Title: *Erosion wear due to sediment in guide vanes of Francis turbine and its effect on performance of the turbine*

Abstract

Erosion in the distributor of Francis turbines deteriorates the flow and gradually causes loss of efficiency. The abrasive wear in the clearance gap of guide vanes increases the gap size, which induces leakage flow due to pressure difference between adjacent sides. The leakage flow mixes with the main flow, forming a vortex filament, which is driven inside the runner. When these vortices carrying sediment particles hit the runner, the inlet of the runner blade towards hub and shroud can experience both erosion and cavitation. This paper presents a case study of a power plant in Nepal, whose runner and guide vanes are facing this type of wear. It is shown that the leakage flow is a root cause of such effect and it can be minimized by reducing the pressure difference in guide vanes. The study uses a numerical approach to investigate the phenomena of leakage flow inside the guide vane and its effect on the runner. The results are compared with experiment conducted in one guide vane's cascade rig, developed for the same model. Simulations are performed for 3 guide vane profiles with each at 11 operating conditions. It is found that the symmetrical guide vane profile, which is the reference profile in the plant, might not be suitable for best efficiency and part load conditions. Such a profile could wear the runner blade by both erosion and cavitation. However, at full load operations, the pressure difference in symmetrical guide vane is less than the other conditions. It is also found that asymmetrical profiles could increase the performance of the turbine at all operating conditions. However, some negative leakage flow could appear at high opening angles, which have a tendency to hit neighboring guide vane causing erosion. Hence, a proper selection of the guide vane profiles is needed to get an optimum performance at all operating conditions.

Chitrakar Sailesh, Dahlhaug Ole Gunnar and Neopane Hari Prasad, "Erosion wear due to sediment in guide vanes of Francis turbine and its effect on performance of the turbine", Under Review.

8.5 Paper 5

Title: *Numerical investigation of the flow phenomena around a low specific speed Francis turbine's guide vane cascade*

Abstract

Guide vanes of Francis turbines convey a significant influence on the flow field at the inlet of the runner. This influence is in the form of pressure pulsation, caused due to rotor-stator-interaction. A guide vane cascade containing a single blade passage was developed to predict the flow field experimentally. This study investigates flow phenomena around the guide vane cascade through computational techniques. A reference case is taken as the condition where the guide vane profile is symmetrical and there is no clearance gaps between the blade and cover plates. The results for this case is compared with experimental results to develop an appropriate numerical model for this setup. The influence of increasing the clearance gap on the flow is studied. Such gaps are expected to increase when the flow containing eroding particles passes through the turbine. This paper also shows that the pressure difference between the pressure and the suction side of guide vane can be reduced by changing the guide vane profile. The reduction of the pressure gradient will reduce leakages through clearance gaps, hereby condensing the subsequent effect of pressure pulsations and erosion.

Chitrakar Sailesh, Thapa Biraj Singh, Dahlhaug Ole Gunnar, Neopane Hari Prasad, "Numerical Investigation of the flow phenomena around a low specific speed Francis turbines guide vane cascade", IAHR Conference 2016.

References

[1] **Edenhofer, O., Madruga, R.P., Sokona, Y.**,
Renewable energy sources and climate change mitigation: special report of the Intergovernmental Panel on Climate Change,
Intergovernmental Panel on Climate Change (IPCC), 2012

[2] **Milliman, J.D., Meade, M.H.**,
World-wide delivery of river sediments to the oceans,
Journal of Geology, vol. 91. pp. 1-21, 1983

[3] **Thapa, B.**,
Sediment Erosion in Hydro Turbines,
PhD thesis, Norwegian University of Science and Technology, 2004

[4] **Thapa, B.S., Trivedi, C., Dahlhaug, O.G.**,
Design and development of guide vane cascade for a low speed number Francis turbine,
Journal of Hydrodynamics, Ser. B, vol. 28, pp. 676-689, 2016

[5] **Celik, I.B., Ghia, U., Roache, P., Freitas, C., Coleman, H., Raad, P.**,
Procedure for estimation and reporting of uncertainty due to discretization in CFD applications,
ASME J. Fluids Eng., vol. 130, pp. 078001, 2008

[6] **Price, T., Probert, D.**,
Harnessing hydropwer: A practical guide,
Applied energy, vol. 57, no. 2/3, pp. 175-251, 1997

[7] **IEC**,
Hydraulic turbines, storage pumps and pump-turbines - Model acceptance tests,
CEI/IEC 60193:1999.

[8] **Stachowiak, G.W., Batchelor, A.W.**,
Engineering Tribology,
3rd Edition, Elsevier, 2006

[9] **Truscott, G.**,
A literature survey on abrasive wear in hydraulic machinery,
Wear, vol. 20, no. 1, pp. 29-50, 1971

[10] **IEC**,
Hydraulic machines. Guide for dealing with hydro-abrasive erosion in Kaplan, Francis, and Pelton turbines,
BS EN 62364:2013.

[11] **Raffel, M., Willert, C.E., Werely, S.T., Kompenhans, J.**,
Particle Image Velocimetry – A practical guide,
2nd Edition, Springer, 2007

[12] **Durbin, P., Reif, B.**,
Statistical theory and modeling for turbulent flows,
John Wiley, 2001

[13] **Menter, F.**,
Two equation eddy-viscosity turbulence models for engineering applications,
AIAA Journal, vol. 32, pp. 1598-1605, 1994

[14] **Darmawi, Sipahutar, R., Bernas, S., Imanuddin, M.S.**,
Renewable energy and hydropower utilization tendency worldwide,
Renewable and Sustainable Energy Reviews, vol. 17, pp. 213-215, 2013

[15] **Felix, D., Albayrak, I., Abgottspon, A., Boes, R.**,
Hydro-abrasive erosion of hydraulic turbines caused by sediment - a century of research and development,
IOP Conf. Series: Earth and Environmental Science, vol. 49, p. 12001, 2016

[16] **Masoodi, J., Harmain, G.**,
Sediment erosion Francis turbine runners in the Himalayan region of India,
Hydropower and Dams, no. 1, pp. 82-89, 2017

[17] **Teran, L., Aponte, R., Munoz-Cubillos, J., Roa, C. Coronado, J., Ladino, J., Larrahondo, F., Rodriguez, S.**,
Analysis of economic impact from erosive wear by hard particles in a run-of-the-river hydroelectric plant,
Energy, vol. 113, pp. 1188-1201, 2016

[18] **Burwell, JT**,
Survey of possible wear mechanisms,
Wear, vol. 1, no. 2, pp. 119-141, 1957

[19] **Bhusan, B.**,
Introduction to Tribology,
John Wiley and Sons, 2002.

[20] **Brekke, H.**,
Design of hydraulic machinery working in sand laden water,
Abrasive erosion and corrosion of hydraulic machinery, London, pp. 155-81, 2002

[21] **Bergeron, P.**,
Similarity conditions for erosion caused by liquids carrying solids in suspension,
La Houille Blanche, B.H.R.A. translation T 408, 1950

[22] **Bak, E.**,
Construction materials and testing results of the wear of pumps for transporting solid media,
Biuletyn Glownego Instytuta Gornictwa, B.H.R.A. translation, 1966

[23] **Chauhan, A.K., Goel, D.B., Prakash, S.**,
Erosion behavior of hydro turbine steels,
Indian Institute of Technology, 2007

[24] **Brekke, H.**,
The influence from the guide vane clearance gap on efficiency and scale effect for Francis turbines,
14th IAHR Symposium, section on hydraulic machinery equipment and cavitation, Trondheim, 1988

[25] **Thapa, B.S., Thapa, B., Eltvik, M., Gjosater, K., Dahlhaug, O.G.**,
Optimizing runner blade profile of Francis turbine to minimize sediment erosion,
26th IAHR Symposium on Hydraulic Machinery and Systems, 2012

[26] **Eltvik, M.**,
Sediment erosion in Francis turbines,
PhD Thesis, Norwegian University of Science and Technology, 2013

[27] **Chitrakar, S., Cervantes, M. Thapa, B.S.**,
Fully coupled FSI analysis of Francis turbines exposed to sediment erosion,
International Journal of Fluid Machinery and Systems (IJFMS), vol. 7, no. 3, pp. 101-109, 2014

[28] **Thapa, B.S., Dahlhaug, O.G., Thapa, B.**,
Sediment erosion in hydro turbines and its effect on the flow around guide vanes of Francis turbine,
Renewable and Sustainable Energy Reviews, vol. 49, pp. 1100-1113, 2014

[29] **Tsuguo, N.**,
Estimation of repair cycle of turbine due to abrasion caused by suspended sand and determination of desilting basin capacity,
International seminar on sediment handling technique, Kathmandu, 1999

[30] **Bajracharya, T.R., Joshi, C.B., Saini, R.P., Dahlhaug, O.G.**,
Sand erosion of Pelton turbine nozzles and buckets: a case study of Chilime hydropower plant,
Wear, vol. 264, pp. 177-84, 2008

[31] **Thapa, B.S., Thapa, B., Dahlhaug, O.G.**,
Empirical modelling of sediment erosion in Francis turbines,
Energy, vol. 41, pp. 386-391, 2012

[32] **Trivedi, C., Gandhi, B., Cervantes, M.**,
Effect of transients on Francis turbine runner life: a review,
Journal of Hydraulic Research, vol. 51, no. 2, pp. 121-132, 2013

[33] **Hasmatuchi, V., Roth, S., Botero, F., Avellan, F., Farhat, M.**,
High-speed flow visualization in a pump-turbine under off-design operating conditions,
25th IAHR Symposium on Hydraulic Machinery and Systems, 2010

[34] **Kobro, E.**,
Measurement of pressure pulsations in Francis turbines,
PhD Thesis, Norwegian University of Science and Technology, 2010

[35] **Nicholet, C., Ruchonnet, N., Avellan, F.**,
One-dimensional modeling of Rotor Stator Interaction in Francis,
23rd IAHR Symposium, Yokohama, 2006

[36] **Finstad, P.H.E.**,
Secondary flow fields in Francis turbines,
PhD Thesis, Norwegian University of Science and Technology, 2012

[37] **Su, W., Li, X.B., Li, F.C., Wei, X.Z., Han, W.F., Liu, S.H.**,
Experimental investigation on the characteristics of hydrodynamic stabilities in Francis hydro-turbine models,
Advances in Mechanical Engineering, vol. 2014, 2014

[38] **Antonsen, O.**,
Unsteady flow in wicket gate and runner with focus on static and dynamic load on runner,
PhD Thesis, Norwegian University of Science and Technology, 2007

[39] **Neopane, H.P.**,
Sediment erosion in hydro turbines,
PhD Thesis, Norwegian University of Science and Technology, 2010

[40] **Eltvik, M.**,
Sediment erosion in Francis turbines,
PhD Thesis, Norwegian University of Science and Technology, 2013

[41] **Neopane, H.P., Thapa, B., Dahlhaug, O.G.**,
The effect of sediment characteristics for predicting erosion on Francis turbines blades,
The International Journal on Hydropower and Dams, vol. 19, no. 1, 2012

[42] **Pradhan, P., Joshi, P.N., Biswakarma, M.B.**,
Efficiency thermodynamic measurement at Jhimruk hydropower plant,
9th international symposium on river sedimentation, China, 2004

[43] **Thapa, B., Chaudhary, P., Dahlhaug, O.G., Upadhyay, P.**,
Study of combined effect of sand erosion and cavitation in hydraulic turbines,
International Conference on Small Hydropower - Hydro Sri Lanka, 2007

[44] **Koirala, R., Chitrakar, S., Regmi, S., Khadka, M., Neopane, H., Thapa, B.**,
Analysis of sediment samples and erosion potential: A case study of upper Tamakoshi hydroelectric project,
Hydro Nepal Journal, no. 16, pp. 28-31, 2015

[45] **Singh, M., Banerjee, J., Patel, P., Tiwari, H.**,
Effect of silt erosion on Francis turbine: a case study of Maneri Bhali Stage-II, Uttarakhand, India,
ISH Journal of Hydraulic Engineering, vol. 19:1, pp. 1-10, 2013

[46] **Koirala, R., Thapa, B., Neopane, H., Zhu, B., Chhetry, B.**,
Sediment erosion in guide vanes of Francis turbine: A case study of Kaligandaki Hydropower Plant, Nepal,
Wear, vol. 362-363, pp. 53-60, 2016

[47] **Koirala, R., Neopane, H., Shrestha, O., Zhu, B., Thapa, B.**,
Selection of guide vane profile for erosion handling in Francis turbines,
Renewable Energy, vol. 112, pp. 328-336, 2017

[48] **Rajkarnikar, B., Neopane, H.P., Thapa, B.S.**,
Development of rotating disc apparatus for test of sediment-induced erosion in Francis runner blades,
Wear, vol. 306, pp. 119-125, 2013

[49] **Guangjie, P., Zhengwei, W., Yexiang, X., Yongyao, L.**,
Abrasion predictions for Francis turbines based on liquid–solid two-phase fluid simulations,
Engineering Failure Analysis, vol. 33, pp. 327-335, 2013

[50] **Rai, A., Kumar, A., Staubli, T.**,
Developing a test rig to measure hydro-abrasive erosion in Pelton turbine,
International Conference on Hydropower for Sustainable Development, Dehradun, 2015

[51] **Gohil, P., Saini, R.**,
Coalesced effect of cavitation and silt erosion in hydro turbines - A review,
Renewable and Sustainable Energy Reviews, vol. 33, pp. 280-289, 2014

[52] **Kumar, P., Saini, R.**,
Study of cavitation in hydro turbines - A review,
Renewable and Sustainable Energy Reviews, vol. 14, pp. 374-383, 2010

[53] **Thapa, B.S., Dahlhaug, O.G., Thapa, B.**,
Sediment erosion induced leakage flow from guide vane clearance gap in a low specific speed Francis turbine,
Renewable Energy, vol. 107, pp. 253-261, 2017

[54] **Padhy, M.K., Saini, R.**,
A review on silt erosion in hydro turbines,
Renewable and Sustainable Energy Reviews, vol. 12, pp. 1974-1987, 2007

[55] **Mann, B., Arya, V.**,
Abrasive and erosive wear characteristics of plasma nitriding and HVOF coatings: their application in hydro turbines,
Wear, vol. 249, pp. 354-360, 2001

[56] **Desale, G., Gandhi, B., Jain, S.**,
Effect of erodent properties on erosion wear of ductile type materials,
Wear, vol. 261, pp. 914-921, 2006

[57] **Winkler, K., Dekumbis, R., Uppal, A.**,
Coating minimizes operational losses at Nathpa Jhakri in India,
Hydro Review Worldwide 19(1)

[58] **Dahlhaug, O.G., Skåre, P.E., Mossing, V., Gutierrez, A.**,
Erosion resistant coatings for Francis runners and guide vanes,
International Journal of Hydropower and Dams, vol. 17, no. 2, pp. 109-112, 2010

[59] **Felix, D.**,
Experimental investigation on suspended sediment, hydro-abrasive erosion and efficiency reductions of coated Pelton turbines,
PhD Thesis, ETH, 2017

[60] **Brekke, H.**,
A review on oscillatory problems in Francis turbines,
New Trends in Technologies: Devices, Computer, Communication and Industrial Systems, Sciyo, 2010, pp. 217-232

[61] **Chitrakar, S., Baidar, B., Koirala, R.**,
Spanwise re-stacking techniques in turbo-machinery blades and application in Francis runner,
RENTECH Symposium 4, Kathmandu, 2014

[62] **Eide, S.**,
Numerical analysis of the head covers deflection and the leakage flow in the guide vanes of high head Francis turbines,
PhD Thesis, Norwegian University of Science and Technology, 2004

[63] **Trivedi, C., Cervantes, M., Gandhi, B., Dahlhaug, O.G.**,
Experimental and numerical studies for a high Head Francis turbine at several operating points,
ASME J. Fluids Eng, vol. 135, pp. 111102, 2013